Fall 2014

Ultrasound assisted low-temperature synthesis of TiB2 and Al3Ti particulates in molten aluminum

Zhiwei Liu
Purdue University

Graduate School Form 30
(Updated 11/20/2014)

PURDUE UNIVERSITY
GRADUATE SCHOOL
Thesis/Dissertation Acceptance

This is to certify that the thesis/dissertation prepared

By Zhiwei Liu

Entitled
Ultrasound Assisted Low-Temperature Synthesis of TiB2 and Al3Ti Particulates in Molten Aluminum

For the degree of Doctor of Philosophy

Is approved by the final examining committee:

Qingyou Han

David R. Johnson

Xiaoming Wang

Haiyan Zhang

To the best of my knowledge and as understood by the student in the Thesis/Dissertation Agreement, Publication Delay, and Certification/Disclaimer (Graduate School Form 32), this thesis/dissertation adheres to the provisions of Purdue University's "Policy on Integrity in Research" and the use of copyrighted material.

Approved by Major Professor(s): Qingyou Han

Approved by: James L. Mohler 12/03/2014

Head of the Department Graduate Program Date

ULTRASOUND ASSISTED LOW-TEMPERATURE SYNTHESIS OF TiB_2 AND Al_3Ti PARTICULATES IN MOLTEN ALUMINUM

A Dissertation

Submitted to the Faculty

of

Purdue University

by

Zhiwei Liu

In Partial Fulfillment of the

Requirements for the Degree

of

Doctor of Philosophy

December 2014

Purdue University

West Lafayette, Indiana

TO MY BELOVED FATHER

Mr. Jishan Liu

ACKNOWLEDGEMENTS

Firstly, I would like to thank my advisor Dr. Qingyou Han. He has provided me with a unique opportunity while studying at Purdue University. Through his guidance and enthusiasm, he has made my doctoral journey a thoughtful and rewarding experience. His patience and kindness has given me more space to explore different ideas in my research, and his enlightening wisdom will continue motivating me with my future work.

Secondly, I am also very grateful to my committee members, Dr. Xiaoming Wang, Dr. Haiyan Zhang, and Dr. David Johnson. Without their selfless assistance and guidance, it would have been hard to accomplish my dissertation.

I am also thankful to Dr. Wilson Xu and Dr. Milan Rakita for their support, including the valuable discussions with them and their friendly help during my research. Working with them has been a very pleasant experience.

In addition to thanking the above faculty members, I want to thank all the graduate students who have helped me during my studies and experiments. I will appreciate our friendship for the rest of my life.

Also, my deepest gratitude goes to my wife Dr. Lingjiao Liu and our son Zhuofan Liu. I am indebted to them very much as I have not been able to spend much time with them during my study. Their love and support is the driving force and motivation for my doctorial study in the US.

Finally, I want to acknowledge my mother, sister, brother in law, and my nephew for their help in taking care of my son. This dissertation would not have been finished without their selfless support.

TABLE OF CONTENTS

Page

Page

Page

LIST OF TABLES

LIST OF FIGURES

Figure Page

Figure Page

Figure Page

Figure Page

ABSTRACT

Liu, Zhiwei. Ph.D., Purdue University, December 2014. Ultrasound Assisted Low-Temperature Synthesis of TiB_2 and Al_3Ti Particulates in Molten Al. Major Professor: Qingyou Han.

In situ formed TiB_2 and Al_3Ti are two typical representatives of ceramic and intermetallic reinforcements in the in situ particulate reinforced Al composites. TiB_2 particulates can be synthesized in molten Al via the mixed-salts reaction by adding mixed K_2TiF_6 and KBF_4 salts into the Al melt at high temperatures. Al_3Ti particulates can be produced by the direct-melt reaction between solid Ti powders and liquid Al at high temperatures. Generally, a high reaction temperature is always needed to obtain both reinforcements. Some issues, however, such as high cost and burning loss of alloying elements in Al alloys, are usually associated with high manufacturing temperatures. Specifically, a higher temperature can lead to the formation of larger-sized particulates, which severely degrades the mechanical properties of composite materials. Therefore, exploring the low-temperature synthesis of TiB_2 and Al_3Ti particulates is meaningful for practical productions. Also, the formation mechanisms for both particulates are still unclear, especially at lower synthesizing temperatures.

This research is developed the following studies based on the above topics. The influences of reaction temperature and time on the mixed-salts reaction were studied. An ultrasound assisted technique was applied to the reaction at 700 °C. Results show that a

higher temperature can lead to a higher yield of TiB_2 with a shorter reaction time, but the size of TiB_2 produced becomes larger. With a 10-min reaction time, the yield of TiB_2 can reach 89.50 % and the size of most of TiB_2 is in the range of 300-800 nm at 900 °C; Most TiB_2 synthesized at 700 °C are smaller than 300 nm, but the yield is just 28.10 %. By using ultrasound, a high yield (90.40 %) of TiB_2 particulates with smaller size (smaller than 300 nm) can be obtained at 700 °C. The formation mechanism of TiB_2 was studied through a static experiment. At a higher temperature (900 °C), the synthesis of TiB_2 mainly follows the precipitation-growth process at the reaction interface. At a lower temperature (700 °C), the precipitation-growth process and dissolution reaction between AlB_2 and Al_3Ti both contribute to the formation of TiB_2. As the reaction time is prolonged, TiB_2 particulates with a smaller size can be formed. Ultrasound has remarkable effects on the formation of TiB_2 particulates, which can lead to accelerated mass transfers of [Ti] and [B] from salts to reaction interface and a high nucleation rate of TiB_2. These two effects contribute to the low-temperature synthesis of TiB_2.

For the direct-melt reaction, a reaction-peeling model is proposed to explain the formation of small blocky Al_3Ti particulates. Ultrasound is able to effectively accelerate the reaction-peeling process. The reaction time for a completed synthesis of Al_3Ti can be shortened significantly. Most importantly, the formation of inclusions containing solid Ti powders can be avoided in the ultrasonic fields, allowing for the realization of a lower-temperature synthesis of Al_3Ti at 700 °C.

CHAPTER 1. INTRODUCTION

1.1 Research Background

Through several decades of development, in situ particulate reinforced Al composites have been attracting more and more attentions in the aerospace and automobile industries due to their excellent properties, such as low density, high specific strength and modulus, good corrosion resistance, high thermal and electrical conductivity, and high damping capacity (Tjong & Ma, 2000).

Generally speaking, ceramic particulate and intermetallic particulate are two of the most important reinforcements in the Al matrix, in which TiB_2 and Al_3Ti are the typical representatives respectively due to their excellent properties. Numerous researchers have done lots of work on synthesizing both reinforcements in the Al matrix.

In practical productions, mixed-salts reaction has been extensively used for synthesizing in situ TiB_2/Al (alloys) composites, which involves adding mixed K_2TiF_6 and KBF_4 salts with a molar ratio of Ti/B=1/2 into molten Al (alloys) at high temperatures, leading to the formation of TiB_2 particulates (Feng & Froyen, 2000). For producing in situ Al_3Ti/Al (alloys) composites, a simple direct-metal reaction between solid Ti powders and liquid Al has becoming a promising approach for producing Al_3Ti particulates in the Al melt (Yu, Chen, Sun, & Min, 2006a).

In essence, the above two reactions both belong to chemical reactions. The temperature of molten Al, i.e. the reaction temperature is one of the most crucial factors, which significantly influences the formation of TiB_2 and Al_3Ti in each reaction. In general, a high temperature is beneficial for the synthesis of TiB_2 and Al_3Ti. As reported, the temperatures of liquid Al used in the mixed-salts reaction are always higher than 800 °C (Anandkumar, Almeida, & Vilar, 2011; Xue, Wang, Han, Chen, & Sun, 2012); and the temperatures used in the direct-metal reaction are greater than 900 °C (Jie, Kandalova, Zhang, & Nikitin, 2000; Yu, Chen, Sun, & Min, 2006a).

Some issues, however, are usually associated with the high temperatures. One is the high manufacturing cost, because higher temperature demands more energy. The other one is the burning loss of some alloying elements, such as Mg and Zn in Al alloys. Particularly, a higher temperature can result in the formation of larger-sized TiB_2 and Al_3Ti particulates. The existence of large-sized particulates in the matrix can lead to the reduction of tensile properties of materials, especially for the ductility and yield strength (Doel & Bowen, 1996). Thereby, decreasing the formation of large-sized particulates in the matrix is desired in most cases.

Based on the above introduction, it is found that a contradiction exists in both reactions for synthesizing particulates, which is a higher reaction temperature is good for the formation of particulates in molten Al, but easily leads to some negative impacts, such as high cost, burning loss of alloying elements and making particulates larger. Therefore, exploring an approach to synthesize TiB_2 and Al_3Ti particulates at lower temperatures is greatly meaningful for industrial productions.

So far, the understanding of the formation mechanism of TiB_2 and Al_3Ti in each reaction is not enough. For the mixed-salts reaction of K_2TiF_6-KBF_4-Al system, the formation mechanism of TiB_2 particulates is still under dispute. Two main viewpoints regarding the formation process of TiB_2 phase have been proposed. One refers that TiB_2 particulates are formed by a dissolution-precipitation mechanism when the concentrations of Ti and B reach saturation in molten Al (alloys) (Fan, Yang, & Zhang, 2005). The other one refers that TiB_2 particulates are synthesized resulting from the reaction between Al_3Ti and AlB_2, which are formed firstly due to the reactions of K_2TiF_6-Al and KBF_4-Al (Feng & Froyen, 2000). In nature, both mechanisms are based on the equilibrium thermodynamics of the Al-Ti-B system. However, the practical mixed-salts reaction of K_2TiF_6-KBF_4-Al is a typical non-equilibrium thermodynamic reaction. The conventional analysis is not able to reflect the actual formation process of TiB_2. In contrast, a kinetic study is more suitable to describe the formation process of TiB_2 particulates in the mixed-salts reaction.

For the direct-melt reaction between solid Ti powders and liquid Al, to our knowledge, the synthesis of Al_3Ti particulates at the temperatures below 800 °C has never been reported by other researchers. The evolution of solid Ti powders in liquid Al at low temperatures has never been explored. Since the reaction between solid Ti powders and liquid Al is also a non-equilibrium thermodynamic reaction, the study of the formation mechanism of Al_3Ti particulates can be conducted from a kinetic prospective. More work can be done in this field.

As mentioned above, decreasing the temperatures of molten Al can limit the formation of TiB_2 and Al_3Ti particulates in each reaction. In order to realize the low-

temperature synthesis of TiB_2 and Al_3Ti, some effective efforts should be applied to each reaction. The research about the chemical effects of ultrasound in a liquid has been lasting almost 90 years since the pioneering work of Richards and Loomis (1927). In their research, they recognized that intense sound waves travelling through a liquid could produce certain chemical effects, leading to accelerated chemical reactions. Since then, ultrasound assisted in situ technique has been widely used in organic synthesis, materials and organometallic chemistry, and other chemistry related fields (Mason & Lorimer, 2002; Suslick, 1988; Xu, Zeiger, & Suslick, 2013), for the intensification of chemical/physical processing applications can be promoted significantly in ultrasonic fields. Suslick (1990) has reported that ultrasonic irradiation could increase reactivities by nearly a millionfold in chemical reactions.

The effects of ultrasound arise from acoustic cavitation: the formation, growth, and implosive collapse of bubbles coupled to the ultrasonic fields (Zeiger & Suslick, 2011). The above process can occur simultaneously at millions of locations in a reactor within a few microseconds (Li, Li, Xiao, & Wang, 2014), which can achieve temperatures above 5000 K, pressures exceeding 10^5 kPa, and heating and cooling rates in excess of 10^{10} K/s (McNamara, Didenko, & Suslick, 1999; Merouani, Hamdaoui, Rezgui, & Guemini, 2014; Prasad, Sonawane, Zhou, & Ashokkumar, 2013; Suslick & Price, 1999). These extreme, transient conditions produced during acoustic cavitation can promote the reactions which need high temperature, high pressures, or long reaction times. Moreover, acoustic cavitation can generate some unique effects, such as shock waves, micro-jets and acoustic streaming, which can increase mass transfer to accelerate chemical reactions (Ma, Zhao, Yan, & Li, 2011).

Until now, the related report about using ultrasound in both reactions is rather limited. The mixed-salts reaction and direct-metal reaction are chemical reactions. More importantly, liquid Al exists in both reactions, which provides the environment for generating acoustic cavitation. Thereby, introducing high-intensity ultrasound in the mixed-salts reaction and direct-metal reaction can provide an opportunity for synthesizing TiB_2 and Al_3Ti particulates at lower temperatures.

1.2 Significance of This Research

As mentioned in the first section, the knowledge of mixed-salts reaction of K_2TiF_6-KBF_4-Al system and direct-melt reaction between solid Ti powders and liquid Al at low temperatures (as low as 700 °C) is rather limited. This research analyzes the formation mechanism of TiB_2 and Al_3Ti particulates in each reaction from a kinetic perspective by considering the reaction temperature, reaction time and external field (ultrasound), which can display more clearly the relationships between products and experimental parameters. A better understanding of the two reactions can be achieved.

Decreasing the temperature of molten Al is always desired in the fabrication of in situ particulate reinforced Al (alloys) composites. This research explores the possibilities of synthesizing TiB_2 and Al_3Ti in molten Al at 700 °C by using high-intensity ultrasound, in which the effects of ultrasound on the two reactions are investigated. A relationship between the formation of TiB_2 (Al_3Ti) and ultrasound also can be created. Accordingly, a novel technique referred as ultrasound assisted low-temperature synthesis of TiB_2 and Al_3Ti particulates is proposed in this research.

Through this research, some meaningful guidelines might be provided in the practical productions of in situ particulate reinforced Al (alloys) composites.

1.3 Purpose of the Research

To sum up, this research aims to understand the mixed-salts reaction of K_2TiF_6-KBF_4-Al system and the direct-metal reaction between solid Ti powders and liquid Al more deeply. The effects of experimental parameters, such as reaction temperature, reaction time and external filed (ultrasound) on the formation of TiB_2 and Al_3Ti particulates are investigated. The final purpose of this research is to synthesize TiB_2 and Al_3Ti particulates in molten Al at low temperatures by using ultrasound.

Especially, each reaction also has its own practical research purpose.

(1) Mixed-salts reaction: studying the relationships between the yields of TiB_2 particulates and their size distributions and reaction temperatures (900, 800, and 700 °C) with different reaction times (10 and 30 min); on the other hand, investigating the effects of ultrasound (700 °C, 10 min) on the yield and size distribution of TiB_2 particulates.

(2) Direct-metal reaction: exploring the evolutions of solid Ti powders in molten Al at two different temperatures (730 and 700 °C) with and without ultrasound.

1.4 Research Questions

Based on the above sections, the following research questions naturally arise:

1. How Al melt temperature and reaction time influence the synthesis of TiB_2 particulates in the mixed-salts reaction of K_2TiF_6-KBF_4-Al system? This research

question mainly studies the yields of TiB_2 particulates and their size distributions under different experimental parameters.

2. What is the formation mechanism of TiB_2 particulates in the mixed-salts reaction?

3. What are the effects of ultrasound on the formation of TiB_2 at a lower temperature (700 °C)?

4. What is the formation mechanism of Al_3Ti particulates in the direct-metal reaction between solid Ti powders and liquid Al?

5. How ultrasound influences the evolution of solid Ti powders in liquid Al at low temperatures?

1.5 Assumptions

This study is on the basis of experiments in the lab. The detailed assumptions of this research are given below.

1. The influences of exterior factors, such as the temperature and humidity of the environment, on the experiments are excluded.

2. There is no any difference in the raw materials which are used in this research.

3. All equipments used in this research have the same working conditions in each group of experiment.

4. Ultrasonic equipment used in this research has a steady output power.

1.6 Limitations

Due to the limitations of experimental equipments used in this research, the biggest challenge for this research is that the initial temperatures of molten Al are hard to set at

the exact temperatures designed in the experiments. Three different temperatures, 900, 800 and 700 °C are involved in the mixed-salts reaction; two temperatures, 730 and 700 °C are used in the direct-melt reaction. In each experiment, the temperature of molten Al is limited in the range of plus and minus 3 °C. Since the lowest temperature is set as 700 °C, this small temperature difference has little effect on both reactions.

In addition, the time for taking sample out from the graphite crucible is hard to control exactly in the direct-melt reaction. An error of a few of seconds exists when taking samples. This relative short period of time does not influence the analysis of the experimental results.

1.7 Delimitations

All the assumptions and limitations mentioned above can be combined in delimitations. Some of the main delimitations are as follows:

1. For the mixed-salts reaction, only three temperatures (700, 800 and 900 °C) of molten Al are considered. These three different temperatures are defined as low, moderate and high melting temperatures, respectively.

2. For the direct-melt reaction, only two temperatures (730 and 700 °C) of molten Al are considered.

3. The ultrasound parameters are the same in this research: the power of ultrasonic generator is 1.5 kW, and the frequency is 20 kHz.

4. Just pure Al is used in the two reactions. No any alloying element participates in the reactions.

5. This research mainly discusses the effects of Al melt temperature and ultrasound on the two reactions. Only products, viz. in situ formed particulates in the Al matrix are concerned. Others, such as the evolution of Al matrix exposed to ultrasound, are not involved in this research.

CHAPTER 2. LITERATURE REVIEW

2.1 Outline

According to the research focuses of this dissertation, three main topics are covered in this chapter. Firstly, the basics about in situ TiB_2/Al (alloys) composites, such as the characteristics of the TiB_2 phase as reinforcement in the Al matrix and the methods for synthesizing TiB_2 particulates in molten Al, are introduced. In this part, the mixed-salts reaction of K_2TiF_6-KBF_4-Al system for producing TiB_2 is discussed. Secondly, an introduction about the direct-melt reaction for synthesizing Al_3Ti is presented. In this part, the methods for obtaining Al_3Ti in molten Al, as well as the merits of the Al_3Ti phase as reinforcement in the Al matrix are both described. Finally, the backgrounds of high-intensity ultrasound, such as acoustic cavitation generated in ultrasonic field, as well as some chemical effects on the liquid-solid system associated with acoustic cavitation, are also introduced.

2.2 Review of TiB_2 Particulates Synthesized in Molten Al

2.2.1 Characteristics of TiB_2

TiB_2 possesses the hexagonal AlB_2 structure (Spoor, Maynard, Pan, Green, Hellmann, & Tanaka, 1997). The Ti and B atoms in TiB_2 form a hexagonal close packed (HCP) structure.

The hexagonal unit cell of single crystal TiB_2, having space group P6/mmm (a=b=3.029 A, c=3.229 A; α=β=90°, γ=120°), is shown in Figure 2.1. Ti atoms are located at (0, 0, 0) and B atoms at (1/3, 2/3, 1/2) and (2/3, 1/3, 1/2) lattice sites (Basu, Raju, & Suri, 2006). TiB_2 is a refractory compound with many attractive properties, including exceptional hardness (approximately 25-35 GPa at room temperature, more than three times harder than fully hardened structural steel), high elastic modulus (560 GPa), high melting point (>3000 °C), good creep resistance, good thermal conductivity (~65 W $m^{-1}K^{-1}$), and considerable chemical stability. The above properties are all attributed to the inherent crystal structure of TiB_2.

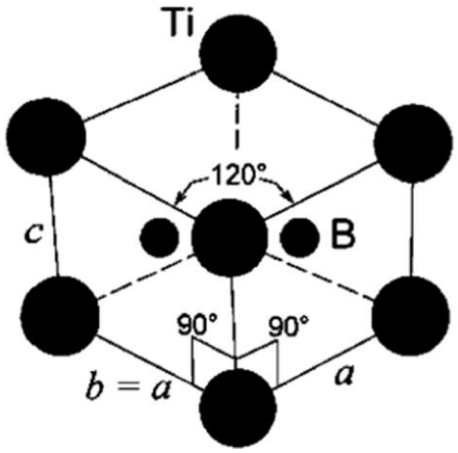

Figure 2.1 A hexagonal unit cell of single crystal of TiB_2.

Due to its unique characteristics, TiB_2 has been attracting more attentions as reinforcement in the fabrication of particulate reinforced Al (alloys) composites. Its chemical inertness in the Al matrix at elevated temperatures can guarantee a good high-temperature service performance, which is one of the most important advantages for TiB_2 compared with other reinforcements (Anandkumar, Almeida, & Vilar, 2011).

2.2.2 Synthesis of TiB_2 in Molten Al

In order to synthesize TiB_2 particulates in molten Al, a chemical reaction is needed to develop the reinforcement. To put it simply, the reactants added into molten Al should contain Ti and B elements, which can form the TiB_2 phase in the chemical reaction.

Tee et al. (2001; 1999) added a mixture of elemental Ti and B powders in molten Al at a high temperature (1060-1080 °C) to produce in situ TiB_2/Al composites through the traditional stir-casting technique. In their research, the in situ formed TiB_2 had a size ranging from 1 to 3 μm. However, a few large-sized Al_3Ti flakes with a length of 30-350 μm were also formed in the reaction, which led to a low ductility of the composites. The addition of a mixture of Ti and B simultaneously into molten Al leads to the following reaction:

$$2Ti + 2B + 2Al \rightarrow TiB_2 + Al_3Ti \qquad \text{Eq. 2.1}$$

Chen et al. (2000) added the blended powders of TiO_2, H_3BO_3, and Na_3AlF_6 into molten Al-4.5Cu alloy at 950 °C to synthesize TiB_2 particulates. In their research, the in situ formed TiB_2 particulates were spherical in shape and had an average diameter of about 0.93 μm. The chemical reactions that occurred during fabrication were given below:

$$2H_3BO_3 \rightarrow 3H_2O + B_2O_3 \qquad \text{Eq. 2.2}$$

$$2TiO_2 + B_2O_3 + 3Na_3AlF_6 + 8Al \rightarrow Na_2O + 2Al_2O_3 + 7NaF + AlF_3 + TiF_2 + 2AlF_3 + Al_3Ti + AlB_2 \qquad \text{Eq. 2.3}$$

The products Al_3Ti and AlB_2 were dissolved in the Al melt simultaneously, forming solutes [Ti] and [B]. Then, [Ti] was combined with [B] to form TiB_2 particulates:

$$[Ti] + 2[B] \rightarrow TiB_2 \qquad \text{Eq. 2.4}$$

Davies et al. (1992) proposed a promising method termed as flux assisted synthesis (FAS) for synthesizing TiB_2 in their patent. Since then, this process has become one of the most important methods for producing in situ TiB_2/Al (alloys) composites (especially for mass production) due to its advantages, such as low cost and simplicity.

In this method, a mixture salts of potassium hexafluorotitanate (K_2TiF_6) and potassium tetrafluororate (KBF_4) with a molar ratio of Ti/B=1/2 is added into a stirred Al melt at high temperatures, and then TiB_2 particulates can be formed in molten Al. The melting points of K_2TiF_6 and KBF_4 are given as 780 °C and 530 °C (Dragut, Moldovan, & Butu, 2012), and the lowest reaction temperature used in the conventional methods is at least 800 °C. The related schematic diagram of the typical mixed-salts reaction process is shown in Figure 2.2. Since a mixed K_2TiF_6-KBF_4 system is used in the fabricating process, FAS is also named as a mixed-salts reaction. Detailed information about this method will be provided in the following sections.

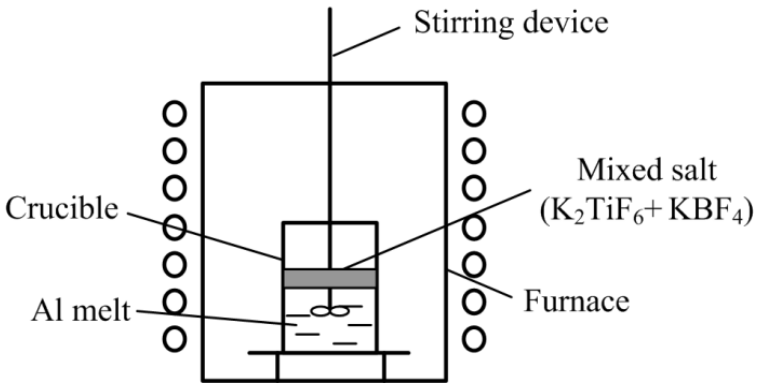

Figure 2.2 Schematic of the fabrication of in situ TiB_2/Al (alloys) composites by using the mixed-salts reaction.

2.2.3 Introduction to Mixed-salts Reaction

2.2.3.1 Formation of TiB_2 in Mixed-salts Reaction

According to Fjellstedt et al.(2005), the mixed-salts reaction of K_2TiF_6-KBF_4-Al system is complex, in which the processes, such as diffusion processes through the boundary layer between salts and molten Al, reactions in the melt, reactions inside the salt and formation of gases, have not been fully understood.

Feng et al.(2000) melted K_2TiF_6 and KBF_4 mixed salts at 810 °C and held for 35 min, but no TiB_2 phase was obtained in their experiment. They also used Ag to replace Al in the mixed-salts reaction, and no TiB_2 was obtained either. The above two experiments indicated that TiB_2 could not be formed without the existence of Al phase, suggesting that Al as the medium participated in the formation of TiB_2 phase in the mixed-salts reaction. Based on which, Feng et al.(2000) suggested that the formation of TiB_2 followed the reactions below:

$$3K_2TiF_6 + 13Al \rightarrow 3Al_3Ti + 3KAlF_4 + K_3AlF_6 \qquad \text{Eq. 2.5}$$

$$2KBF_4 + 3Al \rightarrow AlB_2 + 2KAlF_4 \qquad \text{Eq. 2.6}$$

$$Al_3Ti + AlB_2 \rightarrow TiB_2 + 4Al \qquad \text{Eq. 2.7}$$

In the above chemical reactions, once Al_3Ti and AlB_2 are formed through the reduction reactions according to Eqs. 2.5 and 2.6, both of which immediately react to form TiB_2 phase in molten Al. Mahallawy et al. (1999) also proposed similar chemical reactions in their research to describe the reaction process for synthesizing TiB_2.
An overall reaction (Eq. 2.8) for synthesizing TiB_2 can be given as follows:

$$3K_2TiF_6 + 6KBF_4 + 10Al \rightarrow 3TiB_2 + 9KAlF_4 + K_3AlF_6 \qquad \text{Eq. 2.8}$$

In addition, Lakshmi et al.(1998b), Fang et al. (2005) and Moldovan et al. (2010) all proposed a possible mechanism named as a dissolution-precipitation mechanism to describe the formation process of TiB_2 particulates in the mixed-salts reaction. The detailed mechanism can be summarized as follows.

First, K_2TiF_6 and KBF_4 are melted on the Al surface, both of which are separately decomposed to KF (liquid), TiF_4 (gas), and BF_3 (gas), which are expressed as Eqs. 2.9 and 2.10:

$$K_2TiF_6(l) \rightarrow 2KF(l) + TiF_4(g) \quad \text{Eq. 2.9}$$

$$KBF_4(l) \rightarrow KF(l) + BF_3(g) \quad \text{Eq. 2.10}$$

Then, Ti and B atoms are released and diffuse into liquid Al through the aluminothermic reduction of TiF_4 and BF_3 gases at the salts-melt interface, which are expressed as Eqs. 2.11 and 2.12:

$$TiF_4(g) + [Al] \rightarrow [Ti]_{Al} + AlF_3(l) \quad \text{Eq. 2.11}$$

$$BF_3(g) + [Al] \rightarrow [B]_{Al} + AlF_3(l) \quad \text{Eq. 2.12}$$

When the solutes [Ti] and [B] in liquid Al reach saturation, they might be separated out as compounds Al_3Ti, AlB_2 and TiB_2, according to the following reactions:

$$[Ti]_{Al} + 3[Al] \rightarrow Al_3Ti \quad \text{Eq. 2.13}$$

$$2[B]_{Al} + [Al] \rightarrow AlB_2 \quad \text{Eq. 2.14}$$

$$[Ti]_{Al} + 2[B]_{Al} \rightarrow TiB_2 \quad \text{Eq. 2.15}$$

Among these three compounds, TiB_2 is the most thermodynamically stable phase due to its lowest free energy of formation. The overall reaction showing the formation of TiB_2 can be written as:

$$3K_2TiF_6 + 6KBF_4 + 10Al \rightarrow 3TiB_2 + 12KF + 10AlF_3 \quad \text{Eq. 2.16}$$

After the mixed-salts reaction finishes, TiB_2 phase is the only product which can be kept in molten Al; whereas the molten byproduct salt consisted in a mixture of K_3AlF_6 and $KAlF_4$ or KF and AlF_3 can float on the melt surface due to its low density.

Based on the above two formation mechanisms, it is clear that three elements Al, Ti, B are all involoved in the formation of TiB_2 phase. A thermodynamic study about the mixed-salts reaction can help to understand the formation of TiB_2 more deeply. The related content will be introduced in the following section.

2.2.3.2 Thermodynamic Calculations on Mixed-salts Reaction

After adding K_2TiF_6-KBF_4 mixed salts into the Al melt, Ti and B elements can enter the Al melt; whereas K and F elements isolate with the Al matrix, both of which exist in the byproducts. Thereby, a ternary system of Al-Ti-B can be formed in the Al melt. For this system, thermodynamic calculation has consistently shown that the compound phases of AlB_2, Al_3Ti, and TiB_2 might be present in the Al melt (Hayes & Lukas, 1991; Yue, Lu, & Lai, 1999).

In general, excess fress energy, ΔG has been used to determine the possibility of a reaction. If ΔG is negative, it means the reacton can take place, otherwise the reaction can not occur. At a certain temperature of T, ΔG of a reaction system can be calculated by the following equation:

$$\Delta G = \Delta H - T\Delta S \quad \text{Eq. 2.17}$$

where ΔH and ΔS are respectively the changes in enthalpy and entropy of two states before and after reaction. It can be seen from Eq. 2.17 that ΔG is only a function of temperature. However, ΔG is also dependent on the concentration of the reactants for a solution system; therefore, the influence of composition on the reaction must be taken into account. Consider the following reaction which occurs in a liquid solution:

$$n_1 A_1 + n_2 A_2 \rightarrow n_3 A_3 + n_4 A_4 \qquad \text{Eq. 2.18}$$

where n_i is the stoichiometric coefficient of composition A_i. For the reactant, n_i is negative; while for the product, positive. In this reaction, ΔG can be expressed as:

$$\Delta G_{T,P} = \Delta G^0_{T,P} + \sum_i n_i RT \ln \alpha_i = \Delta G^0_{T,P} + \sum_i n_i RT \ln \chi_i + \sum_i n_i RT \ln \gamma_i \qquad \text{Eq. 2.19}$$

where $\Delta G^0_{T,P}$ is the standard Gibbs free energy of formation, which is just influenced by temperature, α_i the activity of component i, χ_i the molar concentration of component i in the solution, and γ_i the activity coefficient of component i. It is clear that $\alpha_i = \chi_i \bullet \gamma_i$. Hence, the excess free energy of reaction through can be expressed as follows:

$$\Delta G_{Al_3Ti} = \Delta G^0_{Al_3Ti} - 3RT \ln \alpha_{Al} - RT \ln \alpha_{Ti} \qquad \text{Eq. 2.20}$$

$$\Delta G_{AlB_2} = \Delta G^0_{AlB_2} - RT \ln \alpha_{Al} - 2RT \ln \alpha_B \qquad \text{Eq. 2.21}$$

$$\Delta G_{TiB_2} = \Delta G^0_{TiB_2} - 2RT \ln \alpha_B - RT \ln \alpha_{Ti} \qquad \text{Eq. 2.22}$$

Two steps need to be conducted before evaluating ΔGs of Al_3Ti, AlB_2 and TiB_2. First of all, the standard Gibbs free energy of formation (ΔG^0) of three compounds should be calculated.

Liang et al. (2008) studied the ΔG^0 values of the formation to AlB_2, Al_3Ti and TiB_2, and proposed the related equations, as shown in Table 2.1.

Table 2.1 ΔG^0 *Values of the Formation to* AlB_2, Al_3Ti *and* TiB_2.

Reactions	Expressions of ΔG^0/(J/mol)
$2[B]+[Al] \rightarrow AlB_2$	$-237812+182.5T(K)$
$[Ti]+3[Al] \rightarrow Al_3Ti$	$-335920+175.3T(K)$
$[Ti]+2[B] \rightarrow TiB_2$	$-4615411+92.3T(K)$

According to the above equations for calculating ΔG^0 values, the calculated results are plotted in Figure. 2.3.

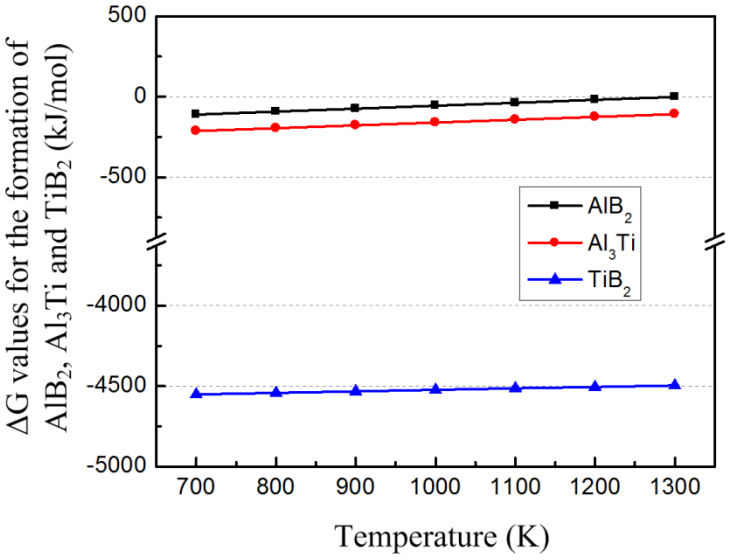

Figure 2.3 ΔG values for the formation of AlB_2, Al_3Ti and TiB_2 with temperature.

It can be observed that ΔG_{TiB_2} is far more negative than ΔG_{AlB_2} and ΔG_{Al_3Ti} at the temperature range of 700-1300 K, indicating that TiB_2 is the most thermodynamically stable phase among the three compounds, and which can be much easier to form than AlB_2 and Al_3Ti phases. In addition, as the temperature increases, the changes of in Gibbs free energies of AlB_2 and Al_3Ti phases become larger, suggesting these two phases become unstable at higher temperatures. This trend is more obvious for AlB_2 phase.

As mentioned above, in the reaction including liquid-state reactants and solid products, ΔG is not only a function of temperature, but also depends on the concentration of reactants. In order to calculate $\Delta G^0_{T,P}$ of reaction in Eq. 2.19, the value of γ_i, or $\ln \gamma_i$ should be known firstly. Yue et al. (1999) and Fan et al.(2005) used different methods to calculate γ_i, respectively.

Based on Lupis method (1983), Yue et al. (1999) introduced the concepts of first order interaction coefficient ε and second order interaction coefficient ρ to interpret how concentration affects the excess free energy as well as activity by using the central atom model (Lupis & Elliott, 1967) of a metallic solution which is limited to qualitative interpretation of the results. Further, the Taylor Series equation (Lupis & Elliott, 1966) was referred to calculate γ_i:

$$\ln \gamma_i = \ln \gamma_i^0 + \sum_{j=2}^{N} \varepsilon_i^j + \sum_{j=2}^{N} \rho_i^j \chi_j^2 + \sum_{j=2}^{N} \sum_{k=j}^{N} \rho_i^{jk} \chi_j \chi_k + O(\chi^3) \qquad \text{Eq. 2.23}$$

where γ_i^0 is the activity coefficient of component i under standard state, ε_i^j is the first order interaction coefficient among the components, and ρ_i^j, $\rho_i^{j,k}$ are the second order interaction coefficients among components units and can be expressed below:

$$\varepsilon_i^j = \left(\frac{\partial \ln \gamma_i}{\partial \chi_i} \right)_{Xsolovent \to 1} \quad \text{Eq. 2.24}$$

$$\rho_i^j = \frac{1}{2} \left(\frac{\partial^2 \ln \gamma_i}{\partial^2 \chi_j} \right)_{Xsolovent \to 1} \quad \text{Eq. 2.25}$$

$$\rho_i^{j,k} = \frac{1}{2} \left(\frac{\partial^2 \ln \gamma_i}{\partial \chi_j \partial \chi_k} \right)_{Xsolovent \to 1} \quad \text{Eq. 2.26}$$

For an Al-Ti-B system having low contents of Ti and B elements, the system can be approximated to be a dilute solution composed of Al as the solvent, and Ti and B as the solutes. According to Eq. 2.23, the contributions of Ti and B to the γ_i can be expressed by:

$$\ln \gamma_{Ti} = \ln \gamma_{Ti}^0 + \varepsilon_{Ti}^{Ti} \chi_{Ti} + \varepsilon_{Ti}^{B} \chi_B \quad \text{Eq. 2.27}$$

$$\ln \gamma_B = \ln \gamma_B^0 + \varepsilon_B^{Ti} \chi_{Ti} + \varepsilon_B^{B} \chi_B \quad \text{Eq. 2.28}$$

In the above equations, the second interaction coefficient ρ can be neglected since χ_i^2 is rather close to zero. The values of $\ln \gamma_i$ can be approximately evaluated. However, the further work was not carried out in their research.

Fan et al (2005) referred to the Wilson equation (Wilson, 1964) to evaluate the value of γ_i, the activity coefficient of component i is determined as:

$$\ln \gamma_i = -\ln(1 - \sum_j x_j A_{j/i}) + 1 - \sum_j \left[\frac{x_j (1 - A_{i/j})}{1 - \sum_K x_k A_{k/j}} \right], \quad \text{Eq. 2.29}$$

where x_j is the molar fraction of component j, and $A_{i/j}$, $A_{j/i}$ are adjustable parameters ($A_{i/j} \neq A_{j/i}$)

Especially, for a ternary system $i-j-k$,

Eq. 2.29 can be expressed in detail as:

$$\ln\gamma_i = 1-\ln(1-x_jA_{j/i}-x_kA_{k/i})-\frac{x_i}{1-x_jA_{j/i}-x_kA_{k/i}} - \frac{x_j(1-A_{i/j})}{1-x_iA_{i/j}-x_kA_{k/j}}-\frac{x_k(1-A_{i/k})}{1-x_iA_{i/k}-x_jA_{j/k}} \quad \text{Eq. 2.30}$$

Furthermore, an extended Miedema model was used in the calculation of $\ln\gamma_i$. Some necessary physical parameters in the Al-Ti-B ternary system were listed in their research. Based on the solubility limits of Ti and B in liquid Al, they calculated the excess free energy of Al-Ti-B system at 1000 K, in which the solubility of Ti in liquid Al was assumed less than 0.5 at. % and the concentration ratio between Ti and B atoms in the melt was 1:2. The excess free energies of AlB_2, Al_3Ti and TiB_2 were calculated as a function of the concentration of Ti dissolved in liquid Al at 1000 K. The related result was plotted in their research, as shown in Figure 2.4.

According to Fan et al. (2005), it is clear that the excess free energy for formation of AlB_2, Al_3Ti and TiB_2 generally follows the order of $\Delta G_{TiB_2} < \Delta G_{Al_3Ti} < \Delta G_{AlB_2}$, indicating that TiB_2 phase is much easier to form than Al_3Ti and AlB_2 in liquid Al. However, at the beginning of the mixed-salts reaction, Al_3Ti and AlB_2 are easier to form than TiB_2 due to the extremely low concentrations of Ti and B in the Al melt.

In addition, Jones and Pearson (1976) have offered an unconventional but practical phase diagram in the rich-Al corner at 1000 K, as shown in Figure 2.5. It is clear that there is no region including AlB_2 and Al_3Ti in the phase diagram, meaning that these two phases cannot stably coexist in the Al melt, which can react to form TiB_2 phase.

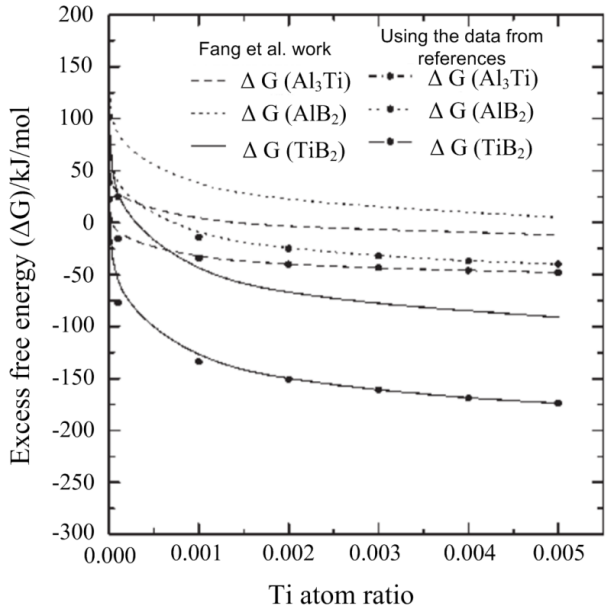

Figure 2.4 Excess free energy varied with the concentration of Ti dissolved in liquid Al at 1000 K.

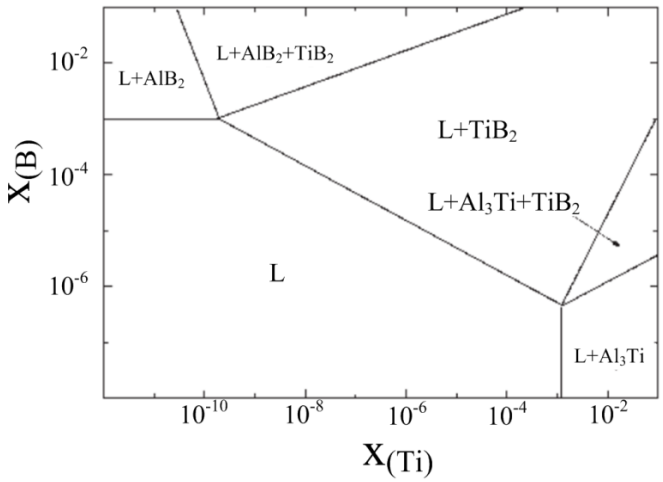

Figure 2.5 Phase diagram for Al-Ti-B system (Al corner), x represents the molar fraction, which is reproduced according to Jones and Pearson (1976).

It should be mentioned that the above thermodynamic study about the mixed-salts reaction is based on an equlibrium condition. The mixed-salts reaction, however, is a

typical non-equilibrium reaction. The formation of products is influenced not only by the thermodynamic factors, but also by the kinetic factors. The analysis of the formation of TiB_2 from a kinetic perspective is rather limited in the literatures. In order to clear display the formation process, more work should be done from the kinetic perspective.

Since this research aims to synthesize TiB_2 particulates in molten Al at low temperatures, the following section will discuss the influence of reaction temperature on the mixed-salts reaction.

2.2.3.3 Influence of Temperature on the Formation of TiB_2

The mixed-salts reaction of K_2TiF_6-KBF_4-Al system for synthesizing TiB_2 phase is a high-temperature reaction. As reported in the literatures, the temperatures of the Al melt used in the reaction are always higher than 800 °C. Generally, a lower temperature can lead to the formation of Al_3Ti phase, which decreases the yield of TiB_2 phase in the Al matrix (Christy, Murugan, & Kumar, 2010; Mandal, Maiti, Chakraborty, & Murty, 2004).

Kumar et al. (2008) synthesized TiB_2 particles by adding the mixed salts of K_2TiF_6 and KBF_4 into molten A356 alloy at 800 °C, and the size of in situ formed TiB_2 particulates was in the range of 0.5-1.5 μm. Han et al. (2002) also obtained in situ TiB_2 particles in Al-Si alloy at 800 °C, and the size of particulates was smaller than 1 μm. Xue et al. (2012) fabricated in situ TiB_2/2014 Al alloy composites at 870 °C by using mixed salts as the main reactants, and the size of TiB_2 particulates was below 2 μm.

Based on the above researchers' work, it is clear that a higher temperature can result in the formation of some TiB_2 particles with the size exceeding 1 μm. The existence of large-sized particles in the matrix, however, can result in the reduction of tensile properties of materials, especially for the ductility and yield strength (Doel & Bowen, 1996). Thereby, decreasing the formation of large-sized TiB_2 particulates is desired in most cases.

Till now, the study of synthesis of TiB_2 particulates via the mixed-salts reaction by using K_2TiF_6 and KBF_4 as the reagents at low temperatures (as low as 700 °C) has never been reported. It is believed that exploring a method of synthesizing TiB_2 particulates at much lower temperatures is attractive and more work should be done in this field.

2.3 Review of Al_3Ti Particulates Synthesized in Molten Al

2.3.1 Characteristics of Al_3Ti

Al_3Ti crystal has a tetragonal structure with a=b=0.385 nm and c=0.861 nm (Li, Wang, Zhao, Chen, Chen, & Cheng, 2010). Each unit cell contains two Ti atoms and six Al atoms. The related crystal structure of Al_3Ti is shown in Figure 2.6 (Wang, Jha, & Brydson, 2004). Due to its structure, Al_3Ti has its own particular characteristics, such as low density (3.4 g cm^{-3}), high Young's modulus (220 GPa), good wetability with Al and excellent mechanical properties at both ambient and elevated temperatures (Wright, Rabin, & McFerran, 1992; Wu, Zheng, & Li, 2000; Zhang, Xiao, Wang, & Ma, 2012). Particularly, Al_3Ti also has an excellent resistance to oxidation and corrosion in the fluoride atmosphere above the melting point of Al (Arnberg, Bäckerud, & Klang, 1982b).

Based on the above reasons, Al_3Ti, one promising particulate-reinforcement in the Al matrix, has been obtaining more and more attractions.

Furthermore, Zhang et al. (2005) have reported that Al_3Ti is a more powerful nucleating substrate for Al alloys than other reinforcements, meaning that Al_3Ti can decrease the Al grain size effectively. For reinforcing a material in terms of the heterogeneous nucleation, the interfacial energy between the nucleation substrate and the solid matrix is critical to the potency of the substrate. In the heterogeneous nucleation, the energy on the newly formed interface should be lower than that of the same area of the interface which formed directly in the liquid metal. To obtain the low interfacial energy, the substrate and the solid have to be coherent or partially coherent. The lattice matching between two solids can be evaluated by the following equation (Li & Wu, 2005):

$$\delta = \left| \frac{a_{matrix} - a_{substrate}}{a_{matrix}} \right| \qquad \text{Eq. 2.31}$$

where δ is the value of lattice misfit between the matrix and the substrate, a_{matrix} and $a_{substrate}$ are the lattice constants of the matrix and the substrate, respectively. Generally, when $\delta \leq 0.05$, the interface between the substrate and the matrix is coherent; when $0.05 < \delta < 0.25$, the interface between the substrate and the matrix is partially coherent.

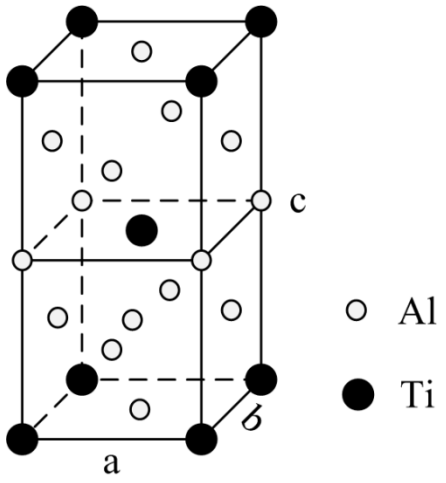

Figure 2.6 The crystal structure of Al_3Ti reproduced from Wang et al. (2004).

α-Al crystal has a fcc structure with a=b=c=0.404 nm (Sigworth, 1984). Thereby, the values of the lattice misfit between the Al and Al_3Ti in both a and c directions are 0.049 and 0.065, respectively. Obviously, in situ formed Al_3Ti phase has a good lattice matching with Al, and Al_3Ti particulates can work as the effective heterogeneous nucleation sites for primary Al in the solidification. Zhang et al. (2005) used the edge-to-edge matching model based on the excellent atomic matching between Al_3Ti and Al matrix to identify that Al_3Ti is the best grain refiner for Al alloys compared with TiC, TiB_2, and AlB_2.

In addition, according to Al-Ti phase diagram (as shown in Figure 2.7) (Sigworth, 1984), when the temperature cools down to 665 °C, the following peritectic reaction will take place:

$$L + Al_3Ti \xrightarrow{665^{\circ}C} \alpha Al \qquad \text{Eq. 2.32}$$

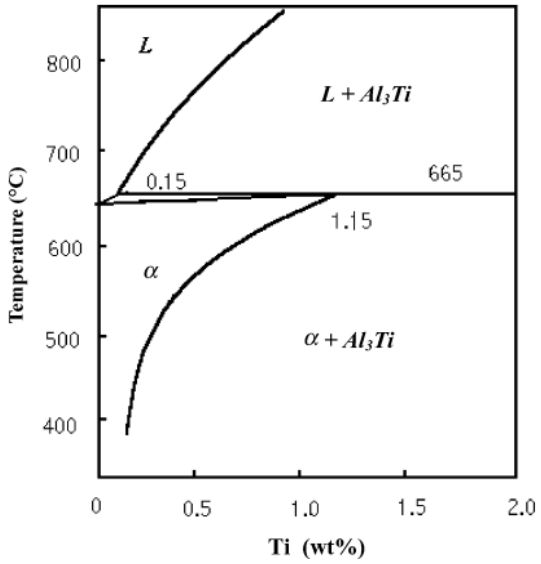

Figure 2.7 Aluminum-rich corner of the Al-Ti phase diagram reproduced according to Sigworth (1984).

In general, the solid phase in the peritectic reaction always has a strong nucleating effect, because the newly formed phase precipitates and grows more easily on the solid phase.

Based on the above introduction, Al_3Ti phase can work as the reinforcement, but also can serve as an effective nucleating agent in the Al alloys, which is one of the most important advantages for using Al_3Ti as the reinforcement in the Al composites. It has been reported that in situ formed Al_3Ti particulates could optimize the microstructures of Al alloys. α-Al crystals changed from dendritic to equiaxed morphology, and the grain size decreased as well, leading to improved mechanical properties (Liu, Rakita, Wang, Xu, & Han, 2014; Liu, Wang, Han, & Li, 2014).

2.3.2 Synthesis of Al_3Ti in Molten Al

In general, Al_3Ti particulates can be synthesized by adding the Ti bearing salt, such as K_2TiF_6 or the solid Ti powders (sometimes mixed with Al powders) into molten Al at high temperatures.

Chen et al. (2009) fabricated in situ Al_3Ti/Al composites by adding K_2TiF_6 into molten Al at 1100 °C. The related chemical formula regarding the formation of Al_3Ti phase in the reaction is given in Eq. 2.5. The Al_3Ti phase produced in their research was needle-like in morphology with the length exceeding 200 μm and width of 10 μm. Kori et al. (2014) synthesized Al_3Ti at a lower temperature (800 °C) using K_2TiF_6 as the additive. In their research, the in situ formed Al_3Ti particulates were block-like in shape with the size from 20 to 40 μm.

Yu et al.(2006b) directly added Ti and Al mixed powders into the Al melt with the temperature in the range of 900-1000 °C. The Al_3Ti particles were in situ formed according to the following chemical reaction:

$$3Al_{(l)} + Ti \xrightarrow{900\text{-}1000^{\circ}C} Al_3Ti \qquad \text{Eq. 2.33}$$

An interesting phenomenon was found in their research that the morphology and size of the in situ formed Al_3Ti particles were changed apparently with the increase of Al_3Ti content. Fine particle and a few of needle-like Al_3Ti (5-20 μm) were formed when the Al_3Ti content was lower; larger block Al_3Ti (30-150 μm) was formed at a higher Al_3Ti content.

Liu et al. (2013) added solid Ti powders into molten Al at 780 °C, and in situ formed Al_3Ti particulates were blocky in morphology with an average size of 5 μm.

It is evident that the temperature of molten Al can influence the morphology and size of Al_3Ti particulates significantly in the direct-melt reaction. The related content will be discussed in the following section.

2.3.3 Influence of Temperature on the Formation of Al_3Ti

Higher reaction temperatures can easily lead to the formation of needle-like Al_3Ti particulates, whereas blocky Al_3Ti particulates can be formed at lower reaction temperatures. The reason can be explained according to the Al-Ti phase diagram (Kwak, Mohney, Lin, & Kern, 2000), as shown in Figure 2.8. The solubility of Ti in molten Al increases as the temperature increases. For example, the solubility of Ti in molten Al at 1100 °C is much higher than that at 800 °C. At a higher temperature, more Ti element exists in molten Al as solute. Since the direct-melt reaction is an exothermic reaction, the actual temperature is higher than the original reaction temperature. Thereby, Al_3Ti phase produced in the reaction can easily dissolve into molten Al. When the temperature decreases, the solubility of Ti decreases, and Al_3Ti phase starts to nucleate and growth. As reported by John et al.(1979b), the Al_3Ti prefers the growth along <110> direction during the growth process. As a result, Al_3Ti particulates in needle-like shape were obtained. Direct-melt reaction between solid Ti powders and liquid Al at low temperatures (lower than 800 °C) can produce much smaller-sized blocky Al_3Ti particulates, indicating that the formation of Al_3Ti at the lower temperatures might be different from the higher temperatures. The detailed work will be discussed in the later part of the dissertation.

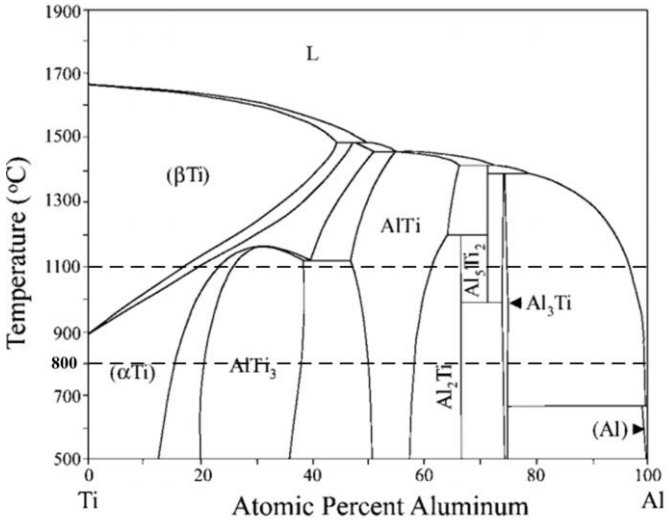

Figure 2.8 Al-Ti phase diagram reproduced according to Mohney et al. (2000).

2.4 Review about High-intensity Ultrasound

In this section the basics of high-intensity ultrasound, including its definition, main effects in a liquid phase, as well as its chemical effects, are introduced in detail.

2.4.1 Background of High-Intensity Ultrasound

Ultrasound is an oscillating sound, which spans the frequencies of roughly 15 kHz-10 MHz, with associated acoustic wavelengths in liquids roughly 100-0.1 mm (Suslick, Eddingsaas, Flannigan, Hopkins, & Xu, 2011). Generally, high-intensity ultrasound requires its intensity ≥ 10 Wcm^{-2} (Eskin, 1997). Abramov (1986) reported that propagation of high-intensity ultrasound in a liquid medium mainly causes acoustic cavitation and acoustic streaming. These non-liner effects lead to liquid agitation and homogenization, raise the rate of convective diffusion processes, and have an influence on the temperature distribution in the liquid medium. In addition, Suslick (1989)

mentioned that intense ultrasonic waves travelling through liquids generate small cavities that enlarge and implode, creating tremendous heat. These extreme conditions provide an unusual chemical environment.

2.4.2 High-Intensity Ultrasound in Liquids

2.4.2.1 Acoustic Cavitation

As described by Neppiras (1984), cavitation might occur "whenever a new surface, or cavity, is created within a liquid, a cavity being defined as any bounded volume, whether empty or containing gas or vapor, with at least part of the boundary being liquid". This general definition would cover such phenomena as boiling and effervescence, which involve only underwater expansion (or explosion) of the gas phase (Leighton, 1994). In the presence of a sound field not only expansion, but also contraction, of existing cavities will generally occur. According to Neppiras (1980), the term "acoustic cavitation" is therefore usually restricted to cases involving both expansion and contraction of cavities or bubble nuclei.

Suslick (1990) indicated that acoustic cavitation can be considered to involve at least three discrete stages: nucleation, bubble growth, and implosive collapse of bubble under proper conditions. More detailed description is that acoustic cavitation, indeed, is the production of cavities inside a liquid irradiated by ultrasound, due to the presence of microbubbles in the liquid (can be regarded as cavitation nuclei), filled with the liquid vapor and/or air, which can concentrate the acoustic energy in a small volume

(corresponding to the bubble growth) and give rise to macroscopic and visible effects (corresponding to the bubble collapse).

Formation of cavities in liquids is a nucleated process. A cavity can nucleate in the pure liquid, or more favorably, grow at weak points in the liquid, such as gas-filled crevices in suspended particulate matter or from transient microbubbles. Similar with solidification process, the former case can be termed as homogeneous nucleation and the latter one as heterogeneous nucleation.

The tensile strength of a liquid refers to the tension which a liquid can support without breaking (cavitating). As regards to acoustic phenomena, to a first approximation a liquid is put into tension when the acoustic pressure amplitude exceeds the static ambient pressure, such that the pressure in the liquid becomes negative, as shown in Figure 2.9. Due to the generation of negative pressure in liquid, the liquid can be tore apart, and then the cavity can be formed filling with liquid vapor and/or gases that are dissolved within the liquid. Accordingly, the initial homogeneous cavitation nuclei are formed. Actually, the theoretical tensile strength of a pure, homogeneous liquid is great, and the pressures of the order of several hundreds of bars are needed in order to disrupt a liquid (Alippi, Galbato, & Cataldo, 1992),which precludes cavity formation easily from the negative pressure of an acoustic expansion wave.

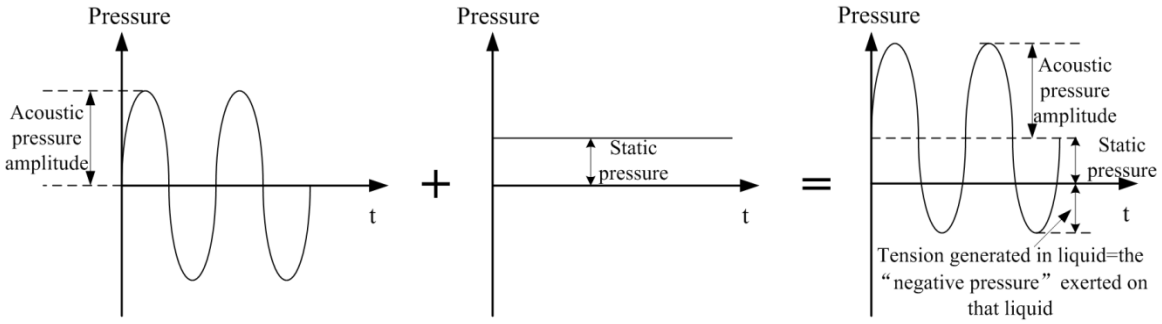

Figure 2.9 When an acoustic wave passes through a liquid, the pressure in a liquid is the sum of static and oscillating terms. If the acoustic pressure amplitude is greater than the static pressure, the pressure in the liquid will be negative for part of each acoustic cycle, and at this moment the liquid is in tension.

In most practical situations the liquid involved is a complex system, containing many impurities (such as small gas bubbles and solid contaminations on which gas bubbles can adhere, etc.). These impurities can act as weakness which can decrease the tensile strength of liquid significantly. Numerous researchers have verified this phenomenon by experiments and obtained an important conclusion: that is not the properties of the liquid determine the maximum tension a liquid can sustain, but often the other bodies present within the liquid sample (Leighton, 1994) These preexisting gas microbubbles can work as the cavitation nuclei, which are termed as heterogeneous cavitation nuclei. Indeed, similar to solidification, heterogeneous nuclei are dominated in the acoustic cavitation inception.

Pressure fluctuations in the liquid, induced by flow, or by the passage of an acoustic wave (such as ultrasound) through the liquid etc., might cause the generation of free-floating bubbles from the cavitation nuclei, which can be either microbubbles adhered to the impurities, or gas-pockets trapped within crevices in motes or the container walls (Leighton, 1994).

In order to recognize the bubble growth in a liquid irradiated with ultrasound well, the response of a bubble to a static pressure should be clarified. Blake (1949) made a pioneering work on this issue. In his work, a spherical microbubble of radius R in static equilibrium in a liquid is considered, as shown in Figure 2.10. The microbubble contains gas and vapor, and the pressures of which are p_g and p_V, respectively. If the liquid is initially in a static equilibrium, the pressure throughout the liquid, including the pressure at very large distance from the bubble (p_∞) and that immediately outside the bubble (p_L), equals the hydrostatic pressure p_0. If the tensile strength of liquid is σ, then the equilibrium of the interface requires the following condition to be satisfied:

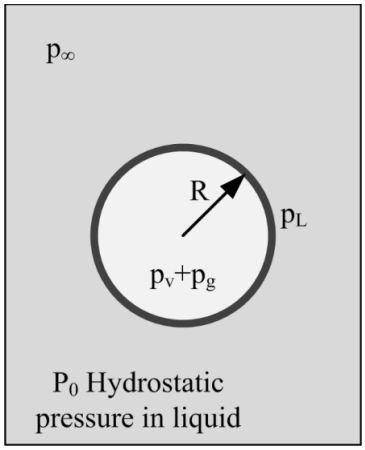

Figure 2.10 A spherical microbubble in static equilibrium in a liquid.

$$p_L + \frac{2\sigma}{R} = p_v + p_g \qquad \text{Eq. 2.34}$$

When the Eq. 2.34 is initially applied at the equilibrium position, $R = R_0$, $p_L = p_0$, and $p_g = p_{g,e}$. Since the vapor pressure is always p_V, Eq. 2.34 can be expressed as:

$$p_0 + \frac{2\sigma}{R_0} = p_v + p_{g,e} \qquad \text{Eq. 2.35}$$

$$p_{g,e} = p_0 - p_v + \frac{2\sigma}{R_0} \qquad \text{Eq. 2.36}$$

Image that the pressure in the liquid changes from p_0 in a quasi-static manner, and such that the pressure outside the bubble is p_L. Since the change is quasi-static, the pressure throughout the liquid is spatially uniform and also equals to p_L. The bubble radius will change from R_0 to R in response to the change in liquid pressure. As the gas pressure is inversely proportional to the volume in an isothermal transformation, the p_g can be given as:

$$p_g = p_{g,e}(\frac{R_0}{R})^3 = (p_0 - p_v + \frac{2\sigma}{R_0})(\frac{R_0}{R})^3 \qquad \text{Eq. 2.37}$$

Substitute Eq. 2.37 into Eq. 2.34, giving the pressure in the liquid immediately beyond the bubble wall is:

$$p_L = (p_0 - p_v + \frac{2\sigma}{R_0})(\frac{R_0}{R})^3 + p_v - \frac{2\sigma}{R} \qquad \text{Eq. 2.38}$$

As stated, the process of bubble from initial stage to new stage undergoes a quasi-static change. Accordingly, the pressure in the liquid remote from the bubble equals the liquid pressure at the ball wall, i.e. $p_\infty = p_L$.

Eq. 2.38 determines the position of the new equilibrium after the liquid pressure has changed uniformly and quasi-statically from p_0 to p_L. It can be imaged simply that, when the p_L increases, the liquid pressure will be positive and greater than before

($p_L > p_0$), and then the bubble in liquid will contracted. This position of equilibrium is stable, since the positive pressure will assisted the surface tension pressure in confining the gas. When p_L decreases, but its value is still positive ($0 < p_L < p_0$), the bubble in liquid will expend and still be stable.

In contrast, when p_L becomes negative ($p_L < 0$), it can begin to counteract the confining effect of surface tension pressure of the bubble wall. After the bubble is larger than some critical radius, the pressure balance across the bubble wall cannot be maintained longer, and the bubble will grow explosively until to collapse. It is clear that after the bubble grows exceeding the critical radius, the system will become unstable. After the start of such instability, it is not reasonable to predict the bubble behavior by using the above equilibrium.

One important thing should be mentioned is that the Blake model just accounts for surface tension effects in the quasi-static case, but the inertial and viscous effects of the liquid are not considered in this model. Thereby, it can never describe the explosive growth. However, in some special situations that are quasi-static and where surface tension dominates inertial and viscous effects, it might be valid to predict the explosive growth of the bubbles.

In addition, one important parameter "the critical radius" (R_{crit}) which a nucleus must exceed if it is to become unstable with respect to further expansion, can be calculated in the Blake mode by differentiating Eq. 2.38 with respect to R:

$$\frac{\partial p_L}{\partial R} = -\frac{3(p_0 - p_v + \frac{2\sigma}{R_0})R_0^{\,3}}{R^4} + \frac{2\sigma}{R^2} \qquad \text{Eq. 2.39}$$

when $\partial p_L/\partial R=0$, the critical radius is given by:

$$R_{crit} = \sqrt{\frac{3R_0^{\,3}}{2\sigma}(p_0 - p_v + \frac{2\sigma}{R_0})} \qquad \text{Eq. 2.40}$$

Similarly, there is a minimum in p_L by substituting R_{crit} into Eq. 2.38, and then the critical liquid pressure is:

$$p_{L(crit)} = p_v - \frac{4\sigma}{3R_{crit}} = p_v - \frac{4\sigma}{3}\sqrt{\frac{2\sigma}{3(p_0 + \frac{2\sigma}{R_0} - p_v)}} \qquad \text{Eq. 2.41}$$

If p_L is less than $p_{L(crit)}$ (i.e. more negative than it), there will be rapid uncontrolled bubble growth. In most cases, a term known as the Blake threshold pressure (p_B) is used to define the critical value of the liquid pressure. p_B represents the difference between the critical value and the original hydrostatic pressure in liquid, as shown in Eq. 2.42:

$$p_B = p_0 - p_{L(crit)} = p_0 - p_v + \frac{4\sigma}{3}\sqrt{\frac{2\sigma}{3(p_0 + \frac{2\sigma}{R_0} - p_v)}} \qquad \text{Eq. 2.42}$$

If the surface tension dominates (i.e. $2\sigma / R_0 >> p_0$, making sure Blake threshold is valid), and vapor pressure is neglected, the Eq. 2.42 can be simplified as:

$$p_B \approx p_0 + 0.77\frac{\sigma}{R_0} \qquad \text{Eq. 2.43}$$

As mentioned above, Blake mode is not suitable to describe the bubble growth and collapse in the practical situations, and the related issues can be studied through the bubble dynamic. The first pioneering study about bubble dynamic was made by Rayleigh

(1917), who solved the problem of the collapse of an empty spherical cavity in an incompressible liquid. In his study, the cavity is assumed to have a radius R_m when the bubble wall velocity is zero. Under the hydrostatic pressure p_∞ the cavity is contracted to a radius R with the bubble wall velocity R'. During this process, the work done simply equals the kinetic energy of the liquid, which can be obtained by integrating the energy over spherical shells of liquid, of thickness Δr, mass $4\pi r^2 \Delta r$, and the liquid velocity r' at a certain distance r (greater than R).

$$\frac{4\pi}{3} p_\infty (R_m{}^3 - R^3) = \frac{1}{2}\int_R^\infty r'^2 \, \rho 4\pi r^2 dr = 2\pi\rho R'^2 \, R^3 \qquad \text{Eq. 2.44}$$

where ρ is the liquid density. Since the fluid is incompressible, the whole motion is determined by that of the inner boundary, then:

$$\frac{r'}{R'} = \frac{R^2}{r^2} \qquad \text{Eq. 2.45}$$

By substituting Eq. 2.45 into Eq.2.44:

$$R'^2 = \frac{2p_\infty}{3\rho}\left(\frac{R_m{}^3}{R_3} - 1\right) \qquad \text{Eq. 2.46}$$

Integration of Eq. 2.46 with respect to time gives the collapse time t of the cavity:

$$t = \int_{R_m}^{R=0} \frac{dR}{R'} \approx 0.915 R_m \sqrt{\frac{\rho}{p_\infty}} \qquad \text{Eq. 2.47}$$

In addition, with neglect of surface tension and liquid viscosity and with the assumption of liquid incompressibility, Rayleigh (1917) also showed the motion of the bubble wall as follows:

$$RR''+\frac{3}{2}(R')^2=\frac{p(R)-p_\infty}{\rho} \qquad \text{Eq. 2.48}$$

where R'' is the derivative of R'. Since 1917, many researchers have contributed a lot on this research (Lohse, 2003; Neppiras & Noltingk, 1951; Noltingk & Neppiras, 1950; Plesset, 1949; Plesset & Prosperetti, 1977; Poritsky, 1951). The radial motion of an acoustically driven bubble can be described any of a family of equations related to the Rayleigh-Plesset equation (RPE). RPEs can vary in complexity, and the following is one example of them (Suslick, Eddingsaas, Flannigan, Hopkins, & Xu, 2011):

$$RR''+\frac{3}{2}(R')^2=\frac{1}{\rho}\left[(p_0+\frac{2\sigma}{R_0})(\frac{R_0}{R})^{3\gamma}-\frac{2\sigma}{R}-\frac{4\mu R'}{R}+p_\infty\right] \qquad \text{Eq. 2.49}$$

where μ is the shear viscosity of liquid. The left side of Eq. 2.49 describes the inertial characteristics of the bubble interface. The first term on the right side represents the intra-cavity gas pressure as the bubble radius varies from R_0 to R. The RPE can be used to solve for the time-varying bubble radius. According to Suslick et al. (2011), the bubble growth and collapse process at 20 kHz is shown qualitatively in Figure 2.11. It clearly shows that bubble subjected to oscillatory pressure at 20 kHz undergoes expansion and then collapses. Bubble collapse during cavitation generates transient hot spots responsible for high-energy chemistry. The cycle of single acoustic cavitation is rather short, which is shorter than 40 μs, indicating that high-intensity ultrasound is able to effectively activate the chemical reaction in a liquid in a very short time.

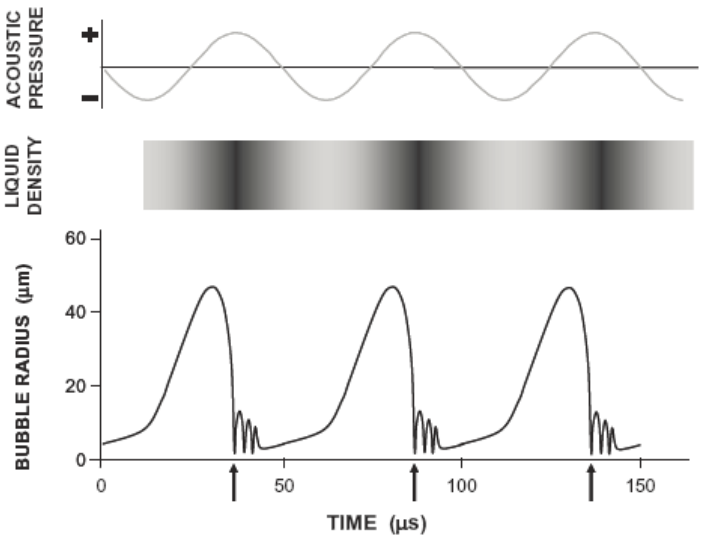

Figure 2.11 Bubble growth and collapse during single cavitation at 20 KHz. The origin of sonochemistry occurs (as indicated by the arrows) at the point of maximum bubble compression.

2.4.2.2 Acoustic Streaming

Acoustic streaming is a macroscopic movement of fluid induced by acoustic wave (Sakharov, Hekkenberg, & Rijken, 2000). As the acoustic wave travels the liquid medium, it may be absorbed (attenuation phenomenon). The momentum absorbed from the acoustic field manifests itself as a flow of the liquid in the direction of the sound field, termed as acoustic streaming (Hyun, Lee, & Loh, 2005; Leighton, 1994).

When ultrasound propagates through a liquid, absorption of energy from the acoustic beam results in an energy density gradient becoming established in the direction of propagation. A gradient in energy corresponds to a force, and liquid flow can occur when adding the energy gradient in the liquid. The relationship can be expressed by the following equation (Starritt, Duck, & Humphrey, 1991):

$$\vec{\nabla} p = \frac{F}{V} = \frac{2I\alpha}{C} \qquad \text{Eq. 2.50}$$

where $\vec{\nabla} p$ is the gradient in pressure, $\frac{F}{V}$ represents the force per unit volume, I is the intensity, α the absorption, and c the speed of sound in liquid. It is clear that if both intensity and attenuation can vary spatially throughout a sound beam in a liquid, then so will the streaming forces and flows. An increase in either parameter will increase the acoustic streaming.

In addition, there is a second type of acoustic streaming, i.e. acoustic streaming occurs near small obstacles placed within a sound field, or vibrating membrane or bounding walls (Nyborg, 1958). It arises from the frictional forces between a boundary and a medium carrying vibrations with a frequency of ω. This time-independent circulation occurs only in a small region within liquid, leading to form an acoustic microstreaming boundary layer. The thickness of the layer can be estimated by:

$$L = \sqrt{2\eta / \rho\omega} \qquad \text{Eq. 2.51}$$

where η and ρ are the shear viscosity and density of liquid, respectively (Leighton, 1994; Nyborg, 1958). Due to the restricted scale of the circulation, it is commonly termed as microstreaming.

Acoustic streaming in a liquid can generate the liquid flow, which can accelerate the mass and thermal transfers in the liquid, making the liquid more homogeneous. Furthermore, microstreaming can bring about some important effects resulting from the shear forces generated in the liquid. Thereby, it can be used to disrupt particle clusters in the Al melt for fabricating particulate reinforced Al composites (Liu, Han, Li, & Huang,

2012; Liu, Rakita, Han, & Li, 2011; Liu, Han, & Li, 2011), disrupt DNA and disaggregate bacteria, etc. (Williams, 1974; Williams & Slade, 1971).

2.4.3 Chemical Effects of Ultrasound

Many researchers have proposed that the chemical effects of ultrasound do not derive from a direct interaction of the ultrasonic field with chemical species on a molecular level (Mason & Lorimer, 2002; Suslick, 1988; Suslick, 1990; Suslick, Eddingsaas, Flannigan, Hopkins, & Xu, 2011). In his research, Suslick (1990) mentioned that the acoustic wavelengths in liquids irradiated with ultrasound are roughly in the range of 0.1-100 mm, which is not on the scale of molecular dimensions. Further Suslick indicated that ultrasound is able to cause high-energy chemistry through the process of acoustic cavitation in a liquid.

2.4.3.1 Ultrasonic Cavitation in Liquids

Cavitation serves as a mean of concentrating the diffuse energy of ultrasound in liquids. The implosion of cavities establishes an unusual environment for chemical reactions. It can produce intense local heating (local hot spot) and high pressure due to the compression of the gases and vapors inside the cavity in a very short time (a few microseconds) (Suslick, Hammerton, & Cline, 1986). The temperatures and pressures of hot sports can reach to approximate 5000 °C and 500 atmospheres, respectively (Suslick, 1989, 1990). Even though the temperature of this region is extreme high, the reign is so small that the heat can dissipate quickly. Thereby, the extreme rapid heating and cooling

rates (greater than 10^9, or 10^{10} K/s) surrounding the cavity can be obtained. An extreme chemical condition can be created in the liquids irradiated with high-intensity ultrasound, which can affect chemical reactions deeply comparing with the conventional methods.

In addition to extreme temperatures and pressures, cavity implosion in the form of spherical collapse also produces shock waves in the surrounding liquid. It has remarkable effects on the liquid-solid interfaces (such as solid particles and extended solid surfaces) in the liquids. The shock wave and acoustic streaming both can promote the mass transfers in the chemical reactions, leading to accelerated reactions.

2.4.3.2 Ultrasound in Liquid-Solid Systems

Of course the above extreme high temperature, pressure and rapid heating and cooling rates can also be generated in liquid-solid systems. There are two main proposed mechanisms for the effects of cavitation on the liquid-solid interfaces: shock wave and micro-jet.

On the one hand, shock waves created by cavity collapse in a liquid can induce surface damage and the fragmentation of brittle materials. On the other hand, due to the existence of shock waves, the ultrasonic irradiation of liquid-solid (powder) suspensions produces a very important effect: high velocity interparticle collisions. The shock waves can cause small particles to collide into one another with great force and the impact velocities ranging from 100-500 m/s for particles ~ 10 μm. The interparticle collisions can introduce remarkable changes in surface morphology, composition and reactivity (Doktycz & Suslick, 1990; Suslick, 1990; Suslick & Price, 1999).

Cavitation near an extended surface is very different from the shock waves mentioned above. Near an extended solid surface, cavity collapse is nonspherical, driving high-speed jets of liquid (termed as micro-jets can reach velocities of hundreds of meters per second) into the surface and creating damage to the surface (Suslick & Price, 1999). This process can produce newly exposed, highly heated surfaces (Suslick, 1990). Since it was reported by Kornfeld & Suvorov (1944) that liquid micro-jets is a dominant factor in cavitation damage, the jet behavior has been studied by numerous researchers (Blake & Gibson, 1987; Lauterborn & Bolle, 1975; Nyborg, 1958; Plesset & Chapman, 1971; Tomita & Shima, 1986). Figure 2.12 shows a comparison between the reentrant jet development in a bubble collapsing near a solid wall as observed by Lauterborn & Bolle (1975) and as computed by Plesset & Chapman (1971).

Actually, the impingements of micro-jets and shock waves on the surface both can induce the damage to the surface. The existence of both mechanisms has been established, but their relative importance is still a matter of debate and probably depends on the method by which cavitaion is generated (Suslick, 1990).

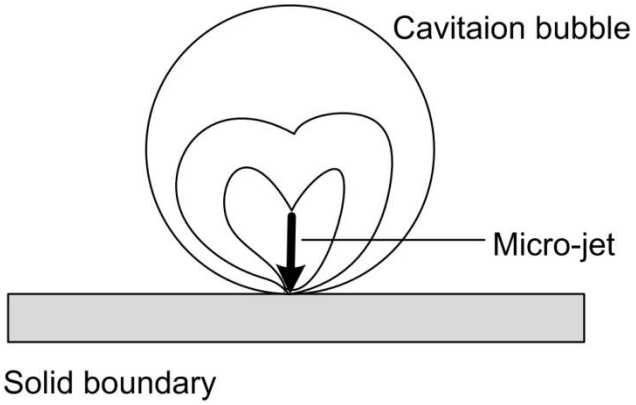

Figure 2.12 The collapse of a cavitation bubble close to a solid boundary in a liquid to generate the micro-jet, the graph is reproduced based on the work from Plesset & Chapman (1971), Lauterborn & Bolle (1975), and Brennen (2013).

Suslick et al. (1999) proposed that micro-jet distortions of bubble collapse depend on a surface several times larger than the resonant bubble size. For example, for solid particles smaller than ~ 200 μm, micro-jet formation cannot occur with ultrasonic frequency of 20 kHz. In these cases, the shock waves created by cavitational collapse can create high velocity interparticle collisions.

It is well known that ultrasound has strong effects on the solid phase in the liquid. Therefore, the chemical reactions of liquid-solid systems in ultrasonic fields should become more active.

CHAPTER 3. METHODOLOGY

The goal of this dissertation is to explore low-temperature synthesis of TiB_2 and Al_3Ti particulates in molten Al by using high-intensity ultrasound. Two typical synthesizing methods are studied: the mixed-salts reaction of K_2TiF_6-KBF_4-Al for fabricating TiB_2 and the direct-melt reaction between solid Ti powders and liquid Al for producing Al_3Ti.

The formation mechanisms of TiB_2 and Al_3Ti in molten Al and the effects of ultrasound on their formations at low temperatures are both investigated in this research. In order to clearly introduce the research methodology, the detailed experimental preparations and analyses about the two reactions are given below individually.

3.1 Mixed-salts Reaction for Synthesizing TiB_2

3.1.1 Raw Materials and Preparation

Potassium hexafluorotitanate (K_2TiF_6, 98% purity) and potassium tetrafluoroboride (KBF_4, 98% purity) were used as the reagents. Pure Al ingot was used as the matrix in order to avoid the possible influences of alloying elements on the reaction. The K_2TiF_6 and KBF_4 salts with a molar ratio of Ti/B=1/2 were mixed sufficiently by using a glass mortar. The amount of mixed salt powders added

corresponded to the composition of Al-5 wt. %TiB_2. The amounts of K_2TiF_6 and KBF_4 added into the Al melt were calculated according to the chemical formula (Eq. 2.8). Assuming the weight of initial Al is M_{Al} (g), and considering the loss of Al during the reaction, the quantities of K_2TiF_6 and KBF_4 could be obtained by:

$$M_{K_2TiF_6} = 2.67 \times 0.06398 \bullet M_{Al} \quad \text{Eq. 3.1}$$

$$M_{KBF_4} = 2.8 \times 0.06398 \bullet M_{Al} \quad \text{Eq. 3.2}$$

3.1.2 Samples Fabricated with Different Temperature and Time

In order to investigate the influences of reaction temperature and time on the formation of TiB_2 particulates in molten Al regarding the yields and size distributions of TiB_2 particulates, three reaction temperatures (900, 800 and 700 °C) with two reaction times (10 and 30 min) were studied, as shown in Table 3.1. Thereby, 6 samples were fabricated in total. For simplicity, the 6 samples were referred as S900-10, S900-30, S800-10, S800-30, S700-10, and S700-30, respectively (the first and second numbers stands for the reaction temperature and time in each sample). Taking S900-10 as an example, the detailed preparation process is given below.

A 300 g pure Al ingot was melted in a graphite crucible in an electrical resistant furnace. After the temperature of the Al melt reached and kept stable at 900 °C, the mixed K_2TiF_6-KBF_4 powders were added into the Al melt. And then the melt was stirred manually for a few seconds by using a niobium bar. After 10 min, the Al melt containing reaction products was stirred again, for the newly formed products might deposit during the reaction due to the higher density than pure Al, and then the slag on the melt surface

was removed before pouring the melt into a steel mold to form an ingot. For the samples fabricated in 30 min, the melt was stirred in 10 min intervals.

Table 3.1 *Samples fabricated under different experimental parameters.*

Composition	Sample Name	Reaction Temperature (°C)	Reaction Time (min)
Al-5 wt. % TiB_2	S900-10	900	10
	S900-30	900	30
	S800-10	800	10
	S800-30	800	30
	S700-10	700	10
	S700-30	700	30

3.1.3 Ultrasound Assisted Mixed-salts Reaction

A 300 g pure Al ingot was melted in a graphite crucible in an electrical resistance furnace. An ultrasonic Nb probe with a cross sectional area of about 5.06 cm^2 was immersed into the melt and the temperature of the melt was remained stable at around 700 °C. The mixed salt powders were added into the melt. In the meantime, high-intensity ultrasound was introduced the melt. The experimental setup is illustrated in Figure. 3.1. In the fabricating process, the Nb probe tip was immersed into molten mixed salts by less than 1 cm. The melt was treated by ultrasound for 10 min, and the slag floating on the top of the melt was removed before pouring the melt into a steel mold to form an ingot. This sample was referred to as an ultrasonically treated sample (UTS700-

10 sample). The power of the ultrasonic generator was 1.5 kW and the frequency was 20 kHz.

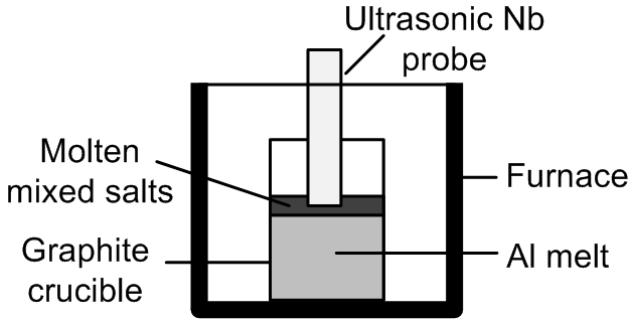

Figure 3.1 Schematic diagram of ultrasound assisted the mixed-salts reaction for synthesizing TiB_2 particles.

3.1.4 Extraction Experiment for Obtaining TiB_2 Particles

In this research, some TiB_2 particles were extracted from the samples for calculating the yield of TiB_2 particulates in each sample, as well as measuring the size distribution of TiB_2 particulates. The detailed extraction procedure for obtaining TiB_2 particles is given below.

1. A small ingot was cut from the sample, and the surface of which was cleaned by sand paper.

2. The small ingot was dissolved in a 15 vol. % aqueous HCl solution in a beaker at room temperature. After dissolution, a layer of particles were deposited at the bottom of the beaker, and then the HCl solution was decanted.

3. TiB_2 particles were washed with water for several times until the supernatant displayed neutral pH.

4. These TiB_2 particles were washed with ethanol, and then dried by using an electric hair dryer.

Since this research mainly concerned the synthesis of TiB_2 particles, aqueous HCl solution was used as the etchant based on the following considerations. TiB_2 can exist stably in HCl solution, whereas other compounds, such as Al_3Ti and AlB_2 can be dissolved. By which, the interference of other phases can be eliminated in the following calculation of the yields of TiB_2 particulates and measurement of their size distributions.

3.1.5 Samples Analysis

3.1.5.1 Grinding and Polishing Processes

The sample was ground using SiC sand papers successively following the order of 180, 240, 400 and 600 mesh. Then the ground sample was polished using micro-sized diamond compound, following the order of 3 and 1μm. After that the polished sample was cleaned in the ultrasonic cleaner for a few minutes to clean the polished surface.

3.1.5.2 XRD Analysis

The products of the mixed-salts reactions, including the slags and the samples, were examined by x-ray diffraction (XRD, Bruker D8) using Cu Kα radiation at 40 kV and 40 mA and a scan rate of 0.10 °/s. The extracted particles from each sample were also analyzed by XRD to examine the purity of TiB_2 particles.

3.1.5.3 Microstructure Analysis

The microstructures of samples were analyzed by scanning electron microscopy (SEM, s4800) equipped with an energy dispersive spectroscope (EDS) device for

identifying the components in the samples. Some samples were also examined by using optical microscopy (OM).

3.1.6 Calculating the Yields of TiB_2 Particulates

In order to evaluate the degree of the mixed-salts reaction and the efficiency of ultrasound on the formation of TiB_2 particulates, the yield of TiB_2 in each sample was calculated. Two small ingots with a weight of about 8 grams cut from each sample were treated by a completed extraction process, respectively. Two groups of extracted powders were weighted by using an electric balance. And then the actual weight percentage of TiB_2 phase in the Al matrix could be calculated. Since the sample was fabricated corresponding to the composition of Al-5 wt.% TiB_2, the yield of TiB_2 could be further obtained. In the end, an average value of the yield was computed in order to decrease the experimental error.

3.1.7 Measuring the Size Distributions of TiB_2 Particulates

Zetasizer Nano ZS (Malvern) was used to measure the size distributions of TiB_2 particulates extracted from each sample. This device was able to measure the particles with the size ranging from 3 nm to 5 μm. Before the test, a small amount of TiB_2 powders were diluted with DI water. 10 measurements were conducted for each sample, and statistical analyses regarding the results were also provided.

3.2 Static Experiment for the Mixed-salts Reaction

3.2.1 Experimental Process

A 10 g pure Al ingot was melted in a small graphite crucible in an electrical resistant furnace. After the temperature reached 800 °C, the Al melt was kept 30 min in the furnace to guarantee a stable temperature. And then the mixed K_2TiF_6-KBF_4 salts were added into the Al melt. After 10 s, the crucible was taken out from the furnace stably, which was naturally cooled down in the air. After solidification, a small sample containing reaction products was obtained.

3.2.2 Preparation and Analysis of the Static Sample

1. The static sample was cut in half along its longitudinal axis, and then the longitudinal section of sample was ground and polished.

2. The microstructure of sample, especially the region containing products was observed by optical microscopy (OM) and scanning electron microscopy (SEM) for detailed information about the products.

3.3 Direct-metal Reaction between Solid Ti Powders and Liquid Al

In this research, the direct-melt reactions between solid Ti powders and liquid Al at low temperatures (730 and 700 °C) without and with ultrasound were investigated. The two synthesizing temperatures were much lower than those used in the conventional methods by at least 200 °C. In order to study the evolution of solid Ti powders in the Al melt, some samples with different reaction times were taken out during the fabricating process. The detailed experimental plan is given in Table 3.2.

Table 3.2 *Experimental design for synthesizing Al_3Ti particulates.*

Composition	Temperature (°C)	With/Without Ultrasound	Reaction Time (min)			
Al-3 wt.% Ti	730	Without	1	3	5	10
	730	With	1	3	5	10
	700	Without	-	-	-	10
	700	With	-	-	5	10

3.3.1 Raw Materials and Experimental Process

Pure Al ingot (99.5 % commercial purity) and solid Ti powders (99.7 % commercial purity, average size of 20 μm) were used as the reactants. A 300 g Al ingot was melted in a graphite crucible in an electrical resistant furnace. When the temperature of molten Al was stable at 730 °C, solid Ti powders were added into the Al melt. In the meantime, high-intensity ultrasound was introduced in the melt by immersing a Nb radiator (or probe), as shown in Figure 3.2. The amount of solid Ti powders added into the Al melt corresponded to the composition of Al-3 wt.% Ti. During the reaction process, four ultrasonically treated samples were taken out from the melt after 1, 3, 5 and 10 min. For simplicity, the four samples were referred as UTS730-1, UTS730-3, UTS730-5 and UTS730-10, respectively. The power of ultrasonic generator was 1.5 kW, with the frequency of 20 kHz. The other four control samples without ultrasonic treatment were taken out from the melt after the same time intervals for making a comparison, which were referred as S730-1, S730-3, S730-5 and S730-10, respectively. Similarly, the samples fabricated at 700 °C were referred as UTS700-5 and UTS700-10 samples (with ultrasound), and S700-10 sample (without ultrasound).

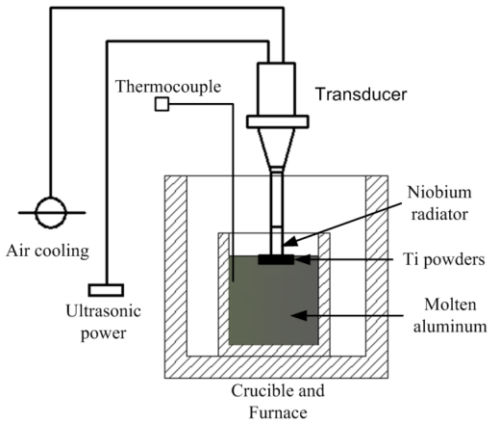

Figure 3.2 Schematic diagram of ultrasonic vibration assisted the direct-melt reaction between solid Ti powders and liquid Al.

3.3.2 Samples Analysis

3.3.2.1 Grinding and Polishing Processes

The samples obtained from the experiments were ground using SiC sand papers successively following the order of 180, 240, 400 and 600 mesh. And then the ground samples were polished using micro-sized (3 μm) diamond compound. After that the polished samples were cleaned in the ultrasonic cleaner for a few minutes to clean the polished surfaces.

3.3.2.2 XRD Analysis

The phases in the samples were examined by X-ray diffraction (XRD, Bruker D8, Germany) by using Cu Kα radiation at 40 kV and 40 mA and a scan rate of 0.10 °/s.

3.3.2.3 Microstructure Analysis

The microstructures of the samples were observed by scanning electron microscopy (SEM, s4800) equipped with an energy dispersive spectroscopy (EDS) device.

CHAPTER 4. EXPERIMENTAL RESULTS

The experimental results obtained from the mixed-salts reaction of K_2TiF_6-KBF_4-Al system and the direct-melt reaction between solid Ti powders and liquid Al are presented in this chapter, respectively.

Firstly, the results of the mixed-salts reactions at three different reaction temperatures (900, 800 and 700 °C) with two different reaction times (10 and 30 min) are summarized, including the phase compositions and microstructures of the samples, as well as the yields and size distributions of TiB_2 particulates. The results of ultrasound assisted mixed-salts reaction at 700 °C are also presented.

Secondly, the results of the static experiment for mixed-salts reaction are also provided in this chapter.

In addition, the results of the direct-melt reaction at different reaction temperatures (730 and 700 °C) with different reaction times (1, 3, 5, and 10 min) without and with ultrasound are provided, in which the phase compositions and microstructures of samples are examined.

4.1 Results of the Mixed-salts Reaction

4.1.1 Results of the Mixed-salts Reaction at 900 °C

4.1.1.1 S900-10 Sample

1) XRD Analysis of the Products

Figure 4.1 shows the XRD patterns of the slag and sample produced at 900 °C with a 10-min reaction time. It is obvious that $KAlF_4$ and K_3AlF_6 were the two main phases in the slag, as shown in Figure 4.1a, indicating that Ti and B elements were both transferred from the molten mixed salts to molten Al. In the S900-10 sample, TiB_2 was the only newly formed phase during the mixed-salts reaction, the diffraction peaks of which could be observed clearly, as shown in Figure 4.2.b. The results of the two XRD patterns indicate that the chemical formula shown in Eq. 2.8 is more suitable to describe the process of the mixed-salts reaction of K_2TiF_6-KBF_4-Al system.

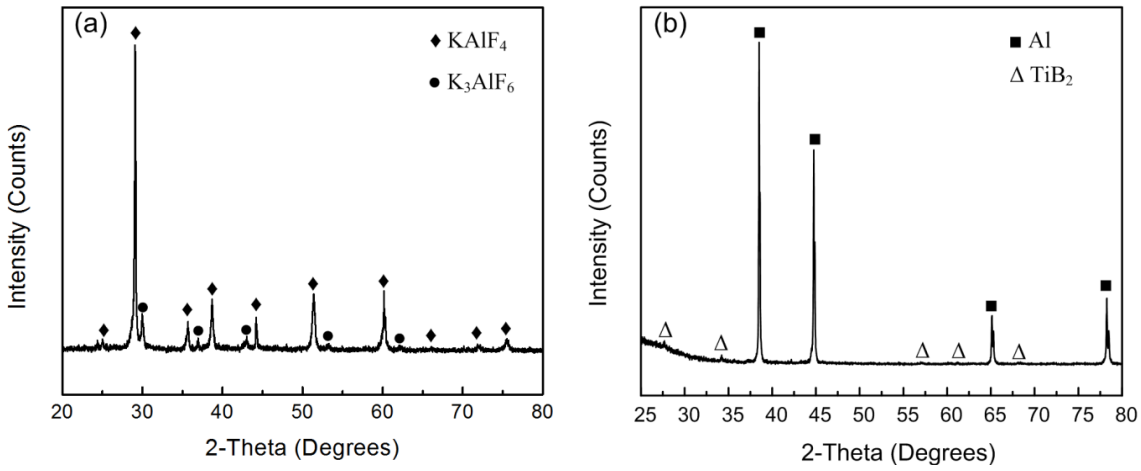

Figure 4.1 XRD patterns of the slag (a), and S900-10 sample (b) produced at 900 °C with a 10-min reaction time.

2) Microstructure Analysis of S900-10 Sample

Figure 4.2 shows the typical microstructure of the S900-10 sample. Only one type of newly formed phase existed in the Al matrix, which was identified as TiB_2 by EDS. These small-sized TiB_2 particulates aggregated to form clusters at α-Al grain boundaries, as shown in Figure 4.2a. Figure 4.2b clearly shows that these TiB_2 particulates synthesized via the mixed-salts reaction had different sizes, and most of them were much smaller than 1 μm. In Figure 4.3c, it can be found that some TiB_2 particulates had a larger size exceeding 1 μm.

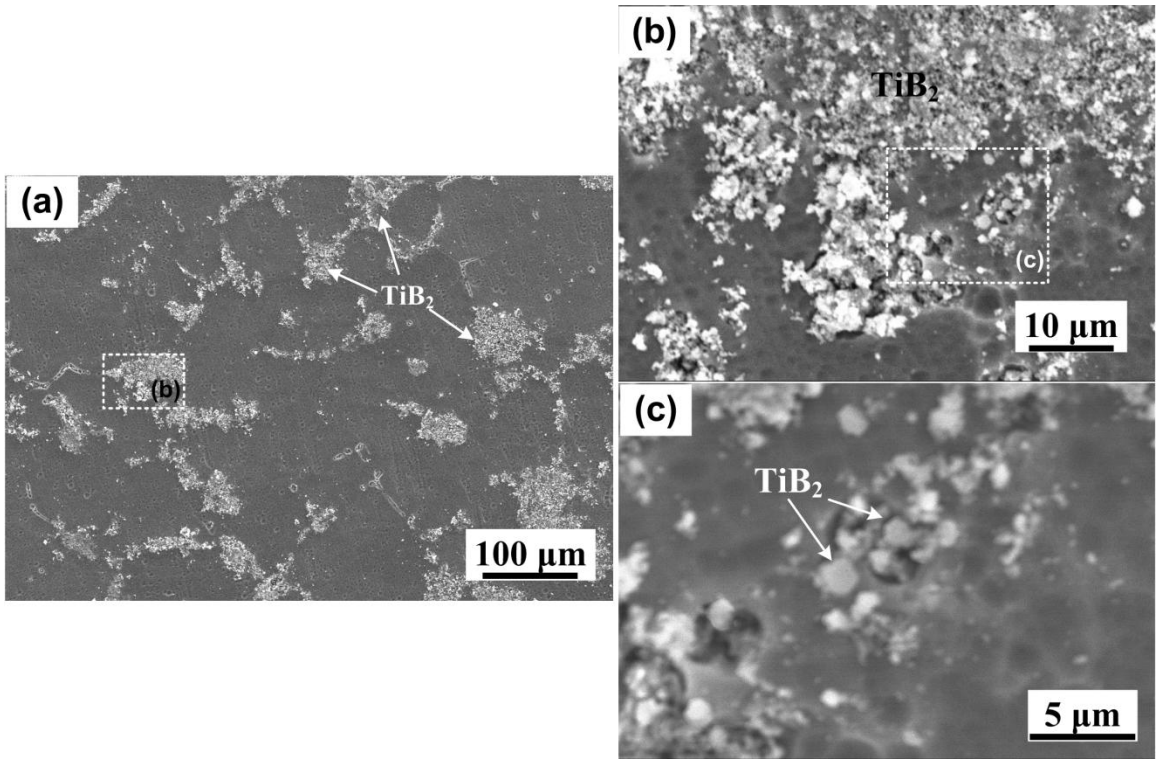

Figure 4.2 (a) Typical microstructure of the S900-10 sample, (b) higher magnification of the area marked in image (a), and (c) higher magnification of the area marked in image (b).

3) Examination of the Purity of Extracted TiB_2 Particles

Phase composition of the extracted particles from the S900-10 sample was examined by XRD. The result is shown in Figure 4.3. Only TiB_2 phase was detected, indicating that a completed extraction process was obtained, in which the Al matrix and some other possibly existed phases had dissolved into the HCl solution completely. Thereby, no other phases influenced the calculation of the yield of TiB_2 particulates and the measurement of their size distribution.

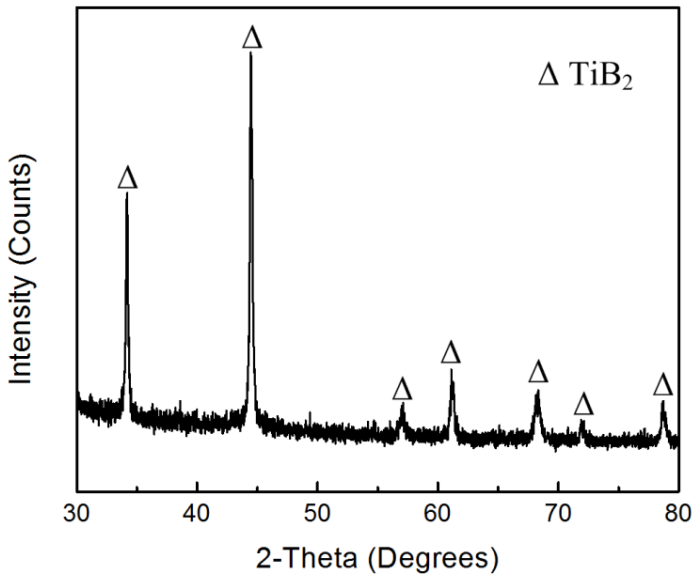

Figure 4.3 XRD pattern of the extracted TiB_2 particles from the S900-10 sample.

4) Yield of TiB_2 Particulates in S900-10 Sample

The yield of TiB_2 particulates in each extracting experiment is given in Table 4.1. Based on the calculation results, the average actual weight percentage of TiB_2 in the sample was about 4.475 %. Accordingly, the yield of TiB_2 particulates could reach 89.50 %.

Table 4.1 *Calculation of the yield of TiB_2 particulates in the S900-10 sample.*

Group	Quantity of the ingot for extracting experiment (g)	Quantity of extracted TiB_2 particles (g)	Actual weight percent (wt. %)	Yield of TiB_2 (%)
1	8.193	0.371	4.52	90.40
2	8.697	0.385	4.43	88.60
Average	-	-	4.475	89.50

5) Size Distribution of TiB_2 Particulates in S900-10 Sample

The size distribution of the TiB_2 particles extracted from the S900-10 sample is shown in Figure 4.4. The detailed statistical result is also included in Figure 4.4. It is clear that most TiB_2 particulates in the S900-10 sample were less than 1 μm in size, in which about 79.1 % of the TiB_2 particles ranged in size from 400 to 800 nm. Also, a very small amount of TiB_2 ranged in size from 1 to 2 μm. The above statistical result about the size distribution of TiB_2 is in good agreement with the SEM analysis (Figure 4.2). The size distribution of TiB_2 particulates in the S900-10 sample followed a normal distribution as well.

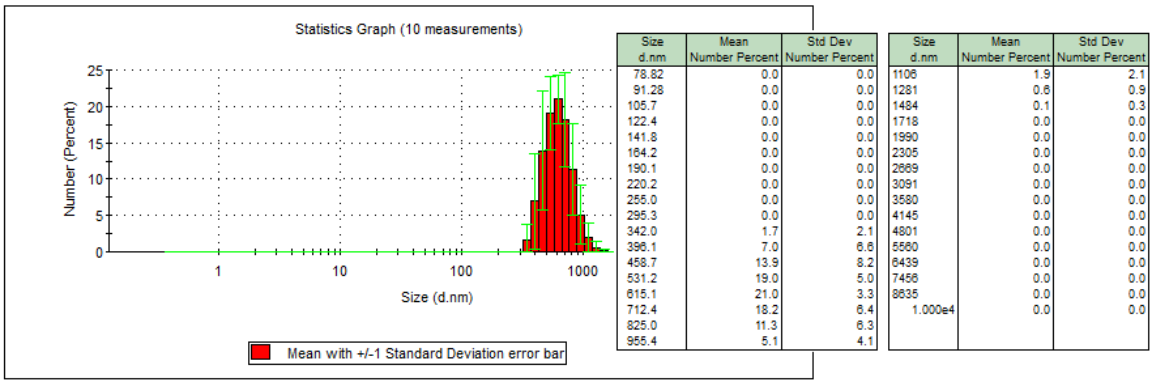

Size d.nm	Mean Number Percent	Std Dev Number Percent
78.82	0.0	0.0
91.28	0.0	0.0
105.7	0.0	0.0
122.4	0.0	0.0
141.8	0.0	0.0
164.2	0.0	0.0
190.1	0.0	0.0
220.2	0.0	0.0
255.0	0.0	0.0
295.3	0.0	0.0
342.0	1.7	2.1
396.1	7.0	6.6
458.7	13.9	8.2
531.2	19.0	5.0
615.1	21.0	3.3
712.4	18.2	6.4
825.0	11.3	6.3
955.4	5.1	4.1

Size d.nm	Mean Number Percent	Std Dev Number Percent
1106	1.9	2.1
1281	0.6	0.9
1484	0.1	0.3
1718	0.0	0.0
1990	0.0	0.0
2305	0.0	0.0
2669	0.0	0.0
3091	0.0	0.0
3580	0.0	0.0
4145	0.0	0.0
4801	0.0	0.0
5560	0.0	0.0
6439	0.0	0.0
7456	0.0	0.0
8635	0.0	0.0
1.000e4	0.0	0.0

Figure 4.4 Size distribution of TiB_2 particulates in the S900-10 sample.

4.1.1.2 S900-30 Sample

1) Phases Analysis of Products

Figure 4.5 shows the XRD patterns of the slag and sample (S900-30) produced at 900 °C with a 30-min reaction time. Similar to the products produced at 900 °C with a 10-min reaction time, $KAlF_4$ and K_3AlF_6 were the two main phases in the slag, and TiB_2 was the only newly formed phase in the sample.

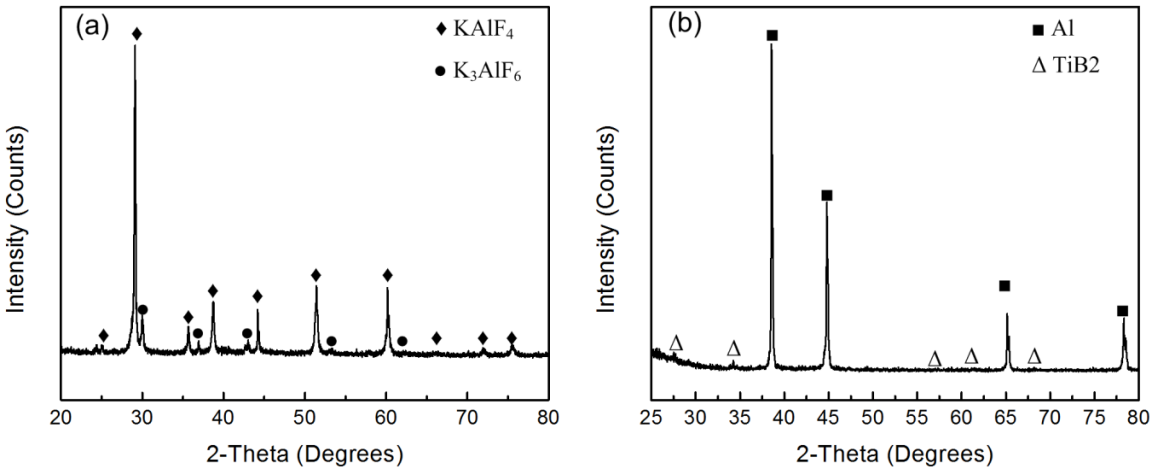

Figure 4.5 XRD patterns of the slag (a), and S900-30 sample (b) produced at 900 °C with a 30-min reaction time.

2) Microstructure Analysis of S900-30 Sample

The typical microstructure of the S900-30 sample is presented in Figure 4.6. Overall, it had similar microstructural features with the S900-10 sample. Only TiB_2 particulates were in situ formed, which existed in the Al matrix as clusters located at the grain boundaries (Figure 4.6a). Most TiB_2 particulates were smaller than 1 μm in size (Figure 4.5b); whereas a very small amount of TiB_2 particulates were greater than 1 μm, as shown in Figure 4.6c.

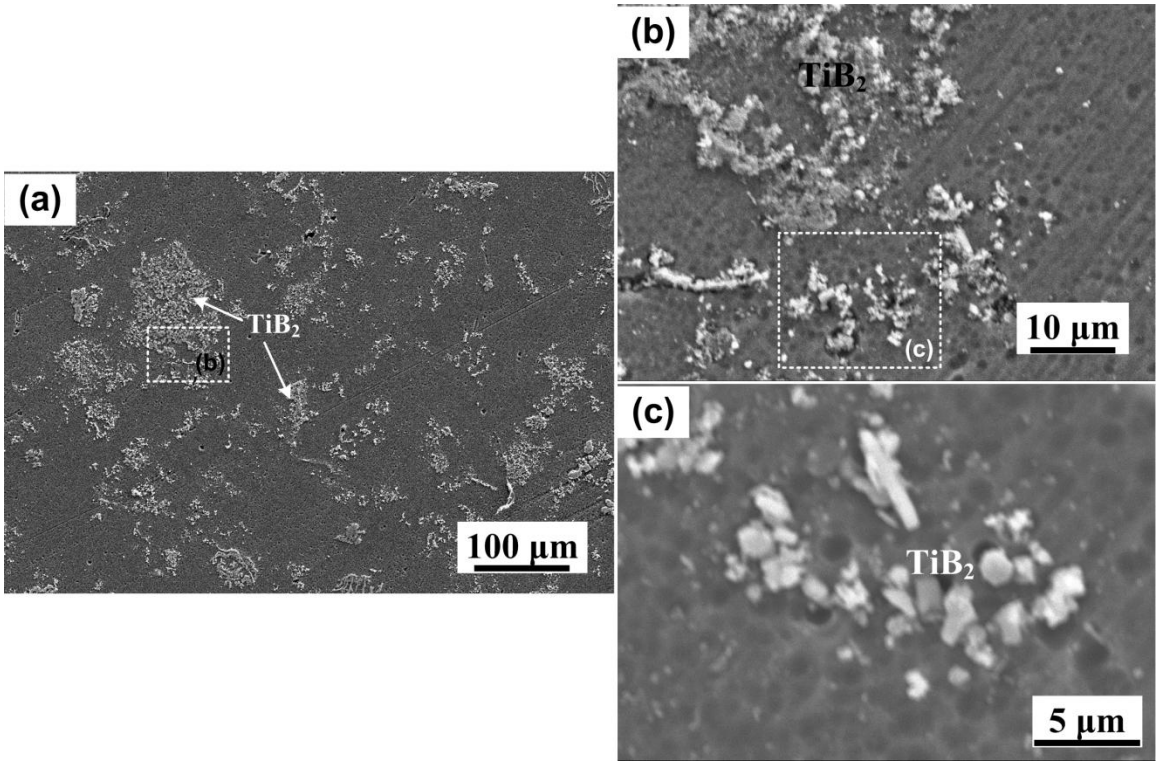

Figure 4.6 (a) Typical microstructure of the S900-10 sample, (b) higher magnification of the area marked in image (a), and (c) higher magnification of the area marked in image (b).

3) XRD Analysis of Extracted Particles

Figure 4.7 shows the phase composition of the extracted particles from the S900-30 sample. TiB_2 was the only phase in the particles, indicating that no interference from

other phases influenced the calculation of the yield of TiB_2 and the measurement of size distribution of TiB_2.

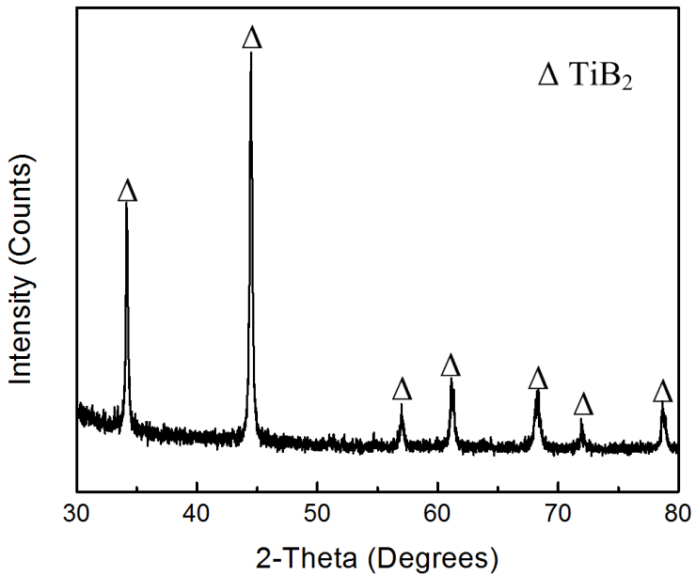

Figure 4.7 XRD pattern of the extracted TiB_2 particles from the S900-30 sample.

4) Yield of TiB_2 Particulates

Table 4.2shows the yield of TiB_2 particulates in the S900-30 sample. The actual weight percentage of TiB_2 particulates in the Al matrix was about 4.515 %, and the yield of which could reach about 90.30%.

Table 4.2 *Calculation of the yield of TiB_2 particulates in the S900-30 sample.*

Group	Quantity of the ingot for extracting experiment (g)	Quantity of extracted TiB_2 particles (g)	Actual weight percent of TiB_2 (wt. %)	Yield of TiB_2 (%)
1	7.667	0.344	4.49	89.80
2	8.012	0.364	4.54	90.80
Average	-	-	4.515	90.30

5) Size Distribution of TiB_2 Particulates

Figure 4.8 shows the size distributions of TiB_2 particulates synthesized in the S900-30 sample. Overall, most TiB_2 particulates were smaller than 1 μm in size, in which about 83.1 % of the TiB_2 ranged in size from 400 to 800 nm; a rather small amount of TiB_2 particles had the size in the range of 1-2 μm, which is in good agreement with the SEM analysis (Figure 4.6). The size distribution of TiB_2 particulates followed a normal distribution as well.

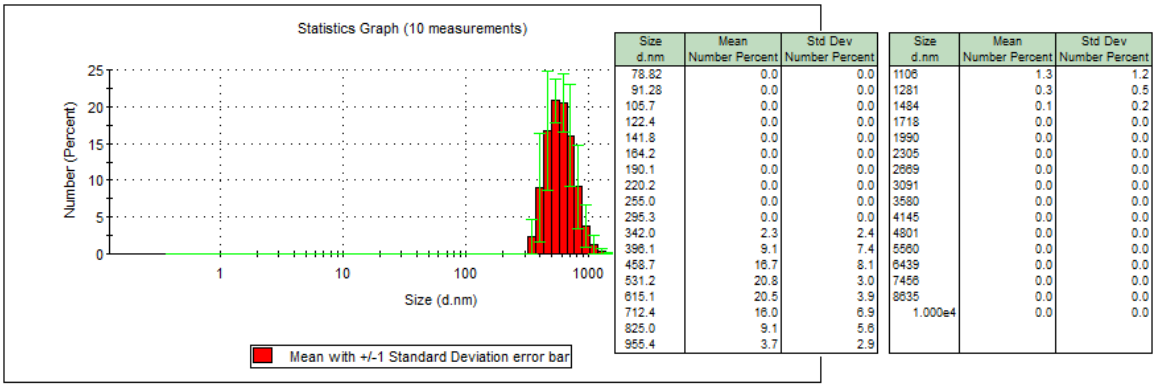

Size d.nm	Mean Number Percent	Std Dev Number Percent
78.82	0.0	0.0
91.28	0.0	0.0
105.7	0.0	0.0
122.4	0.0	0.0
141.8	0.0	0.0
164.2	0.0	0.0
190.1	0.0	0.0
220.2	0.0	0.0
255.0	0.0	0.0
295.3	0.0	0.0
342.0	2.3	2.4
396.1	9.1	7.4
458.7	16.7	8.1
531.2	20.8	3.0
615.1	20.5	3.9
712.4	16.0	6.9
825.0	9.1	5.6
955.4	3.7	2.9

Size d.nm	Mean Number Percent	Std Dev Number Percent
1106	1.3	1.2
1281	0.3	0.5
1484	0.1	0.2
1718	0.0	0.0
1990	0.0	0.0
2305	0.0	0.0
2669	0.0	0.0
3091	0.0	0.0
3580	0.0	0.0
4145	0.0	0.0
4801	0.0	0.0
5560	0.0	0.0
6439	0.0	0.0
7456	0.0	0.0
8635	0.0	0.0
1.000e4	0.0	0.0

Figure 4.8 Size distributions of TiB_2 particulates in the S900-30 sample.

4.1.2 Results of the Mixed-salts Reaction at 800 °C

4.1.2.1 S800-10 Sample

1) Phase Analysis of the Products

Figure 4.9 presents the phase compositions of the slag and S800-10 sample, both of which were obtained in the mixed-salts reaction at 800 °C with a 10-min reaction time. $KAlF_4$ and K_3AlF_6 were the two main phases in the slag, indicating that Ti and B elements were transferred from the molten mixed salts to molten Al, as shown in Figure

4.9a. TiB_2 was the only newly formed phase in the Al matrix, which was shown in Figure 4.9b. It is clear that the mixed-salts reaction of K_2TiF_6-KBF_4-Al took place according to the chemical reaction shown in Eq. 2.8 at 800 °C.

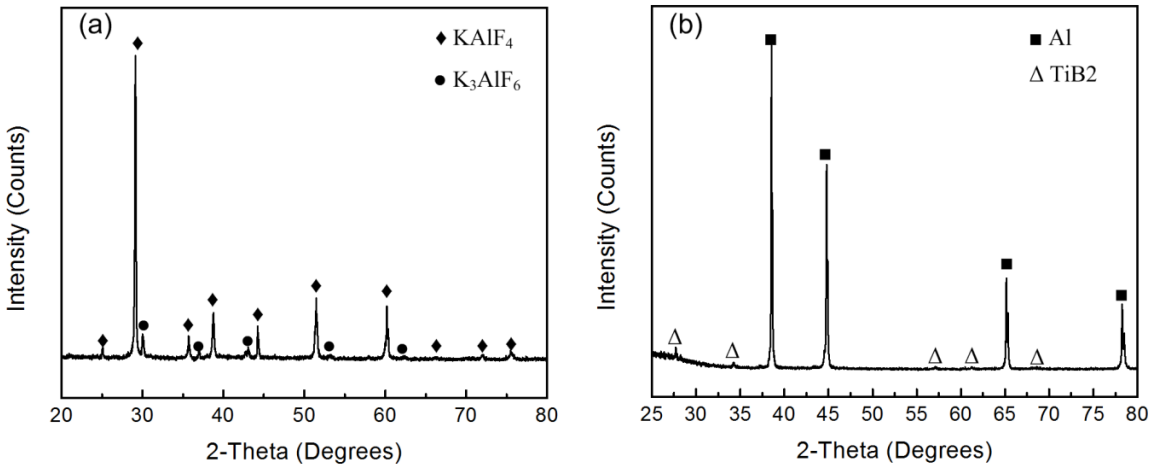

Figure 4.9 XRD patterns of the slag (a), and S800-10 sample (b) produced at 800 °C with a 10-min reaction time.

2) SEM Analysis of S800-10 Sample

Figure 4.10 shows the typical microstructure of the S800-10 sample which was fabricated at 800 °C with a 10-min reaction time. Two types of reinforcements with different morphology were found in the Al matrix. One was chain-like reinforcement, and the other was particulates which aggregated together, as shown in Figure 4.10a. After the EDS examination, the main phase of the chain-like reinforcement was Al_3Ti. However, a very small amount of TiB_2 phase also might exist in this reinforcement, as shown in Figure 4.10b. The in situ formed particulates were TiB_2 which were identified by EDS, and these particulates had different sizes, some of which were larger than 1 μm, as shown in Figure 4.10c.

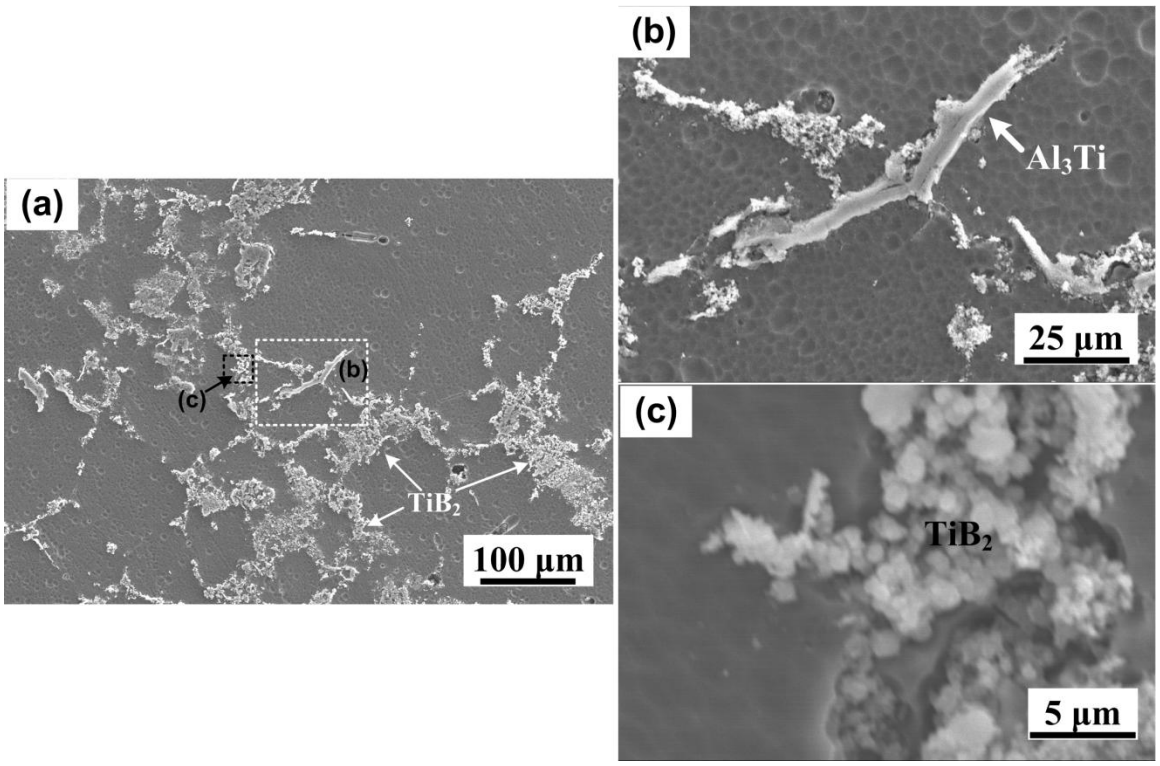

Figure 4.10 (a) Typical microstructure of the S800-10 sample, (b) higher magnification of the area marked in image (a), and (c) higher magnification of the area marked in image (a).

3) XRD Analysis of Extracted TiB_2 particles

According to the XRD result (Figure 4.11), only TiB_2 phase was found in the extracted particles from the S800-10 sample, indicating that no other phase influenced both the calculation of the yields of TiB_2 and the measurement of the size distribution of TiB_2 particulates.

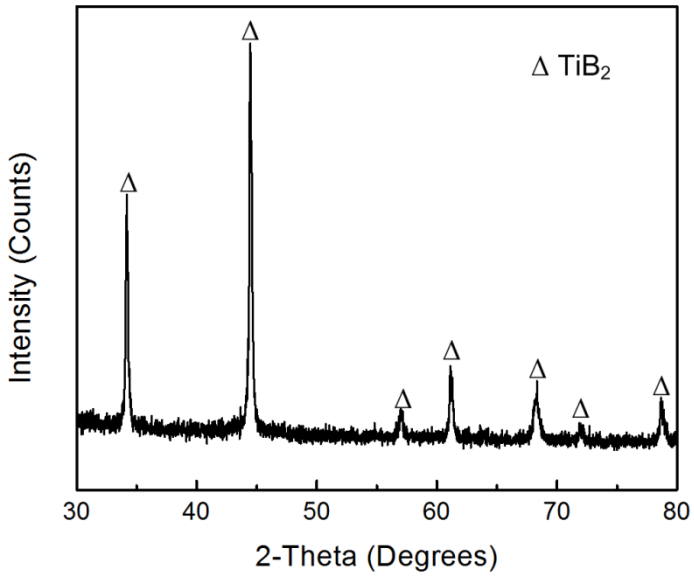

Figure 4.11 XRD pattern of the extracted TiB_2 particles from the S800-10 sample.

4) Yield of TiB_2 Particulates in S800-10 Sample

After calculation (as shown in Table 4.3), the actual weight percentage of TiB_2 in the mixed-salts reaction at 800 °C with a 10-min reaction time could reach around 3.515 wt. %. Accordingly, the yield of TiB_2 was about 70.30 %.

Table 4.3 *Calculation of the yield of TiB_2 particulates in the S800-10 sample.*

Group	Quantity of the ingot for extracting experiment (g)	Quantity of extracted TiB_2 particles (g)	Actual weight percent of TiB_2 (wt. %)	Yield of TiB_2 (%)
1	7.601	0.263	3.46	69.20
2	7.669	0.274	3.57	71.40
Average	-	-	3.515	70.30

5) Size Distribution of TiB_2 Particulates in S800-10 Sample

Figure 4.12 shows the size distribution of TiB_2 particulates synthesized in the S800-10 sample. It is obvious that most of TiB_2 particulates were less than 1μm in size, in which about 95 % of the TiB_2 had the size smaller than 300 nm according to the statistic result. In addition, a rather small amount of in situ formed TiB_2 particulates larger than 1 μm were detected by Zetasizer Nano ZS device. The existence of larger-sized TiB_2 particulates (larger than 1 μm) in the Al matrix was also found by SEM test (as shown in Figure. 4.10c). Generally, the size distribution of TiB_2 particulates in the S800-10 sample followed a normal distribution as well.

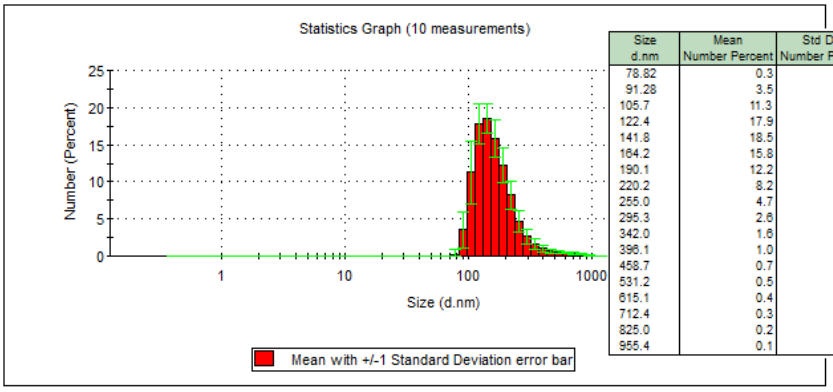

Size d.nm	Mean Number Percent	Std Dev Number Percent	Size d.nm	Mean Number Percent	Std Dev Number Percent
78.82	0.3	0.6	1106	0.1	0.0
91.28	3.5	2.5	1281	0.0	0.0
105.7	11.3	4.2	1484	0.0	0.0
122.4	17.9	2.7	1718	0.0	0.0
141.8	18.5	1.9	1990	0.0	0.0
164.2	15.8	2.5	2305	0.0	0.0
190.1	12.2	2.4	2669	0.0	0.0
220.2	8.2	1.9	3091	0.0	0.0
255.0	4.7	1.4	3580	0.0	0.0
295.3	2.6	1.0	4145	0.0	0.0
342.0	1.6	0.7	4801	0.0	0.0
396.1	1.0	0.4	5560	0.0	0.0
458.7	0.7	0.3	6439	0.0	0.0
531.2	0.5	0.2	7456	0.0	0.0
615.1	0.4	0.2	8635	0.0	0.0
712.4	0.3	0.1	1.000e4	0.0	0.0
825.0	0.2	0.1			
955.4	0.1	0.0			

Figure 4.12 Size distribution of TiB_2 particulates in the S800-10 sample.

4.1.2.2 S800-30 Sample

1) Phases Analysis of Products

Figure 4.13 presents the XRD results of the slag and S800-30 sample produced in the mixed-salts reaction at 800 °C with a 30-min reaction time. $KAlF_4$ and K_3AlF_6 were

the main phases in the slag, as shown in Figure 4.13a. TiB_2 was detected as the only newly formed phase in the sample, as shown in Figure 4.13b.

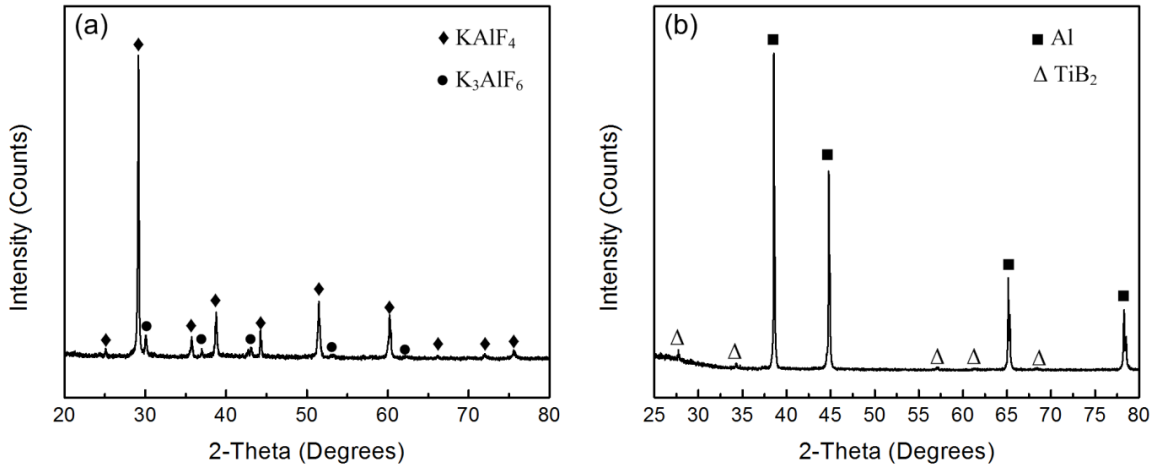

Figure 4.13 XRD patterns of the slag (a), and S800-30 sample (b) produced at 800 °C with a 30-min reaction time.

2) Microstructure Analysis of S800-30 Sample

The microstructure of the S800-30 sample is given in Figure 4.14. Two main types of reinforcements were found in the Al matrix. One was TiB_2 particulates which formed clusters at the grain boundaries, as shown in Figure 4.14a. The other one was the chain-like reinforcements with a large size, in which Al and Ti elements were identified by EDS, indicating that the main phase contained in the chain-like reinforcements was Al_3Ti, as shown in Figure 4.14b. Due to its low content, Al_3Ti phase was not detected in the XRD analysis. Furthermore, some large TiB_2 particulates with the size greater than 1 μm were also found in this sample, as shown in Figure 4.14c. It also should be mentioned that some AlB_2 phase might exist in the matrix, but it is hard to be examined out by SEM due to its low content and blocky morphology.

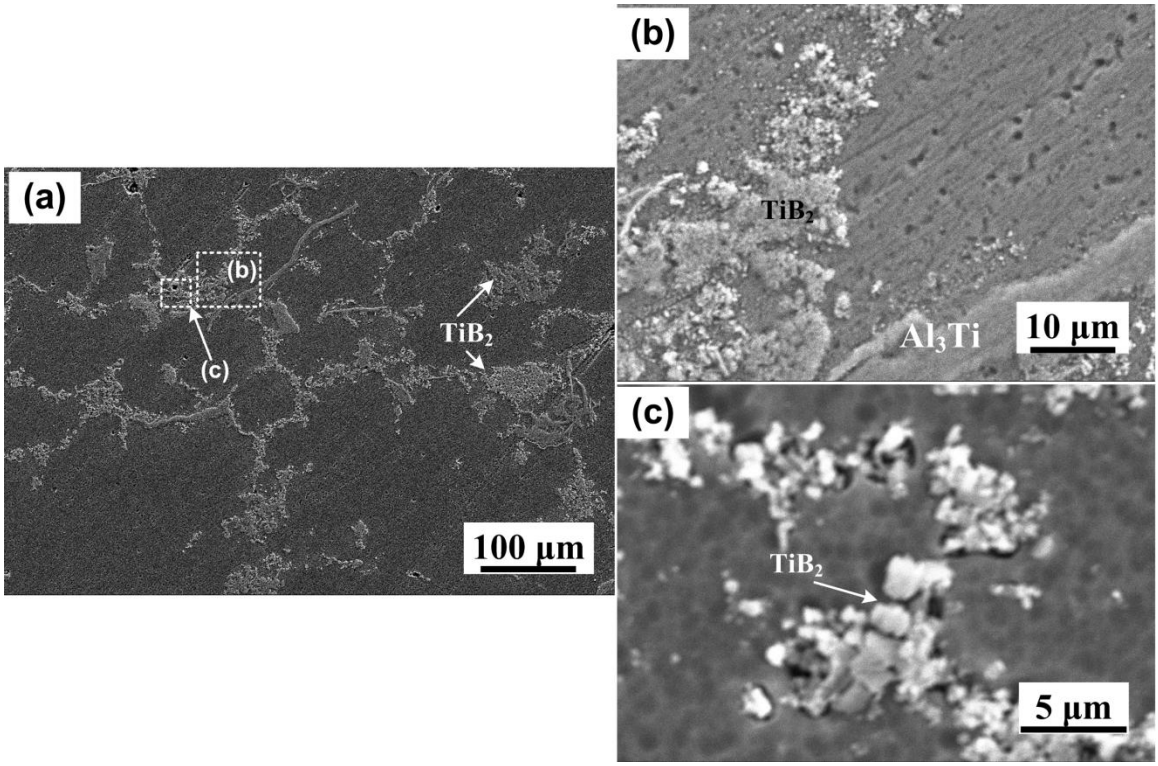

Figure 4.14 (a) Typical microstructure of the S800-30 sample, (b) higher magnification of the area marked in image (a), and (c) higher magnification of the area marked in image (a).

3) XRD Analysis of Extracted TiB_2 Particles from S800-30 Sample

Figure 4.14 shows the XRD pattern of the extracted TiB_2 particles from the S800-30 sample. Only TiB_2 phase was found in the particles, which indicated that the extraction experiment was conducted completely.

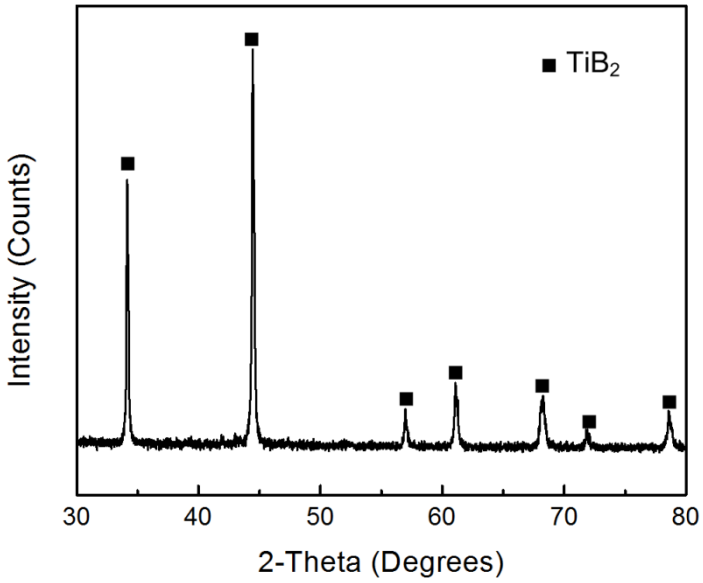

Figure 4.15 XRD pattern of the extracted TiB_2 particles from the S800-30 sample.

4) Yield of TiB_2 Particulates in S800-30 Sample

The actual weight percentage of TiB_2 obtained in the S800-30 sample was about 3.80 wt. %, and its yield reached 76 %. Compared with S800-10 sample, it is found that more TiB_2 was formed as the reaction time was increased.

Table 4.4 *Calculation of the yield of TiB_2 particulates in the S800-30 sample.*

Group	Quantity of the ingot for extracting experiment (g)	Quantity of extracted TiB_2 particles (g)	Actual weight percent of TiB_2 (wt. %)	Yield of TiB_2 (%)
1	8.004	0.309	3.86	77.20
2	7.735	0.289	3.74	74.80
Average	-	-	3.80	76.00

5) Size Distribution of TiB_2 Particulates in S800-30 Sample

Figure 4.16 shows the size distribution of TiB_2 particulates in the S800-30 sample. Overall, most TiB_2 particulates in S800-30 sample were smaller than 1 μm, in which about 95 % of the TiB_2 had the size less than 300nm. Some TiB_2 particulates larger than 1 μm were also detected. An interesting finding observed in the statistic result is that the ratio of smaller-sized TiB_2 was increased, indicating that the newly formed TiB_2 phase had a smaller size. It is clear that the size distribution of TiB_2 particulates in S800-30 sample followed a normal distribution as well.

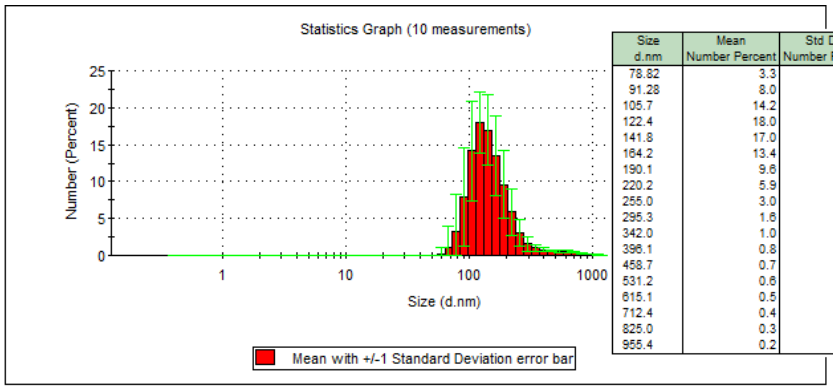

Size d.nm	Mean Number Percent	Std Dev Number Percent
78.82	3.3	5.0
91.28	8.0	6.7
105.7	14.2	6.7
122.4	18.0	4.1
141.8	17.0	4.8
164.2	13.4	5.4
190.1	9.6	4.6
220.2	5.9	3.1
255.0	3.0	1.8
295.3	1.6	1.0
342.0	1.0	0.5
396.1	0.8	0.2
458.7	0.7	0.1
531.2	0.6	0.2
615.1	0.5	0.2
712.4	0.4	0.1
825.0	0.3	0.1
955.4	0.2	0.0

Size d.nm	Mean Number Percent	Std Dev Number Percent
1106	0.1	0.0
1281	0.0	0.0
1484	0.0	0.0
1718	0.0	0.0
1990	0.0	0.0
2305	0.0	0.0
2669	0.0	0.0
3091	0.0	0.0
3580	0.0	0.0
4145	0.0	0.0
4801	0.0	0.0
5560	0.0	0.0
6439	0.0	0.0
7456	0.0	0.0
8635	0.0	0.0
1.000e4	0.0	0.0

Figure 4.16 Size distribution of TiB_2 particulates in the S800-30 sample.

4.1.3 Results of the Mixed-salts Reaction at 700 °C

4.1.3.1 S700-10 Sample

1) Phases Analysis of Products

Figure 4.17 shows the XRD patterns of the slag and S700-10 obtained in the mixed-salts reaction at 700 °C with a 10-min reaction time. $KAlF_4$ and K_3AlF_6 detected by XRD were the main phases in the slag. No any phase containing Ti or B was found in

the slag, suggesting that Ti and B elements were both transferred to molten Al from salts. Some rather weak diffraction peaks of TiB_2 phase were found in the S700-10 sample, indicating that the mixed-salts reaction proceeded according to the chemical formula shown in Eq. 2.8 at the low temperature of 700 °C.

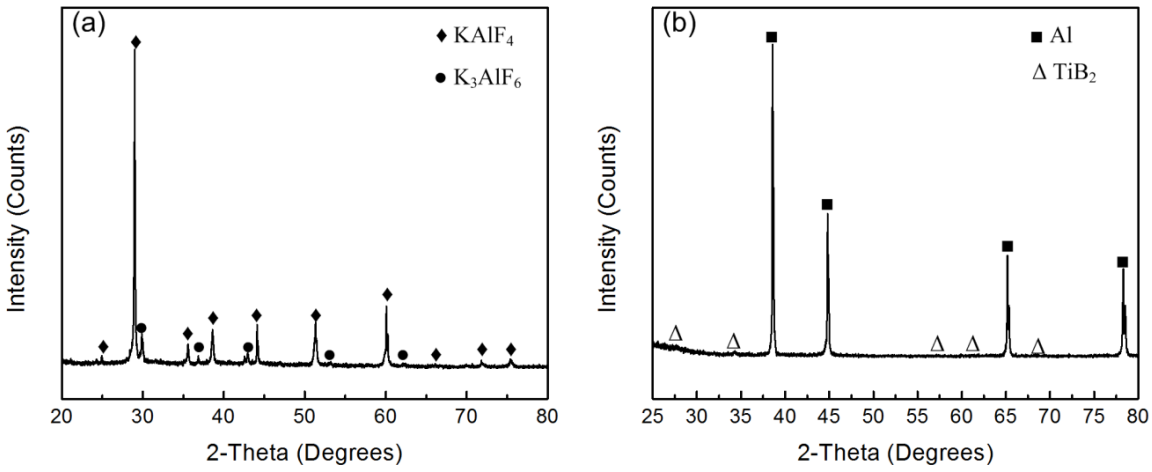

Figure 4.17 XRD patterns of the slag (a), and S700-10 sample (b) produced in the mixed-salts reaction at 700 °C with a 10-min reaction time.

2) Microstructure Analysis of S700-10 Sample

Figure 4.18 shows the typical microstructure of the S700-10 sample. Three types of reinforcements existed in the Al matrix. Some blocky particles ranged in size from 1 to 3μm were detected as Al_3Ti by EDS. Some rather small-sized TiB_2 particulates were also found in the matrix, most of which existed along the chain-like reinforcement. After examined by EDS, the main phase of chain-like reinforcement was identified as Al_3Ti, and also some separately tiny TiB_2 particles were located in Al_3Ti, as shown in Figure 4.18b. In addition, a little amount of AlB_2 phase might exist in the Al matrix, but it is hard to examine them out in the present research due to the limitation of device.

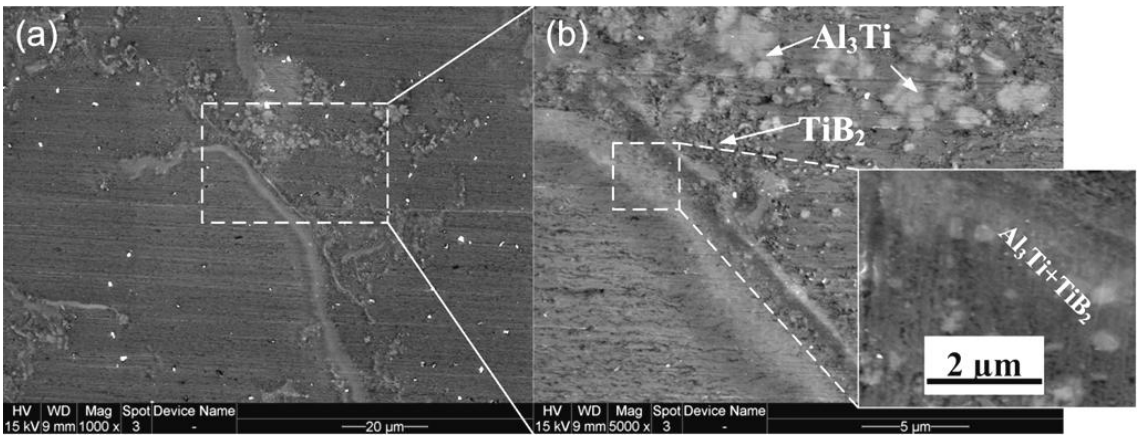

Figure 4.18 (a) Typical microstructure of the S700-10 sample, and (b) higher magnification of the area marked in image (a).

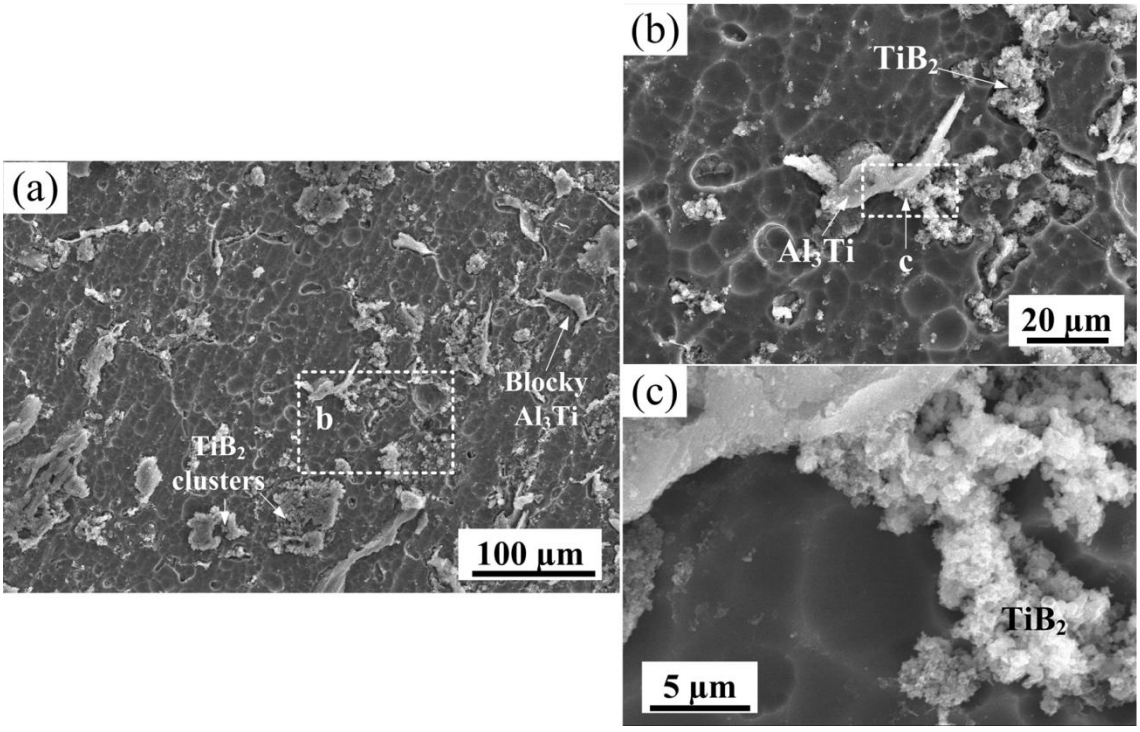

Figure 4.19 SEM images of the deep-etched S700-10 sample.

In order to clarify the morphologies of the reinforcements in the Al matrix, a deep-etched sample was observed by SEM, the results are shown in Figure. 4.19. Actually, the chain-like Al_3Ti was flakey in morphology, with a thickness of a few

micrometers. Also, some in situ formed TiB_2 particles existed in the Al matrix in the form of cluster, and the size of these TiB_2 particles was less than 1μm obviously. Since some TiB_2 particulates aggregated together, it is hard to make a clear observation.

3) XRD Analysis of Extracted TiB_2 Particles from S700-10 Sample

Based on the XRD result as shown in Figure 4.20, only TiB_2 phase was detected in the extracted particles, indicating that some other phases (such as Al_3Ti) had completely dissolved into the HCl solution.

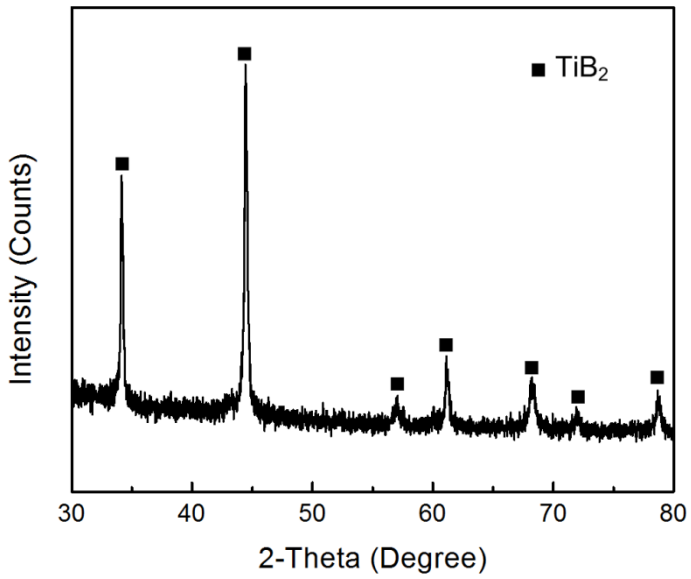

Figure 4.20 XRD pattern of the extracted TiB_2 particles from the S700-10 sample.

4) Yield of TiB_2 Particulates in S700-10 Sample

The yield of TiB_2 in the S700-10 sample is calculated in the Table 4.5. The measured actual weight percentage of TiB_2 synthesized in the S700-10 sample was rather low, the value of which was about 1.405 wt. %. And the corresponding yield of TiB_2 was

28.10 %. This result clearly showed that the synthesis of TiB_2 in the mixed-salts reaction was hindered significantly at 700 °C.

Table 4.5 *Calculation of the yield of TiB_2 particulates in the S700-10 sample.*

Group	Quantity of the ingot for extracting experiment (g)	Quantity of extracted TiB_2 particles (g)	Actual weight percent of TiB_2 (wt. %)	Yield of TiB_2 (%)
1	6.989	0.098	1.40	28.00
2	7.086	0.10	1.41	28.20
Average	-	-	1.405	28.10

5) Size Distribution of TiB_2 Particulates in S700-10 Sample

Overall, in situ formed TiB_2 particulates in the S700-10 sample were smaller than 700 nm, in which approximate 95 % of the TiB_2 particles were smaller than 300 nm, and size distribution of TiB_2 particulates followed a normal distribution as well, as shown in Figure 4.21. The result clearly shows that a lower reaction temperature can decrease the size of TiB_2 remarkably. The yield of TiB_2, however, is rather low at a lower temperature.

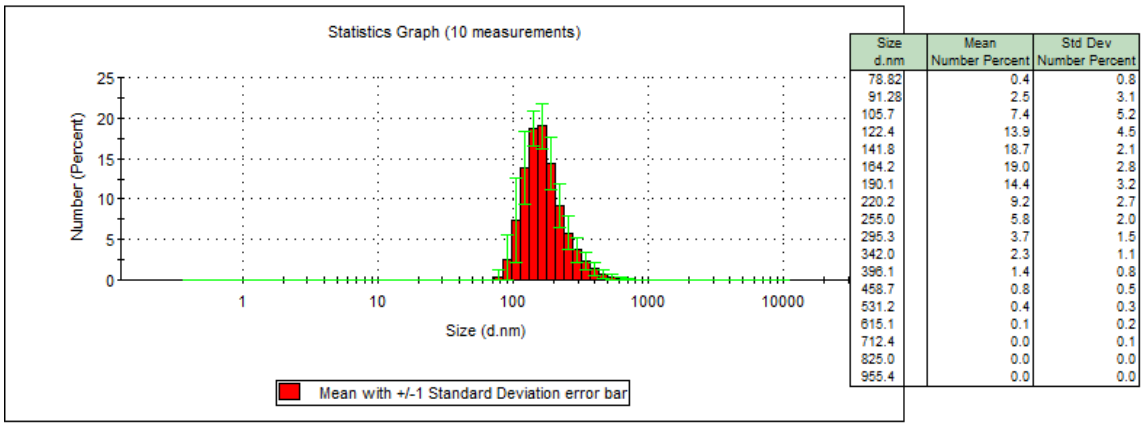

Figure 4.21 Size distribution of TiB_2 particulates in the S700-10 sample.

4.1.3.2 S700-30 Sample

1) Phases Analysis of Products

Figure 4.22 shows the XRD patterns of the slag and S700-30 sample obtained in the mixed-salts reaction at 700 °C with a 30-min reaction time. As shown in Figure 4.22a, the slag was consisted of $KAlF_4$ and K_3AlF_6 phases. Weak TiB_2 peaks were also found in the sample, showing that the content of TiB_2 phase was still low (Figure. 4.22b) in the Al matrix by a 30-min reaction.

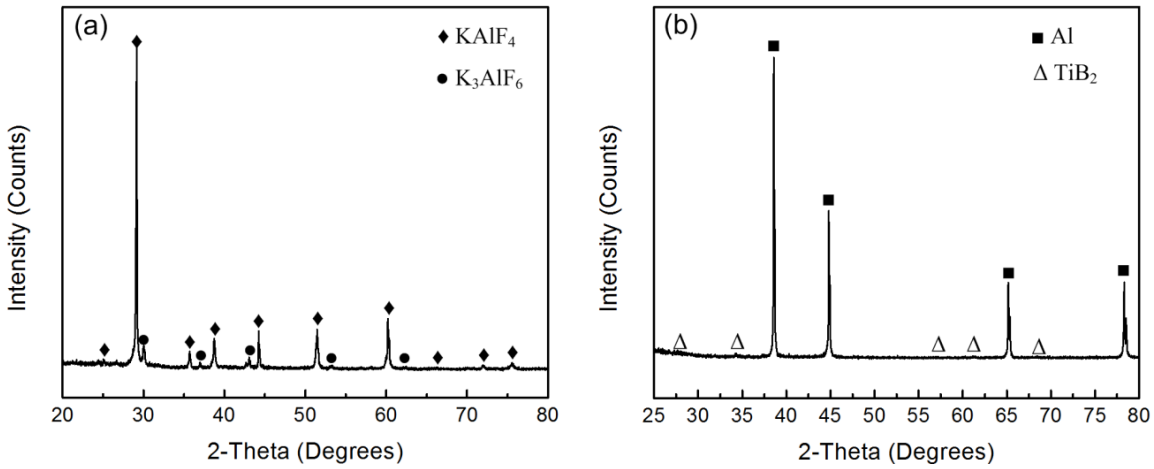

Figure 4.22 XRD patterns of the slag (a), and S700-30 sample (b) produced in the mixed-salts reaction at 700 °C with a 30-min reaction time.

2) Microstructure Analysis of S700-30 Sample

Figure 4.23 shows the microstructure of the S700-30 sample. Long chain-like reinforcements and cluster-like reinforcements were both found in the Al matrix, as shown in Figure 4.23a. It is found that the chain-like reinforcement was composed of by Al_3Ti and some small-sized TiB_2 particulates which were located in the Al_3Ti phase, as shown in Figure 4.23b. The cluster-like reinforcement was consisted of some large-sized

blocky Al_3Ti particles and some nanometer-sized TiB_2 particles, as shown in Figure 4.23c. One more thing should be mentioned is that the size of long chain-like reinforcement in S700-30 sampler was smaller than that in the S700-10 sample, which indicated that part of it might dissolve or react as the reaction time was increased. AlB_2 phase also might exist in the sample, which was hard to examine out clearly in this research.

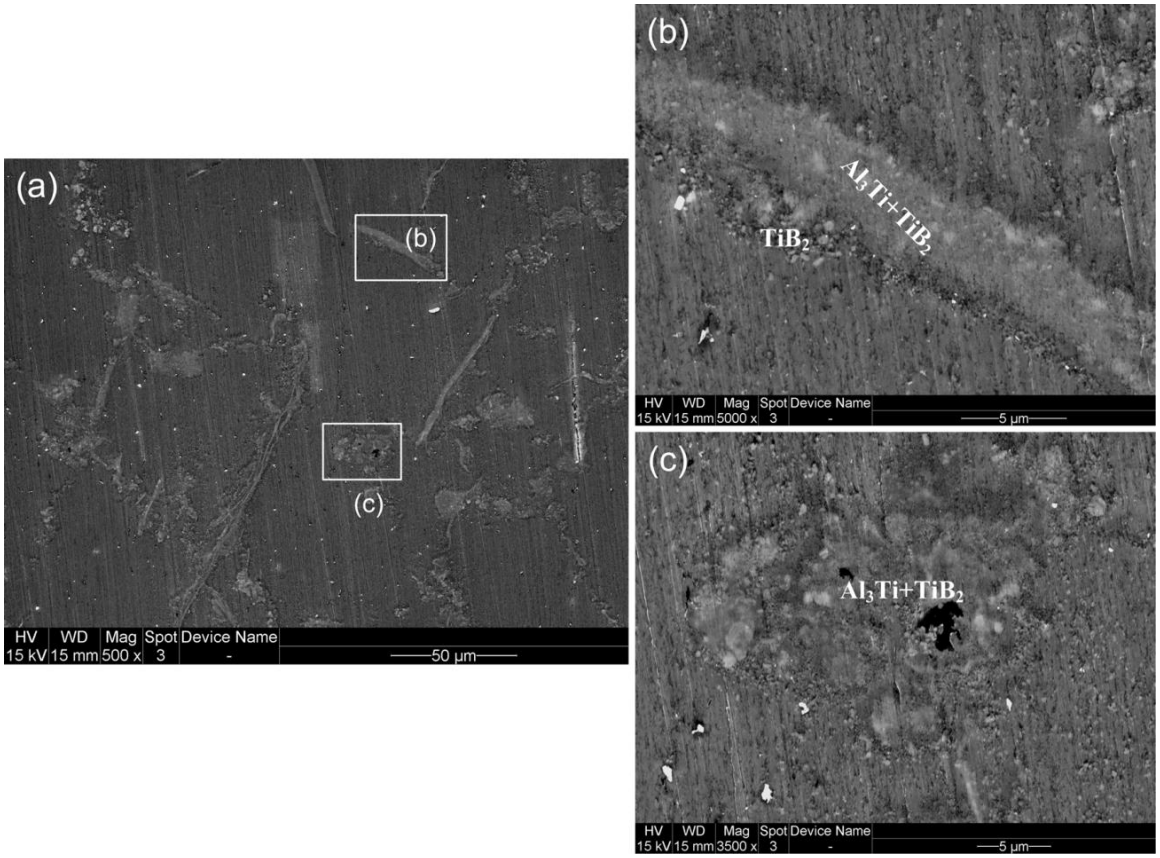

Figure 4.23 (a) Typical microstructure of the S700-30 sample, and (b), (c) higher magnification of the areas marked in image (a).

3) XRD Analysis of Extracted TiB_2 Particles from S700-30 Sample

As shown in Figure 4.24, only TiB_2 was detected by XRD in the extracted particles, which meant a completed extraction process was carried out. Thereby, the measurement results of yield and the size distribution of TiB_2 particulates were believable, since other phases such as Al_3Ti and AlB_2 were dissolved into HCl solution completely.

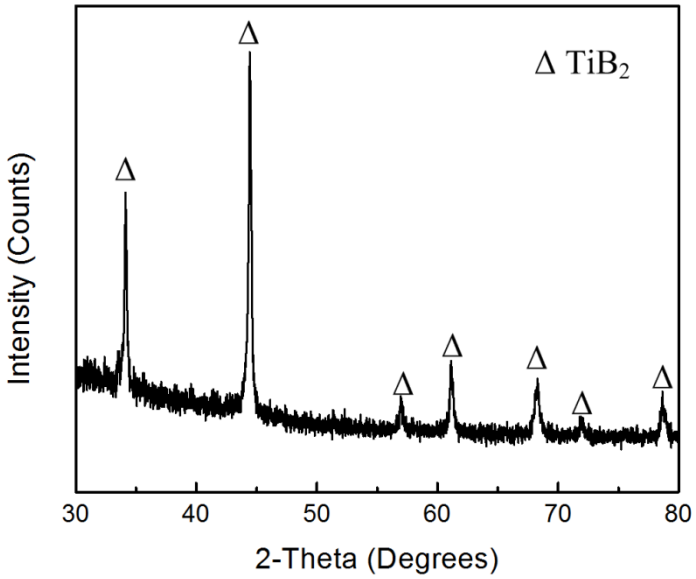

Figure 4.24 XRD pattern of the extracted TiB_2 particles from the S700-30 sample.

4) Yield of TiB_2 Particulates in S700-30 Sample

The actual weight percentage of TiB_2 in the S700-30 sample was about 1.775 wt. %, and the related yield of TiB_2 was about 35.50 %, as shown in Table 4.6. The result shows that the yield of TiB_2 phase in the S700-30 sample was still low, but a certain amount of TiB_2 phase was formed as the reaction time was prolonged from 10 to 30 min.

Table 4.6 *Calculation of the yield of TiB_2 particulates in the S700-30 sample.*

Group	Quantity of the ingot for extracting experiment (g)	Quantity of extracted TiB_2 particles (g)	Actual weight percent of TiB_2 (wt. %)	Yield of TiB_2 (%)
1	7.657	0.135	1.76	35.20
2	7.698	0.138	1.79	35.80
Average	-	-	1.775	35.50

5) Size Distribution of TiB_2 Particulates in S700-30 Sample

According to the measurement result shown in Figure 4.25, the size of TiB_2 particulates synthesized in the S700-30 sample was smaller than 1 μm. More than 95% of the TiB_2 had the size less than 300 nm. Furthermore, the content of TiB_2 with a smaller size was increased, and the ratio of TiB_2 smaller than 100 nm was about 30 %, indicating that a certain amount of TiB_2 particulates with a smaller size were formed as the reaction time was prolonged from 10 to 30 min.

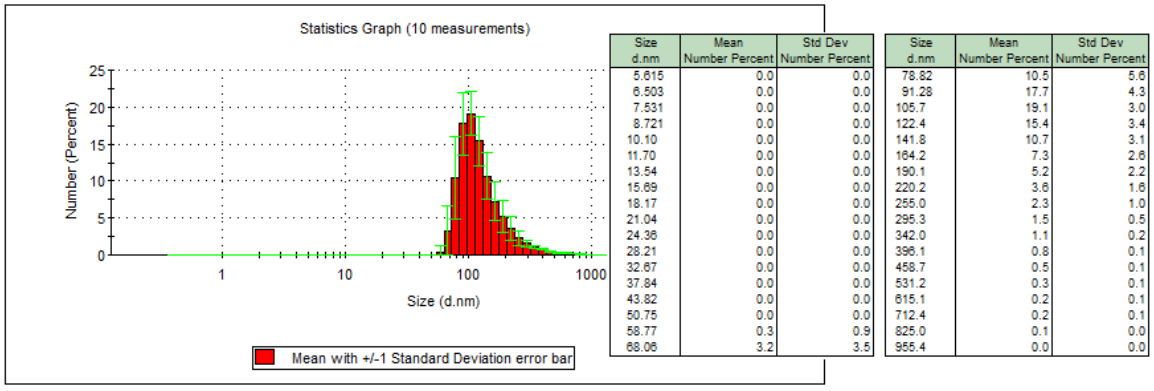

Size d.nm	Mean Number Percent	Std Dev Number Percent
5.615	0.0	0.0
6.503	0.0	0.0
7.531	0.0	0.0
8.721	0.0	0.0
10.10	0.0	0.0
11.70	0.0	0.0
13.54	0.0	0.0
15.69	0.0	0.0
18.17	0.0	0.0
21.04	0.0	0.0
24.36	0.0	0.0
28.21	0.0	0.0
32.67	0.0	0.0
37.84	0.0	0.0
43.82	0.0	0.0
50.75	0.0	0.0
58.77	0.3	0.9
68.06	3.2	3.5

Size d.nm	Mean Number Percent	Std Dev Number Percent
78.82	10.5	5.6
91.28	17.7	4.3
105.7	19.1	3.0
122.4	15.4	3.4
141.8	10.7	3.1
164.2	7.3	2.6
190.1	5.2	2.2
220.2	3.6	1.6
255.0	2.3	1.0
295.3	1.5	0.5
342.0	1.1	0.2
396.1	0.8	0.1
458.7	0.5	0.1
531.2	0.3	0.1
615.1	0.2	0.1
712.4	0.2	0.1
825.0	0.1	0.0
955.4	0.0	0.0

Figure 4.25 Size distribution of TiB_2 particulates in the S700-30 sample.

4.1.4 Ultrasound Assisted Mixed-salts Reaction at 700 °C

1) XRD Analysis of Products

Figure 4.26 shows the XRD patterns of the slag and UTS700-10 sample produced by the ultrasound assisted mixed-salt reaction with a 10-min reaction time. $KAlF_4$ and K_3AlF_6 were also the two main phases in the slag; and TiB_2 was the only newly formed phase in the UTS700-10 sample, indicating that the mixed-salts reaction in ultrasonic fields was also conducted according to the chemical formula shown in Eq. 2.8. Furthermore, it is clear that the diffraction peaks of TiB_2 phase in the UTS700-10 sample were much stronger than those in the S700-10 sample, indicating that ultrasound can significantly improve the synthesis of TiB_2 in the mixed-salts reaction.

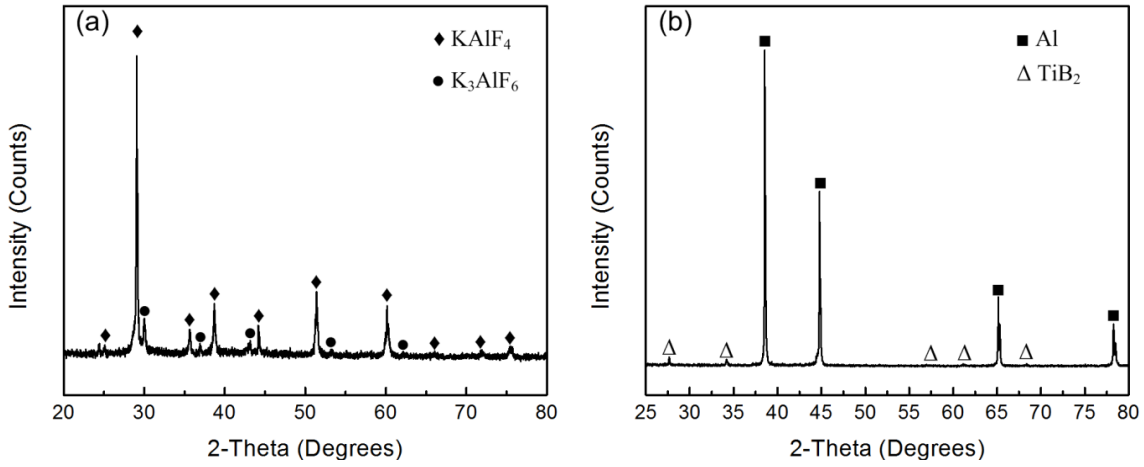

Figure 4.26 XRD patterns of the slag (a), and UT sample (b) produced with a 10-min reaction time.

2) SEM Analysis of UTS700-10 Sample

Figure 4.27 shows the microstructural features of the deep-etched UTS700-10 sample. The newly formed phase was located at the boundaries of α-Al grains with a

network structure, as shown in Figure. 4.27a. After magnification, it is found that the reticular phase was composed of by plenty of tiny in situ formed TiB_2 particulates which were identified by EDS, and these TiB_2 particles had different sizes, as shown in Figure. 4.28b and c. Due to the effect of particle pushing, the in situ formed TiB_2 particles were pushed by α-Al dendrites to the grain boundaries during the solidification process.

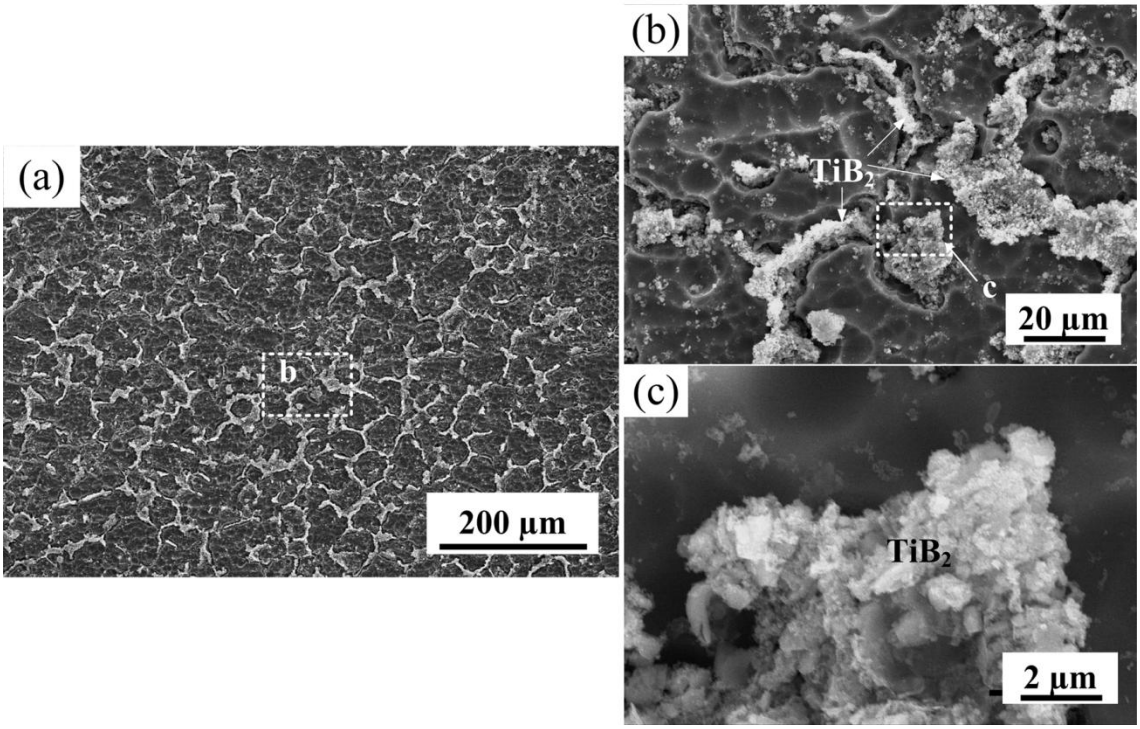

Figure 4.27 SEM images of the deep-etched UTS700-10 sample.

3) XRD Analysis of Extracted TiB_2 Particles from UTS700-10 Sample

Only TiB_2 phase was detected in the extracted particles from the UTS700-10 sample, as shown in Figure 4.29. Based on the XRD results, it is clear that no any other phases influenced the analyses about the yields and size distribution of TiB_2 particulates.

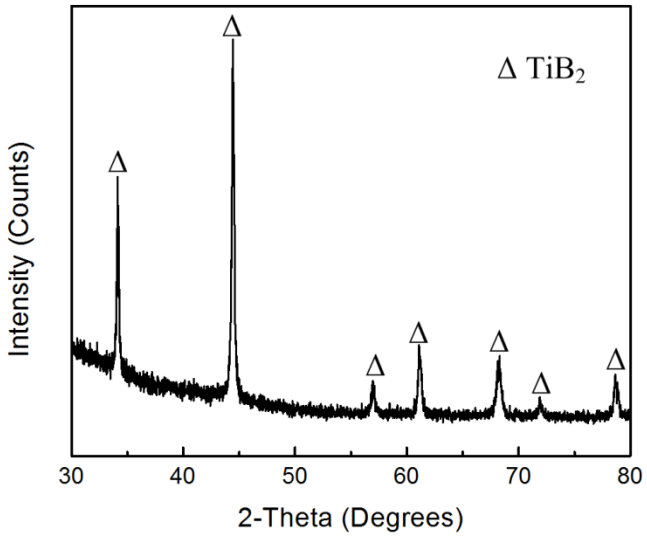

Figure 4.28 XRD pattern of the extracted TiB_2 particles from the UTS700-10 sample.

4) Yield of TiB_2 Particulates in UTS700-10 Sample

Table 4.7 shows the actual weight percentage of in situ formed TiB_2 particulates in the UTS700-10 sample was about 4.52 wt. %, and the corresponding yield of TiB_2 was 90.4 %. The result showed that applying ultrasound to the mixed-salts reaction at 700 °C improved the formation of TiB_2 phase significantly. The effects of ultrasound on the reaction will be discussed in the following chapter.

Table 4.7 *Calculation of the yield of TiB_2 particulates in the UTS700-10 sample.*

Group	Quantity of the ingot for extracting experiment (g)	Quantity of extracted TiB_2 particles (g)	Actual weight percent of TiB_2 (wt. %)	Yield of TiB_2 (%)
1	7.156	0.316	4.42	88.40
2	7.766	0.358	4.61	92.20
Average	-	-	4.52	90.40

5) Size Distribution of TiB_2 Particulates in UTS700-10 Sample

The size distribution of in situ formed TiB_2 particulates in the UTS700-10 sample is shown in Figure 4.29. Almost all TiB_2 particles were smaller than 700 nm in size, and around 95 % of the TiB_2 particles were smaller than 300 nm. It is obvious that the use of ultrasound in the mixed-salts reaction at a lower temperature have its unique advantages. On the one hand, a high yield of TiB_2 can be obtained. On the other hand, the size of most of in situ formed TiB_2 particulates can be controlled under 300 nm.

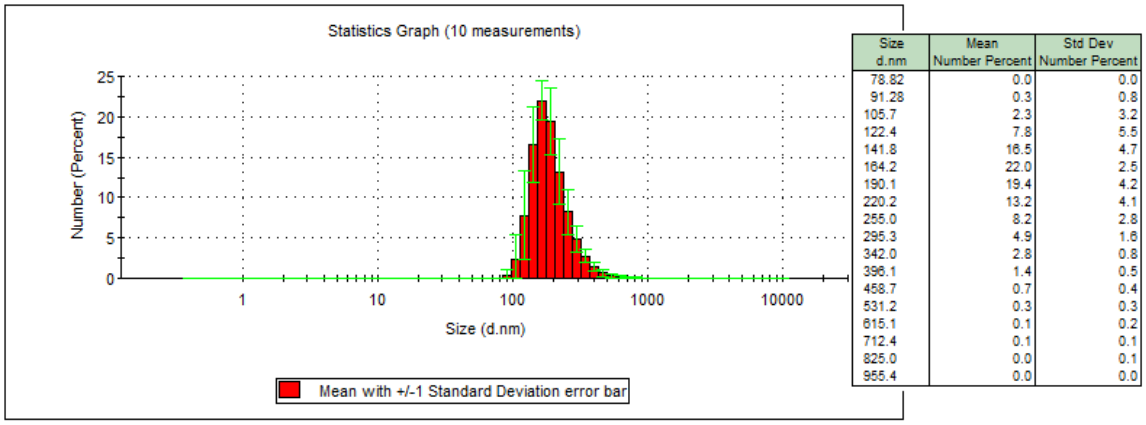

Size d.nm	Mean Number Percent	Std Dev Number Percent
78.82	0.0	0.0
91.28	0.3	0.8
105.7	2.3	3.2
122.4	7.8	5.5
141.8	16.5	4.7
164.2	22.0	2.5
190.1	19.4	4.2
220.2	13.2	4.1
255.0	8.2	2.8
295.3	4.9	1.6
342.0	2.8	0.8
396.1	1.4	0.5
458.7	0.7	0.4
531.2	0.3	0.3
615.1	0.1	0.2
712.4	0.1	0.1
825.0	0.0	0.1
955.4	0.0	0.0

Figure 4.29 Size distribution of TiB_2 particulates in the UTS700-10 sample.

Overall, the results of the mixed-salts reactions under different experimental parameters clearly are summarized in Table 4.7 with the aim of displaying the results clearly.

Table 4.8 *The summary of the mixed-salt reaction results under different experimental parameters.*

Sample	Yield of TiB_2 (%)	Size distribution of TiB_2 (nm)
S900-10	89.50	400-800nm (79.10 %), some are larger than 1 μm
S900-30	90.30	400-800nm (83.10 %), some are larger than 1 μm
S800-10	70.30	< 300nm (95 %), some are larger than 1 μm
S800-30	76.00	< 300nm (95 %), some are larger than 1 μm
S700-10	28.10	< 300nm (95 %)
S700-30	35.50	< 300nm (95 %)
UTS700-10	90.40	< 300nm (95 %)

4.2 Results of the Static Experiment

4.2.1 Static Sample

Figure 4.30a shows the static sample fabricated via the mixed-salts reaction at 800 °C with a 10-second reaction time. A product-region could be observed clearly with naked eye in the sample. The thickness of layer in the sample was about 7 mm. Figure 4.30b presents the microstructure of region of the product-layer by using optical microscopy. A layered microstructure of products formed in the reaction was found, in which chain-like reinforcements and cluster-like reinforcements both existed in the Al matrix. According to the morphology of the product-region, it is clear that the mixed-salts reaction of K_2TiF_6-KBF_4-Al system took place at the interface between molten salts and Al. As the reaction proceeded, the products generated at the interface would deposit into the Al melt due to their heavier density than Al. Four typical areas chosen from the

product-region were further examined. These four areas contained the products which were synthesized at different reaction stages. Area 1 represented the reaction occurred at the starting stage, and Area 4 represented the reaction at the last stage.

In Area 1, some blocky Al_3Ti particulates smaller than 5 μm were found in the Al matrix, as shown in Figure 4.31. These Al_3Ti were generated due to the reaction between K_2TiF_6 and Al. It has been reported that the reaction between K_2TiF_6 and Al could take place at much higher rate than that between KBF_4 and Al (Mayes, McCartney, & Tatlock, 1993), especially at low temperatures. Arnberg et al. (1982a) also reported that the blocky Al_3Ti could be formed when the K_2TiF_6 salt was added to molten Al at a temperature of about 750-800 °C.

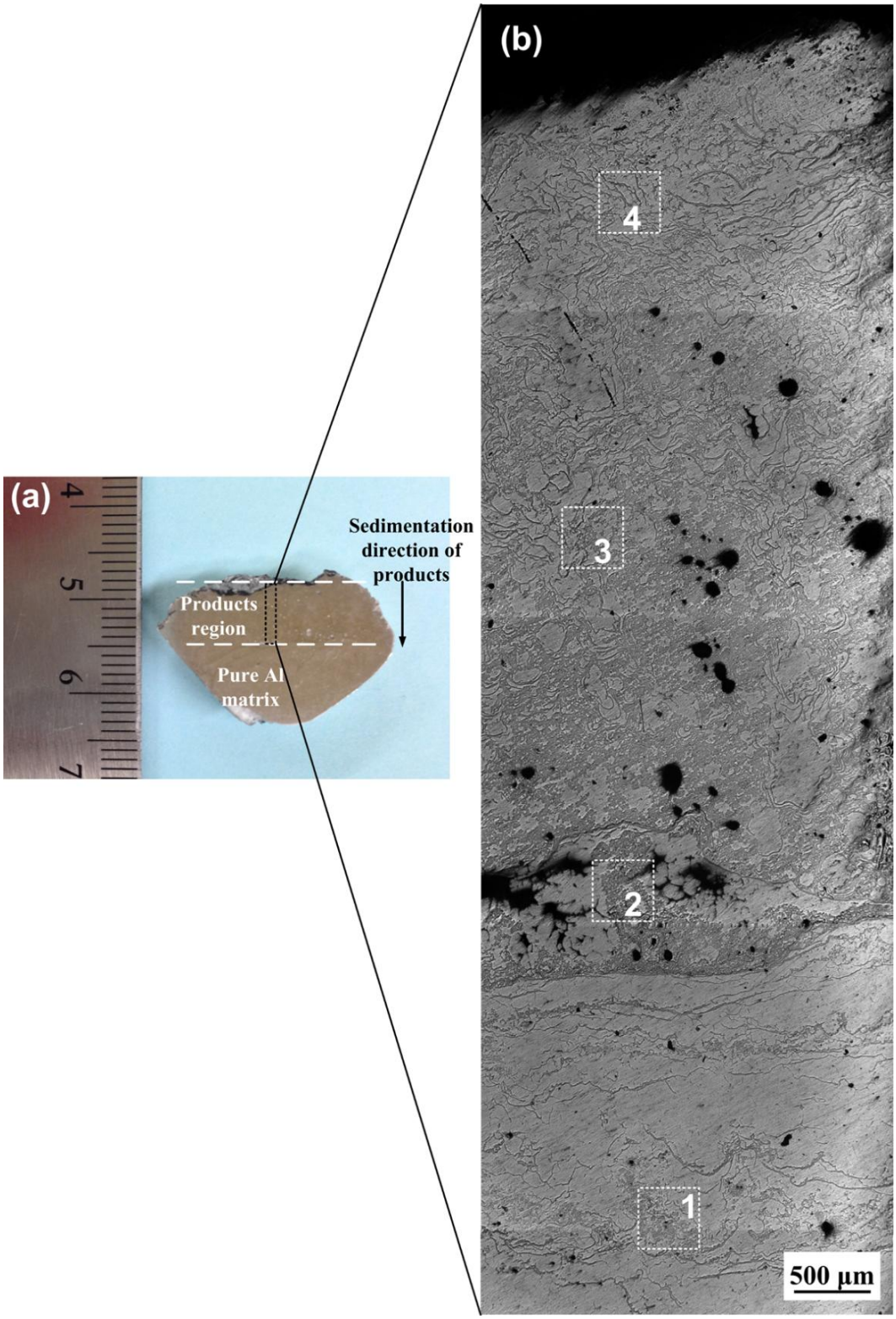

Figure 4.30 Static sample fabricated at 800 °C with a 10-second reaction time (a), and microstructure of the region containing products (b).

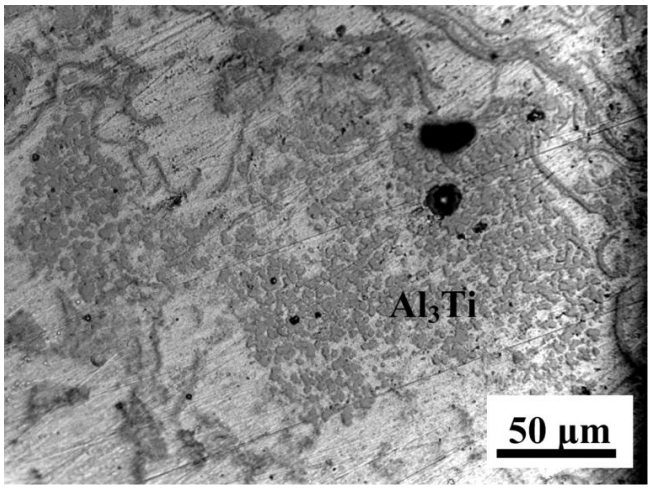

Figure 4.31 Al_3Ti particulates found in Area 1.

Figure 4.32 shows the microstructure of Area 2 in the sample. In this area, some blocky Al_3Ti particulates in clusters, as well as some tiny TiB_2 particulates were both found.

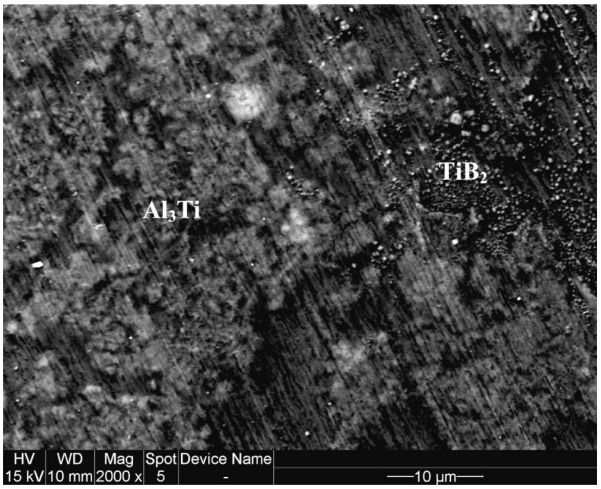

Figure 4.32 SEM image of Area 2.

Figure 4.33 shows the microstructure of Area 3 in the sample. Two types of reinforcements existed in the Al matrix. One was chain-like reinforcement with different

sizes. Some large-sized chain-like reinforcements had the width of about 10 μm and length exceeding 100 μm, and others were much thinner and shorter. The other one was cluster-like reinforcement. Based on the EDS mapping analysis, two types of reinforcements were both consisted of Al, Ti and B elements, as shown in Figure 4.33b, c and d. It is obvious that the cluster-like reinforcement contained more Al element than the chain-like reinforcement. According to the results, TiB_2 and Al_3Ti were dominated in the chain-like and cluster-like reinforcements respectively. More detailed analyses about the two reinforcements were conducted based on the SEM images with higher magnification (Figure 4.34 and 4.35).

More detailed information about the chain-like reinforcement is provided in Figure 4.34. A fragment of the chain-like reinforcement (Figure 4.33a (1)) was picked up for analyzing, as shown in Figure 4.34a. Some tiny TiB_2 particulates with the size of about 200 nm were found around the chain-like reinforcement. Figure 4.34b shows a higher magnification of the area marked in Figure 4.34a. It is clear that some rather small-sized particles which were smaller than 200 nm in size existed in the reinforcement. According to the EDS mapping analysis, these small particles were TiB_2. It is also should be mentioned that in some small areas of the reinforcement, the content of TiB_2 particles was rather low and no obvious TiB_2 particulates were found, as shown in Figure 4.34a.

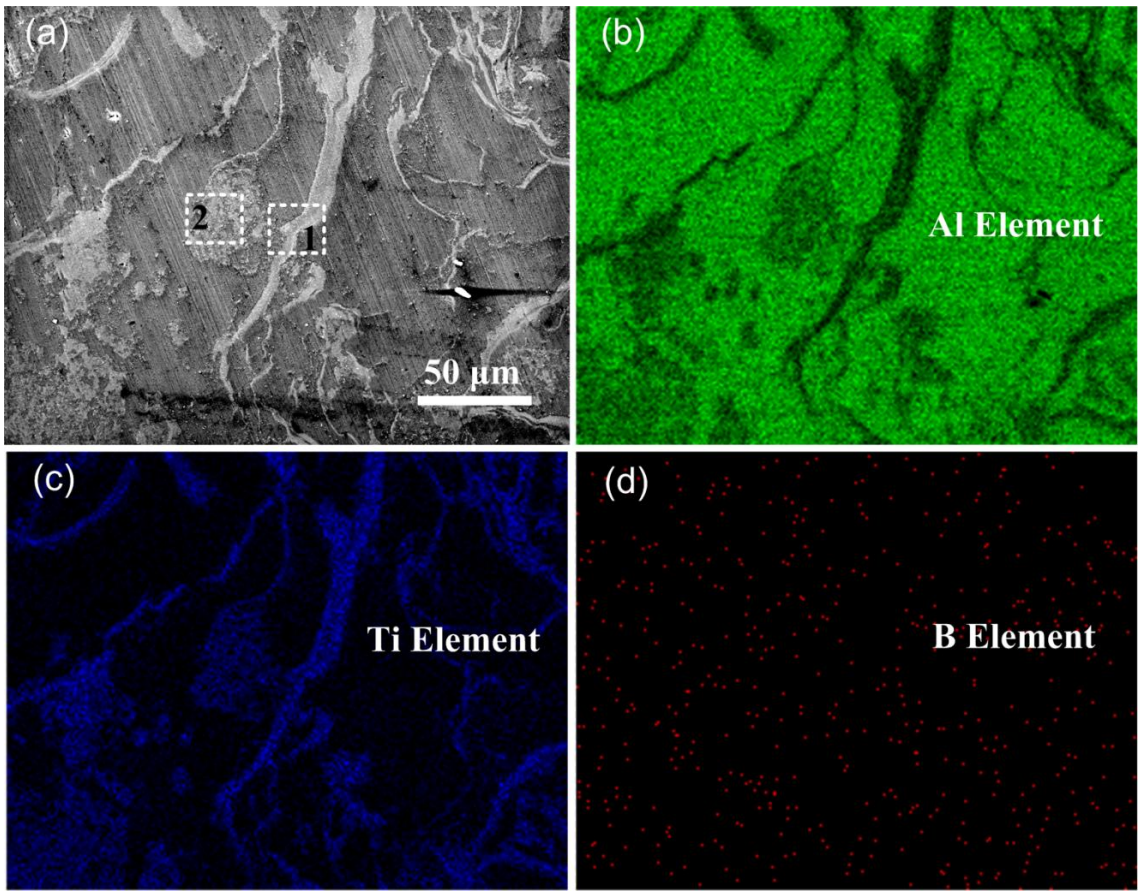

Figure 4.33 SEM image and EDS mapping (Al, Ti, B) of Area 3.

Combining the EDS analysis and the SEM result, it is inferred that these areas might be Al_3Ti phase. So the chain-like reinforcements in the Al matrix were consisted of by plenty of TiB_2 particles and Al_3Ti phase. These TiB_2 particles were located separately in the Al_3Ti phase. Actually, the amounts of the two phases in the chain-like reinforcement can be changed under different experimental conditions, such as the reaction temperature and the motivation of external fields (ultrasonic fields). These factors are able to influence the chemical reaction directly. Increasing the reaction temperature, for example, can accelerate the reaction rate because higher temperature can increase the reaction activity of the reactants. More thermodynamically stable phase can

be synthesized. The further analysis about the influence of reaction temperature and ultrasound will be conducted in detail later in the following chapter.

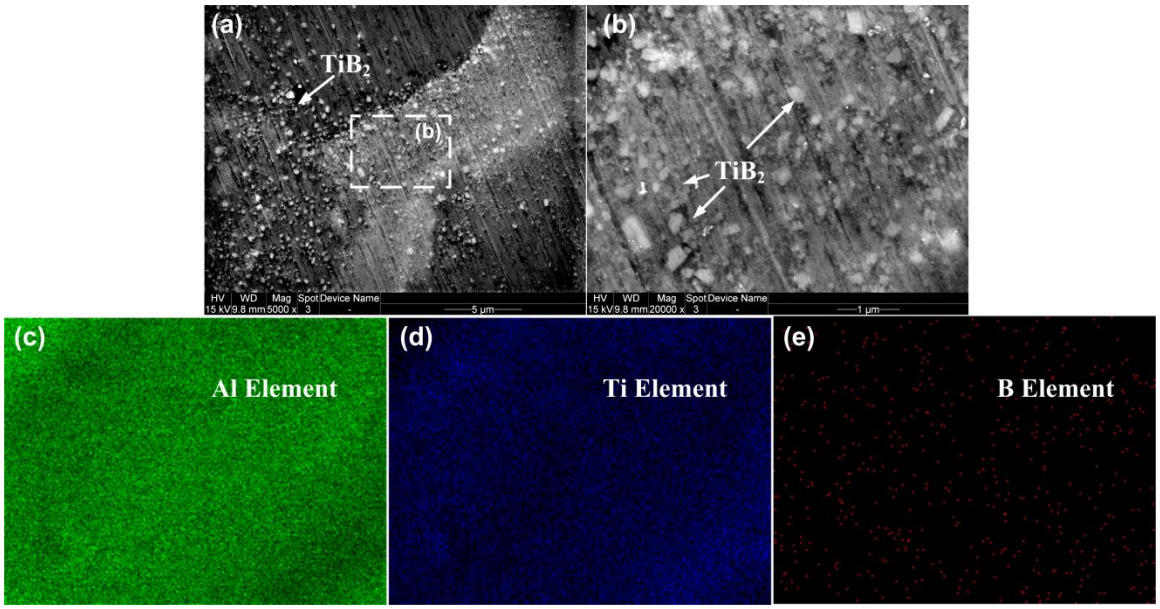

Figure 4.34 (a) SEM image of the area marked in Figure 4.33a (1), (b) a higher magnification of the area marked in (a), and EDS mapping (Al (c), Ti (d), and B (e)) of (b).

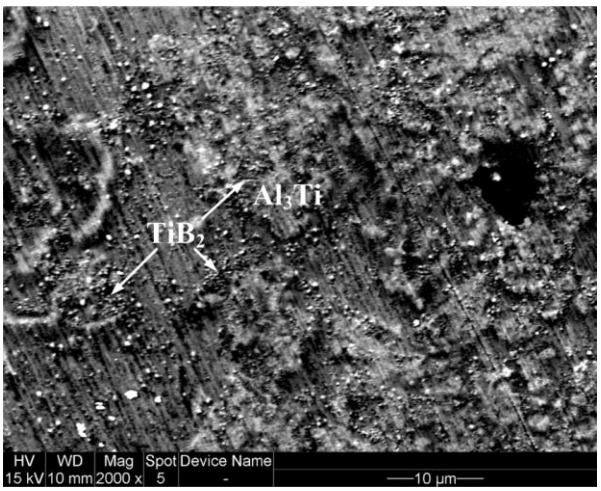

Figure 4.35 SEM image of the area marked in Figure 4.33a (2).

Figure 4.35 shows the microstructure of the cluster-like reinforcements (as shown in Figure 4.33a (2)), in which two typical phases existed together. According to the EDS analysis, the large-sized particles were Al_3Ti, and the rather small-sized particles were TiB_2.

Figure 4.36a presents the microstructure of Area 4 marked in Figure 4.30. A specific area of the reinforcement was zoomed in step by step in order to display the features clearly, as shown in Figure 4.36b, c and d, respectively. On the one hand, plenty of small-sized TiB_2 particles with the size less than 200 nm existed around the chain-like reinforcement. On the other hand, it is found that the chain-like reinforcement was consisted of lots of TiB_2 particulates, which were also smaller than 200 nm in size, as shown in Figure 4.36d.

Overall, in the static sample, TiB_2 and Al_3Ti were both synthesized in the mixed-salts reaction. For TiB_2 particulates, some of which existed in Al matrix, some existed in the chain-like reinforcements, and some existed together with blocky Al_3Ti particulates. For Al_3Ti, some of which existed separately in Al matrix, some existed in clusters, and some existed in the chain-like reinforcement.

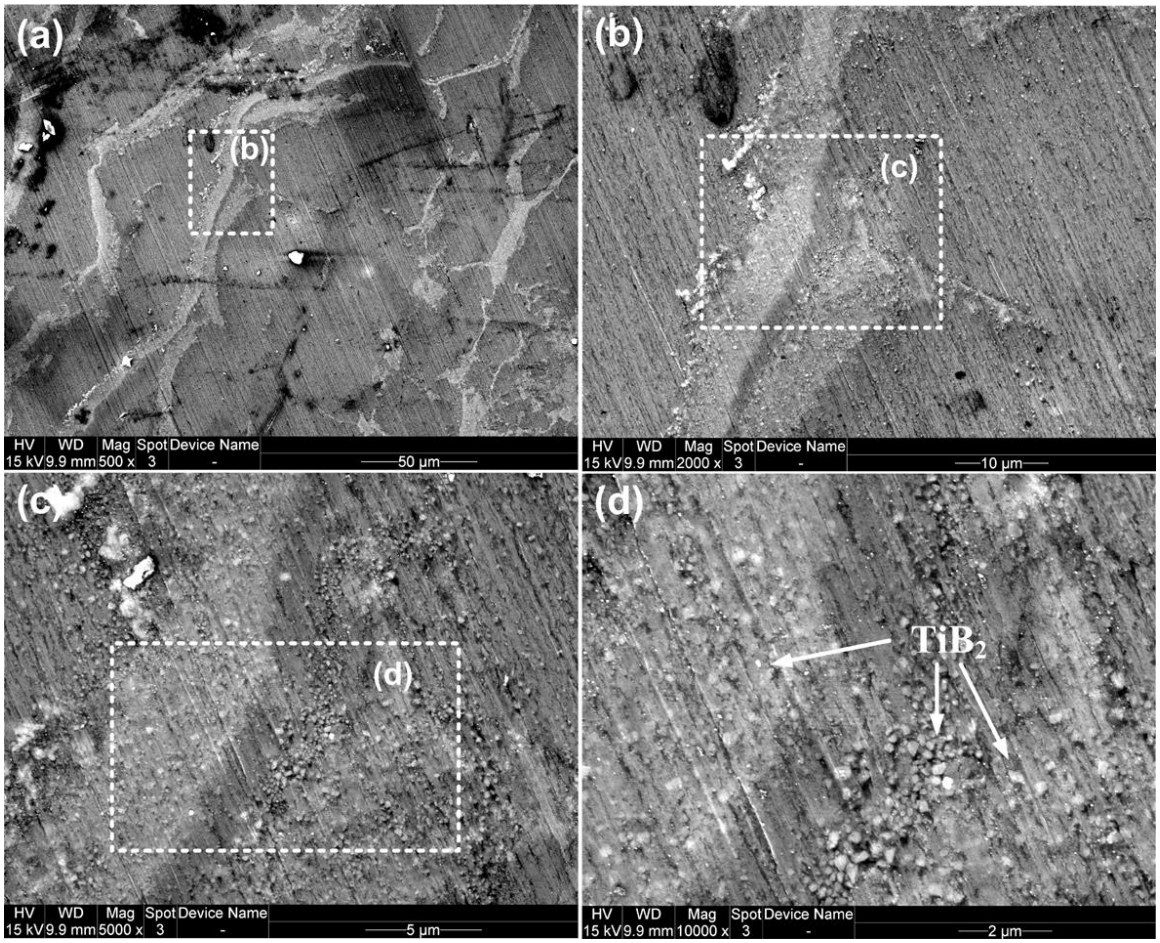

Figure 4.36 SEM images of Area 4 in the static sample.

4.3 Results of the Direct-melt Reaction

4.3.1 Direct-melt Reaction at 730 °C

4.3.1.1 S730 Samples Fabricated without Ultrasound

1) XRD Analysis of Samples Fabricated with Different Reaction Times

Figure 4.37 shows the XRD patterns of the S730 samples fabricated at 730 °C with different reaction times. Al_3Ti was the only newly formed phase in the reaction. The amount of in situ formed Al_3Ti phase was increased as the reaction time was prolonged according to the diffraction intensity of Al_3Ti peaks. The XRD results indicated that the

reaction for synthesizing Al_3Ti phase was successive from 1 min to 10 min. The evolution of solid Ti powders in liquid Al can be observed directly through the following SEM analysis.

2) SEM Analysis of S730 Samples Fabricated with Different Reaction Times

Figure 4.38 shows the typical microstructures of the S730 samples produced via the direct-melt reaction at 730 °C with different reaction times. The evolution of solid Ti powders in liquid Al was shown clearly by observing samples from S730-1 to S730-10. It is obvious that the solid Ti powders were unable to react with liquid Al completely in 10 min, for some Ti particles covered with reaction layers which were identified as Al_3Ti phase by EDS were found in the matrix after solidification. Also, the thickness of Al_3Ti reaction layers was increased as the reaction time was prolonged, which could reach around 5, 10, 15 and 25 μm in S730-1, S730-3, S730-5 and S730-10 samples, respectively. In addition, in situ formed Al_3Ti particles aggregated together around these Ti powders. The amount of Al_3Ti particles was increased with increasing the reaction time, as shown in Figure 4.38b, c and d. This trend is in good agreement with the XRD results in Figure 4.37.

Furthermore, based on the results of SEM, some important features about the Al_3Ti reaction layers were also found in the S730 samples. One was that the outside part of reaction layer was composed of by some loose Al_3Ti particles with weak bonds. Second one was that the size of Al_3Ti particles in the reaction layer became larger from inside to outside of the layer. Third one was that some inter-Al_3Ti particle spacings existed in the reaction layer. The above three features about reaction layers were shown

clearly in Figure 4.38b, c and d, respectively. Also, the in situ formed Al_3Ti particulates located in the matrix were blocky in morphology and were smaller than 5 μm in size in the four S730 samples.

The results clearly showed that a lower Al melt temperature can lead to the formation of small blocky Al_3Ti particulates. The formation mechanism of small blocky Al_3Ti particulates via the direct-melt reaction will be discussed later in this dissertation.

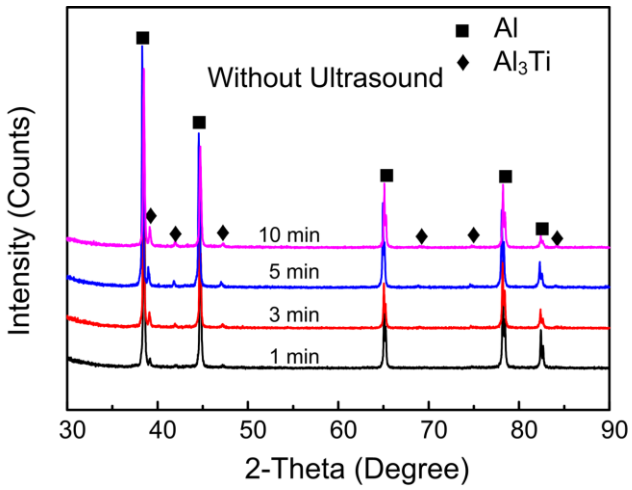

Figure 4.37 XRD patterns of the S730 samples fabricated at 730 °C with different reaction times.

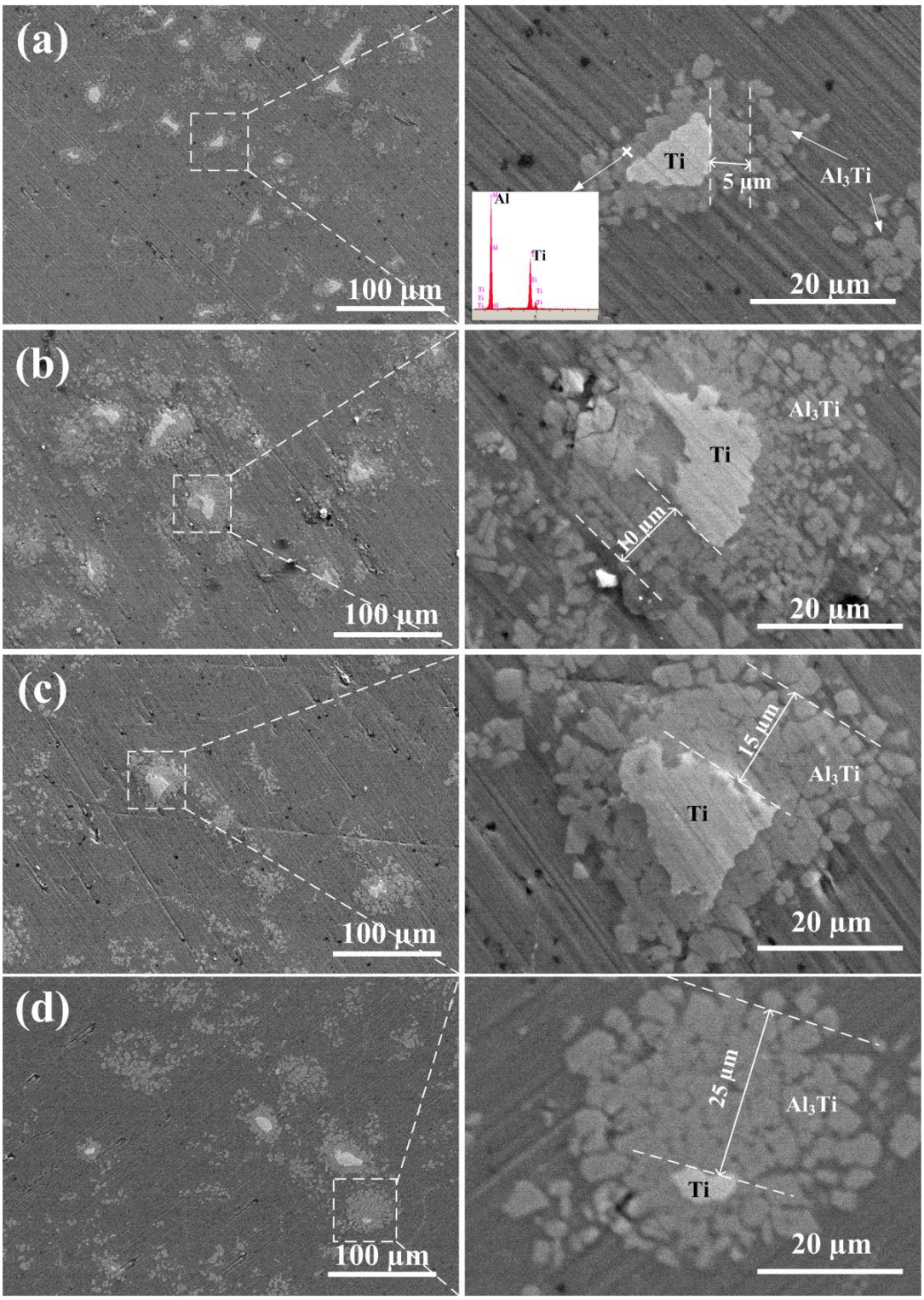

Figure 4.38 Typical microstructures of the control samples (S730) with different reaction times and higher magnification of areas marked in images: (a) 1 min, (b) 3 min, (c) 5min, and (d) 10 min.

4.3.1.2 S730 Samples Fabricated with Ultrasound

1) XRD Analysis of UTS730 Samples Fabricated with Different Times

Figure 4.39 shows the XRD patterns of the ultrasonically treated samples fabricated at 730 °C with different reaction times. Similar to the S730 samples (control samples), Al_3Ti was the only newly formed phase detected by XRD in the UTS730 samples, and the amount of Al_3Ti phase was increased with increasing the reaction time. It was found that there was no significant difference in the diffraction intensity of Al_3Ti phase between the US730-5 and the US730-10 samples, indicating that the Al_3Ti contents in both samples were similar. In addition, it is also found the amount of Al_3Ti phase in the UTS730 sample was obviously higher than that in the S730 sample with the same reaction time, which indicated that high-intensity ultrasound promoted the formation rate of Al_3Ti phase in the direct-melt reaction.

2) SEM Analysis of US730 Samples Fabricated with Different Times

Similarly, Figure 4.40 shows the typical microstructures of the ultrasonically treated samples (UTS730) with different reaction times. After 1 min of ultrasonic treatment, a few of solid Ti powders covered by Al_3Ti layers existed in the matrix, and the thickness of the reactive layer was around 5 μm, as shown in Figure 4.33a. As the reaction time was increased to 3 min, most of the solid Ti powders reacted with liquid Al completely, a very few of unreacted large-sized Ti powders covered with Al_3Ti layers were found in the Al matrix, and the thickness of reaction layer was around 5 μm, as shown in Figure 4.33b. Moreover, Al_3Ti layers in the ultrasonically treated samples were gear-like in morphology (as shown in Figure 4.40a and b), suggesting that some outside

Al_3Ti particles in reaction layer were peeled off from the reaction layer in the ultrasonic fields. After 5 min, all solid Ti powders reacted completely with liquid Al (Figure 4.40c), since no unreacted Ti particles were found in the Al matrix, indicating the reaction between solid Ti powders and liquid Al was promoted greatly in the ultrasonic fields. After 10 min, only the in situ formed Al_3Ti particulates existed in the UTS10 sample (Figure 4.40d). This trend of the amount of in situ formed Al_3Ti phase in the ultrasonically treated samples was also in good accordance with the XRD results in Figure 4.39. In addition, the distributions of in situ formed Al_3Ti particulates became more homogeneous in the matrix as the ultrasonic processing time was increased. The Al_3Ti particulates synthesized in the four ultrasonically treated samples were blocky in shape, having the size smaller than 5 μm.

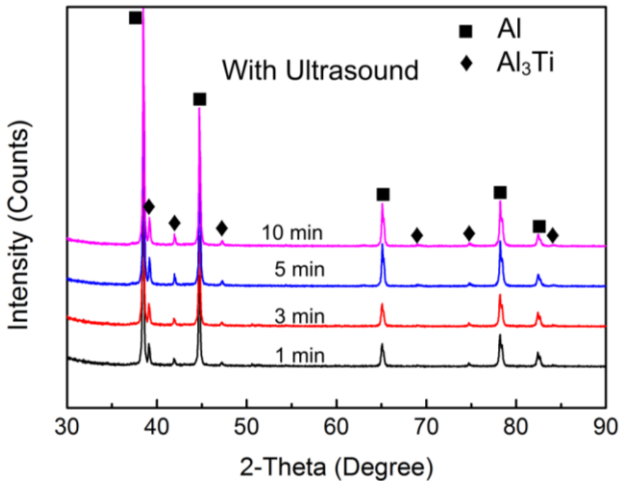

Figure 4.39 XRD patterns of the UTS730 samples with different reaction times.

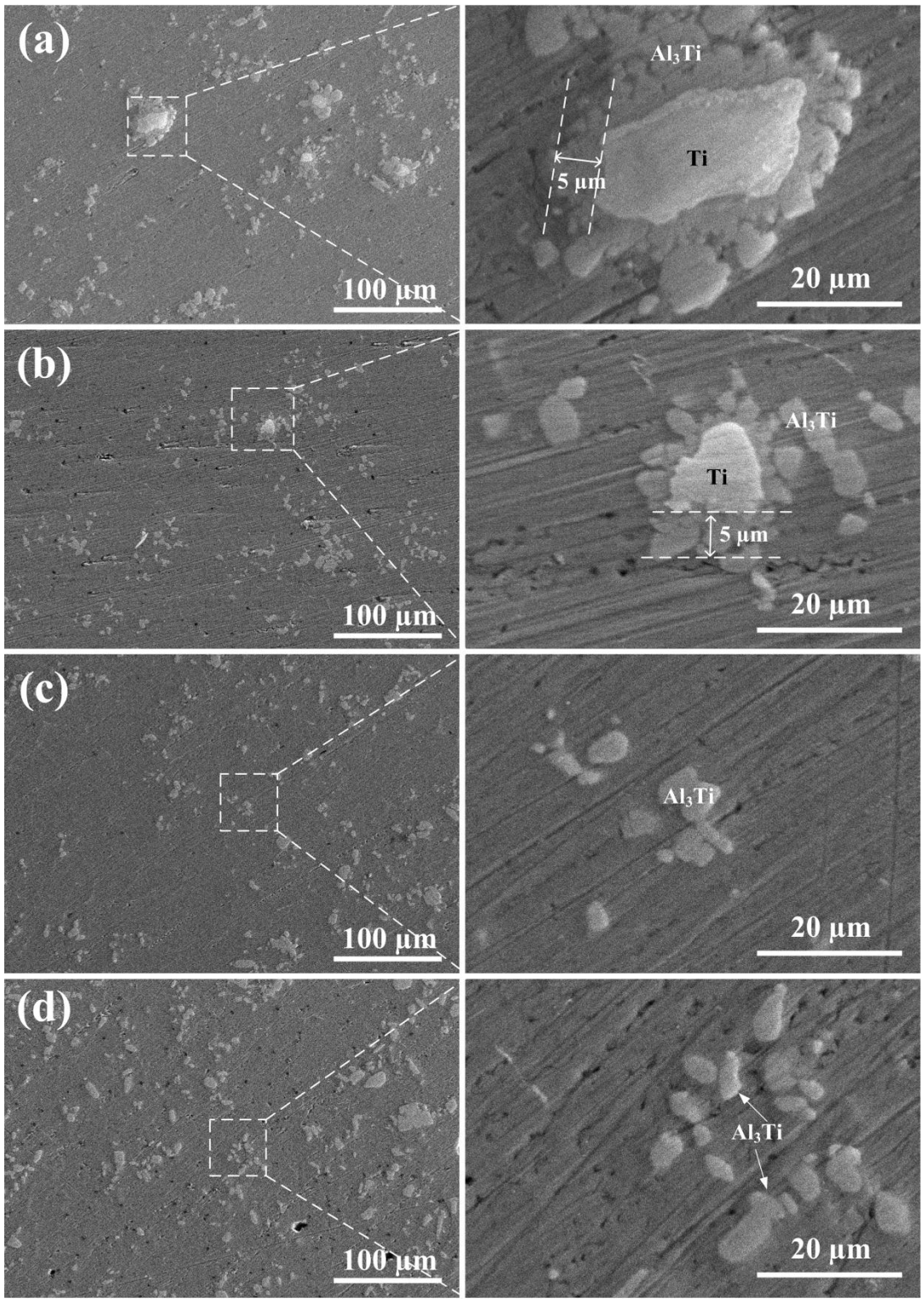

Figure 4.40 Typical microstructures of the ultrasonically treated samples (UTS730) with different reaction times and higher magnification of the areas marked in images: (a) 1 min, (b) 3 min, (c) 5min, and (d) 10 min.

4.3.2 Direct-melt Reaction at 700 °C

4.3.2.1 S700 Sample Fabricated without Ultrasound

After adding solid Ti powders into molten Al at 700 °C, it was found that the Ti powders wrapped in an Al foil were hard to disperse. In contrast, some inclusions including Ti powders were easily formed in molten Al. After 10 min, the molten Al was poured into a steel mold to form an ingot. Plenty of unreacted Ti powders were found at the bottom of the crucible, as shown in Figure 4.41. Four groups of experiments at 700 °C were repeated in this research, but the similar issue occurred in each group, even though a mechanical stirring was applied. The results showed that once these inclusions were formed, the reaction between solid Ti and liquid Al was severely hindered, and the commonly used mechanical stirring was unable to effectively break up these inclusions. Based on this research, the direct-melt reaction between solid Ti powders and liquid Al is hard to take place at 700 °C.

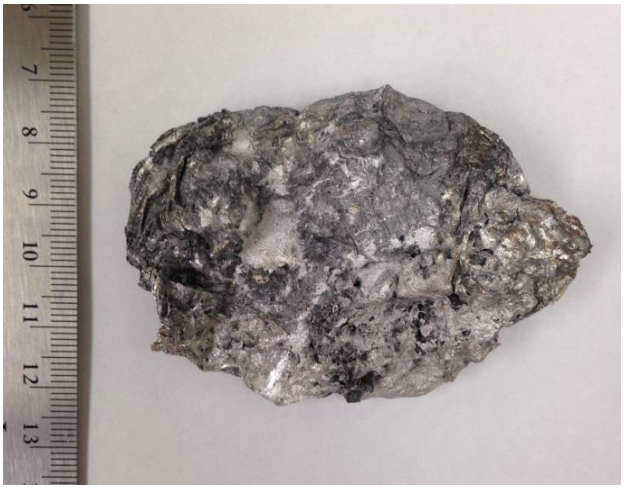

Figure 4.41 An inclusion including solid Ti powders.

(1) XRD Analysis of S700-10 Sample

Figure 4.42 shows the XRD pattern of the S700-10 sample. No any other phases were detected besides Al phase in the sample, indicating that the direct-metal reaction for synthesizing Al_3Ti is hard to take place at 700 °C.

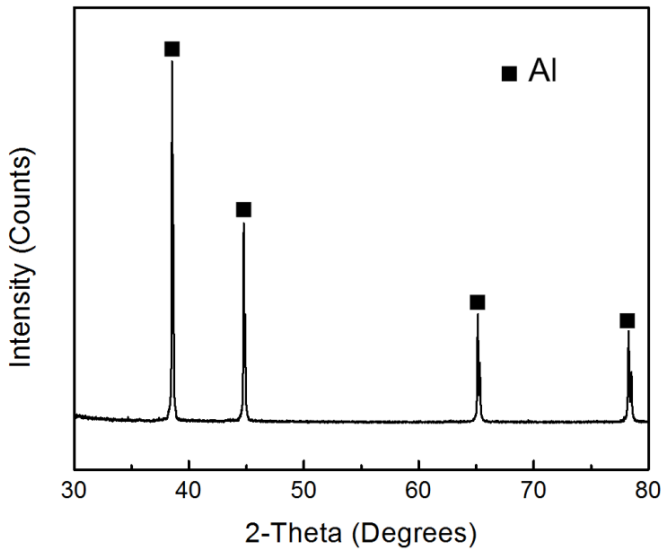

Figure 4.42 XRD pattern of the S700-10 sample fabricated at 700 °C with a 10-min reaction time.

(2) SEM Analysis of S700-10 Sample

The microstructure of the S700-10 sample was observed by SEM, as shown in Figure 4.43. Only individual Ti particle with Al_3Ti phase occasionally existed in the matrix, as shown in Figure 4.43a. The reaction layer on Ti particle was consisted of some blocky Al_3Ti particles, and the thickness of reaction layer could reach about 20 μm, as shown in Figure 4.43b. The result showed that most Ti powders did not react with liquid Al at 700 °C. For the solid Ti powder reacted with Al at 700 °C, it had a similar evolution as the solid Ti powders in molten Al at 730 °C.

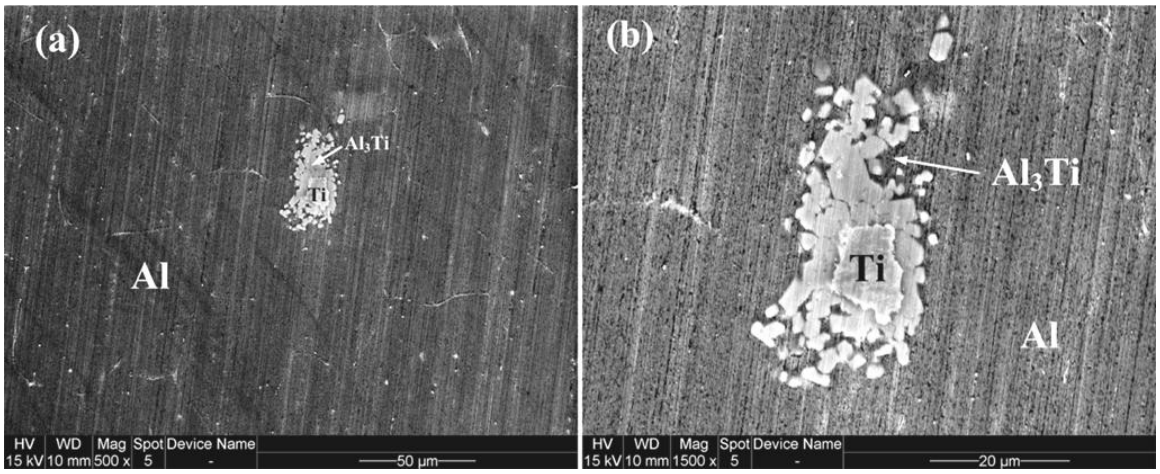

Figure 4.43 Microstructure of the S700-10 sample (a), and Ti particle with Al_3Ti phase at higher magnification (b).

4.3.2.2 UTS700 Samples

(1) XRD analysis of UTS700 Samples

Figure 4.44 presents the XRD patterns of the UTS700 samples fabricated at 700 °C with different reaction times (5 min and 10 min). Newly formed Al_3Ti phase were detected clearly in both samples, indicating that the direct-metal reaction for synthesizing Al_3Ti occurred at 700 °C in ultrasonic fields. Also, the Al_3Ti peaks in the UTS700-10 sample (Figure 4.44b) were stronger than those in the UTS700-5 sample (Figure 4.44a), which indicated that more Al_3Ti phase was obtained as the reaction time was prolonged from 5 to 10 min.

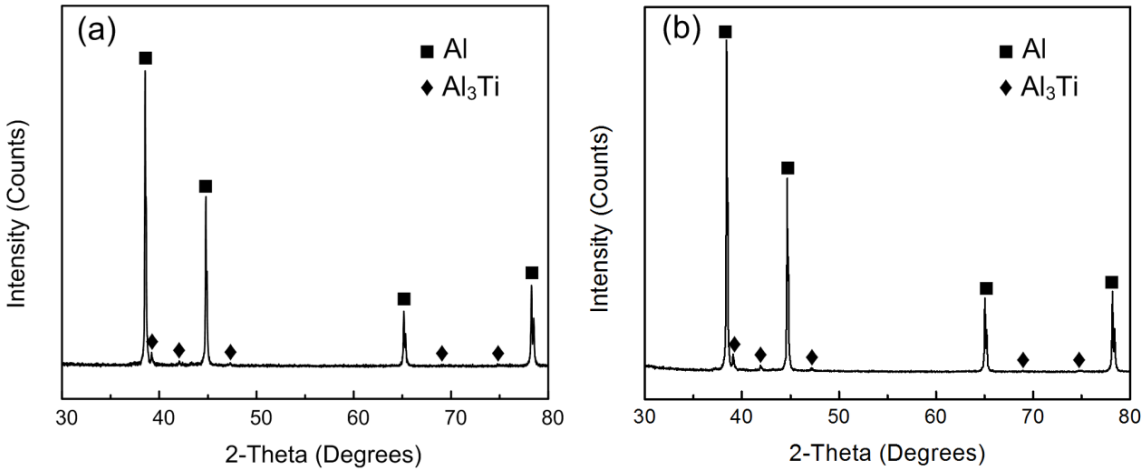

Figure 4.44 XRD patterns of the UTS700 samples: (a) 5 min, and (b) 10 min.

(2) SEM Analysis of UTS700 Samples

The microstructures of the UTS700-5 and UTS-10 samples are shown in Figure 4.45a and Figure 4.45b. Some blocky Al_3Ti particulates were synthesized in both sample, and most of these particulates were smaller than 5 μm in size. In the UTS700-5 sample, some Ti particles wrapped by reaction layers were found, indicating that a 5-min reaction time was not enough for a completed reaction. The reaction layer was composed of by some blocky Al_3Ti particles, the thickness of which was about 5 μm, as shown in Figure 4.45a. No unreacted Ti particles were found in the UTS700-10 sample, indicating that the direct-melt reaction between solid Ti powders and liquid Al can be conducted completely with a 10-min reaction time in ultrasonic fields. The size of most block-like Al_3Ti particulates synthesized in both samples was smaller than 5 μm.

The results clearly showed that ultrasound was able to make the direct-melt reaction take place at a lower reaction temperature (700 °C). The effects of ultrasound on the direct-metal reaction became more obvious at a lower reaction temperature. The

effects of ultrasound on the direct-melt reaction will be discussed in detail in the following chapter.

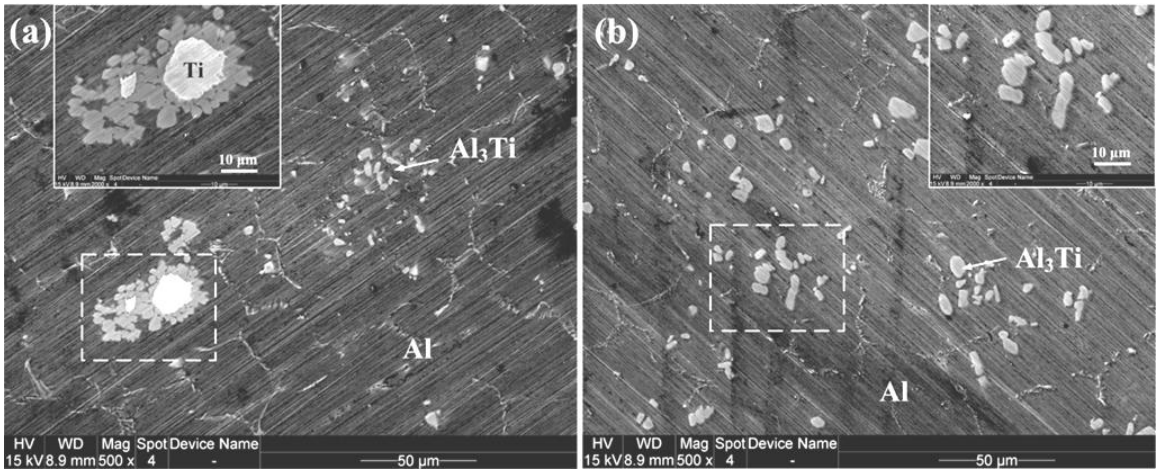

Figure 4.45 Microstructures of the UTS700-5 sample (a) and the UTS700-10 sample (b).

CHAPTER 5. DISCUSSION, CONCLUSIONS AND FUTURE WORK

The mixed-salts reaction of K_2TiF_6-KBF_4-Al system for synthesizing TiB_2 particulates and the direct-melt reaction between solid Ti powders and liquid Al for producing Al_3Ti particulates were both studied in this research. The discussion of the experimental results presented in the previous chapter is divided into two parts regarding each reaction. The conclusions of this dissertation and future work are drawn in the end of this chapter.

5.1 Discussion of the Mixed-salts Reaction

The results clearly show that the experimental parameters, such as the reaction temperature and reaction time both influence the synthesis of TiB_2 particulates via the mixed-salts reaction. The reaction temperature is a more crucial factor, which decides the yield and size distribution of TiB_2 particulates produced in the reaction. In addition, the use of high-intensity ultrasound remarkably improves the yield of smaller-sized TiB_2 synthesized at 700 °C. The formation mechanism of TiB_2 regarding the Al melt temperature is clarified firstly in this section. And then the effects of ultrasound on the reaction at a lower temperature (700 °C) are discussed.

5.1.1 Formation Mechanism of TiB_2 Particulates

The static experiment provides the crucial route for studying the formation mechanism of TiB_2 in the mixed-salts reaction. The results in this research displayed the differences in the formation of TiB_2 at different temperatures (700 and 900 °C), such as the yields of TiB_2 particulates and their size distributions. It is noted that the reaction temperature plays a critical role in the mixed-salts reaction of K_2TiF_6-KBF_4-Al system. Accordingly, the related formation mechanism of TiB_2 might be different at different temperatures. The following discussion about the formation process of TiB_2 will be conducted considering the Al melt temperature.

It is obvious that the mixed-salts reaction of K_2TiF_6-KBF_4-Al system is an interface reaction based on the following reasons.

Firstly, according to the microstructure of the static sample shown in Figure 4.30, a layer structure of products was obtained in the static sample with a 10-sec reaction time. The layer was distributed along the direction from the top to the bottom of the crucible.

Secondly, the SEM analyses (Figure 4.36) showed that the in situ formed TiB_2 particulates aggregated in a lamellar morphology. When a longitudinal profile was made to observe the reaction area, a chain-like structure of reinforcement was found in the sample. Since the lamellar reinforcement has a greater density than Al, which can deposit during the reaction process. Plenty of similar lamellar reinforcements which were parallel to the salts/Al interface were found in the static sample, which clearly proved that the mixed-salts reaction is an interface reaction.

It should be noted that the above interface reaction just realizes the transfers of Ti and B from salts to molten Al. Since TiB_2, Al_3Ti and AlB_2 were all existed in the samples

produced in the mixed-salts reactions at 800 and 700 °C, the formation process of TiB_2 in the reaction is not simple.

Based on the results of static experiment and the series of S900, S800 and S700 samples obtained in Chapter 4, the possible formation process of TiB_2 phase in the mixed-salts reaction is discussed below. In order to clearly describe the process, two critical steps in the reaction are listed respectively.

5.1.1.1 Transfers of Ti and B from Salts to Al Melt

First all of, no obvious KF and AlF_3 phases were found in the slags produced in the mixed-salts reaction at different temperatures. Thereby, the Ti and B in Al are not from the reactions of TiF_4 (gas)-Al and BF_3 (gas)-Al, in which the TiF_4 and BF_3 gases are from the decomposition of K_2TiF_6 and KBF_4. Accordingly, the formation processes described in Eqs 2.9, 2.10, 2.11 and 2.12 are not suitable to explain the formation of TiB_2 phase. At least, the formation of most TiB_2 phase in the mixed-salts reaction does not follow the chemical reaction shown in Eq. 2.16.

Actually, it has been reported by Birol (2009) that even though K_2TiF_6 has a higher melting point than KBF_4, K_2TiF_6 can be reduced by Al, releasing Ti at approximately 220 °C; KBF_4 starts to be reduced by Al a while later at round 525 °C, possibly after its polymorphic transformation from orthorhombic to cubic structure is over. In this research, after the mixed salts are added on the surface of molten Al, Ti released from K_2TiF_6 and B released from KBF_4 both react with Al at the interface between salts and Al to form Al_3Ti and AlB_2 (AlB_{12} might be formed at higher reaction temperatures) by reduction reactions (as shown in Eqs.2.5 and 2.6). According to Al-Ti

and Al-B phase diagrams (Sigworth, 1984), as shown in Figure 5.1, Al_3Ti and AlB_2 are both soluble in molten Al. The newly formed Al_3Ti and AlB_2 phases can dissolve in molten Al immediately. And then a thin layer of liquid Al containing Ti and B adjacent to the interface can be formed. The processes can be expressed as follows:

$$Al_3Ti \xrightarrow{dissolving} [Ti]_{Al} + 3Al \qquad \text{Eq. 5.1}$$

$$AlB_2 \xrightarrow{dissolving} 2[B]_{Al} + Al \qquad \text{Eq. 5.2}$$

Actually, the above processes are significantly influenced by the temperature of molten Al. Higher contents of [Ti] and [B] in the thin layer are obtained easily at higher reaction temperatures. On the one hand, the reduction reactions between salts and Al become more active, and more Al_3Ti and AlB_2 phases can be obtained at a higher temperature. On the other hand, according to the phase diagrams in Figure 5.1, the solubilities of Al_3Ti and AlB_2 phases in molten Al become larger as the temperature is increased. Thereby, increasing the temperature can accelerate the transfer speed of Ti and B to molten Al effectively. In contrast, at lower temperatures, more Ti and B might exist as Al_3Ti and AlB_2 respectively at the reaction interface, because of the limited solubilities of the two phases.

It has been proved that the reaction between K_2TiF_6 and Al occurs at a much higher rate than that between KBF_4 and Al. Thereby, the ratio of Ti/B in the thinner layer located at the reaction interface is easy to be greater than ½, and this ratio will become greater as the temperature of molten Al is decreased. This means that at the early stage of the mixed-salts reaction, the reaction to form TiB_2 is less complete and the intermediate Al_3Ti exists in a larger quantity than is required to form TiB_2 with AlB_2 (Lakshmi, Lu, &

Gupta, 1998a). In the static sample, some blocky Al_3Ti particulates were found in the Al matrix at the early stage of the reaction (Figure 4.31).

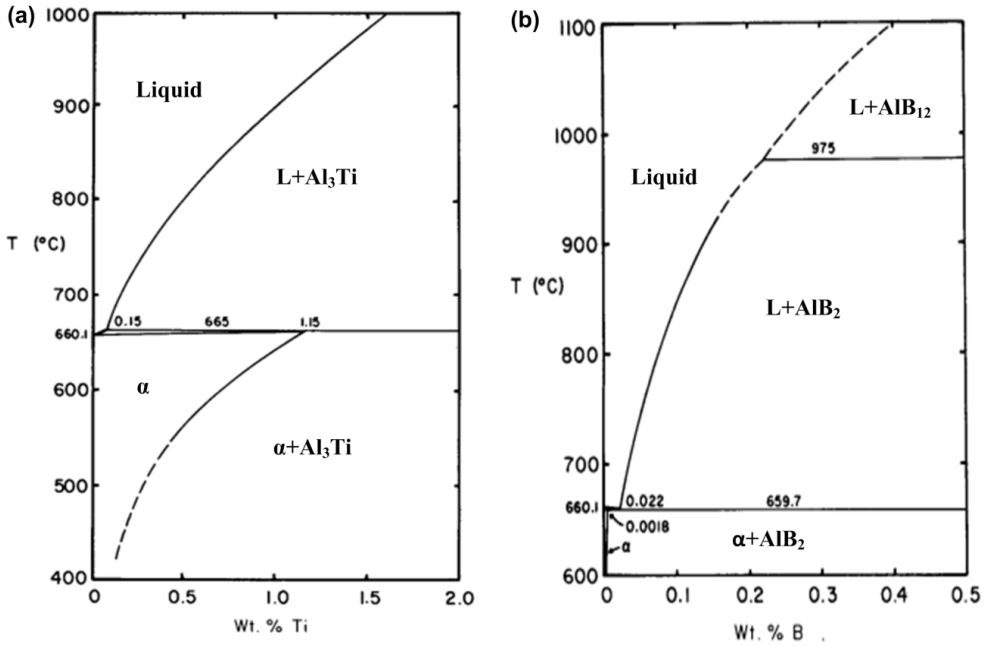

Figure 5.1 The aluminum-rich side of the Al-Ti phase diagram (a), and the aluminum-rich side of the Al-B phase diagram (b). Both of which were reproduced according to Sigworth (1984).

5.1.1.2 Formation of TiB_2 Phase

By comparison, it is found that the yield and size of TiB_2 formed at 900 °C were both much greater than those of TiB_2 synthesized at 700 °C. It is clear that the reaction temperature plays a crucial role in the mixed-salts reaction.

As mentioned above, Ti and B can be easily obtained in the thin layer of Al at the reaction interface. When the solutes [Ti] and [B] in liquid Al reaches saturation, they might be separated out as the compounds Al_3Ti, AlB_2 and TiB_2 in the ternary system of Al-Ti-B. Based on the thermodynamic calculations in the Chapter 2, TiB_2 is the most

thermodynamically stable phase due to its lowest free energy of formation among the three compounds. In addition, according to the phase diagram of Al-Ti-B shown in Chapter 2 (Figure 2.5), rather low contents of Ti and B can lead to the formation of TiB_2 phase. At a certain temperature, after the concentrations of [Ti] and [B] reach saturation in the Al melt, TiB_2 nuclei are formed, and then TiB_2 particles start to grow up due to the deposition of more Ti and B. In this research, in situ formed TiB_2 particles had a rather small size. It is suggest that the precipitation-growth mechanism might be more suitable to explain the formation of TiB_2 particles during the mixed-salts reaction.

It is well known that the formation of TiB_2 is influenced not only by the thermodynamic factor, but also by the kinetic factor at a certain temperature. Thereby the final formation of TiB_2 phase is controlled by the transfers of Ti and B from molten salts to liquid Al.

A higher Al melt temperate can result in a higher concentration of solutes in liquid Al, because the mass transfers of Ti and B from salts to the reaction interface become faster, and the dissolutions of Al_3Ti and AlB_2 into molten Al become faster as well. On the one hand, the Ti/B ratio in the reaction layer is much closer to 1/2, so plenty of TiB_2 phase can be formed. In the meantime, the formation of Al_3Ti phase can be limited effectively. On the other hand, the size of TiB_2 particulates can become larger, since more Ti and B can be provided in the growth process of TiB_2 particulates in a short time. The mixed-slats reaction for synthesizing TiB_2 phase can be completed in a short reaction time. In this research, when the reaction temperature was 900 °C and the reaction time was 10 min, no Al_3Ti phase was found in the Al matrix, the yield of TiB_2 reached 89.50 %, and the size of most of in situ formed TiB_2 particulates was in the range of 400-

800 nm. As the reaction time was increased to 30 min, no obvious change occurred in the S900-30 sample, in which the yield of TiB_2 was about 90.30 % and the size of most TiB_2 particulates was in the range of 400-800 nm, as shown in Figure 5.2a. It is clear that the S900-30 sample was similar with the S900-10 sample regarding the yield and size distribution of TiB_2 particulates.

Figure 5.2b shows the yields and size distributions of TiB_2 particulates in the S700 samples. When the mixed-salts reaction proceeded at 700 °C with a 10-min reaction time, some Al_3Ti (AlB_2 also should exist) phase existed in the Al matrix, the yield of TiB_2 was just about 28.10 %, and most of TiB_2 particulates were smaller than 300 nm in size. The yield of TiB_2 fabricated at 700 °C with a 30-min reaction time was 36.40 %, which was higher than that of TiB_2 in the S700-10 sample by about 29.50 %. Furthermore, the ratio of TiB_2 particulates with a smaller size was increased, which indicated that a certain amount of smaller-sized TiB_2 particulates were synthesized as the reaction time was prolonged from 10 to 30 min.

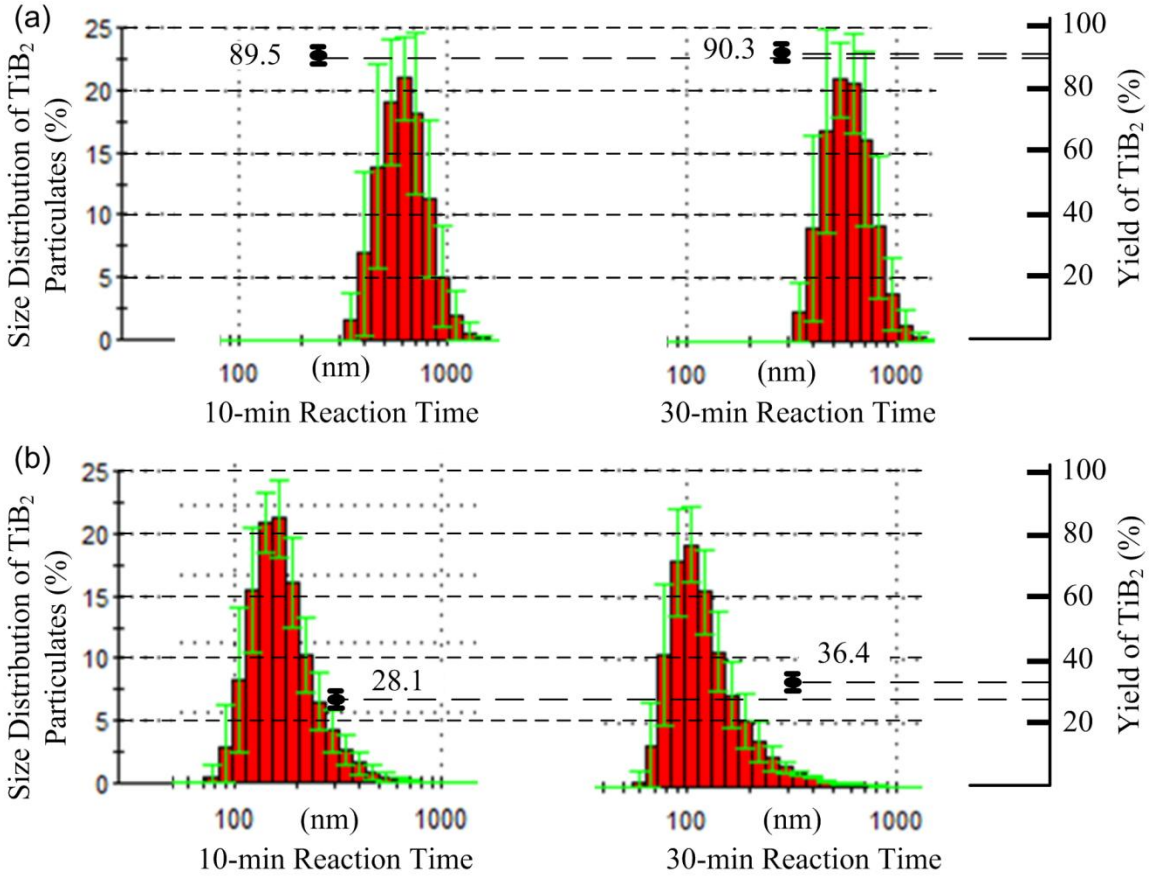

Figure 5.2 Comparison of the mixed-salts reactions at 900 °C (a) and 700 °C (b) regarding the size distribution and yield of TiB_2 particulates.

According to the SEM analysis (Figures 4.18 and 4.23), the products in the S700 samples were more complicated, in which blocky Al_3Ti particulates, tiny TiB_2 particulates and chain-like Al_3Ti reinforcement containing TiB_2 phase were all formed. Actually, when the Al melt temperature is low, the ratio of Ti/B is always higher than ½. Part of Ti reacts with B to form TiB_2 phase, and the rest of Ti will react with Al to form Al_3Ti phase. As reported by Mohanty et al. (1995), the growth of Al_3Ti could engulf the entire TiB_2 particulate. Alternatively, the Al_3Ti might also nucleate as individual particulates (Guzowski, Sigworth, & Sentner, 1987).

At a lower temperature, the transfer speed of B to molten Al is much lower than that of Ti, thereby the ratio of T/B is much higher than ½. Some TiB_2 particulates can form following the precipitation-growth process. Since the content of B is rather low in the reaction interface, the growth of TiB_2 will be limited. As a result, the size of TiB_2 in the S700-10 sample was much smaller than that of TiB_2 produced in the S900-10 sample.

In the S700-30 sample, the newly formed TiB_2 particulates had a smaller size. It is reasonable that the newly formed TiB_2 particulates in the S700-30 sample were obtained according to Eq. 2.7, by which Al_3Ti reacted with AlB_2 to form TiB_2. The detailed formation process has been studied by Emamy et al. (2006) and Michael Rajan et al. (2013), respectively. The basic sequence of TiB_2 formation can be proposed as follows:

1. The B from AlB_2 moves toward Al_3Ti phase;

2. Reaction takes place between Ti and B in a gap from Al_3Ti surface to formTiB_2;

3. Dissolution of Al_3Ti phase due to natural cracking and fragmentation of Al_3Ti which lead to increased rate of TiB_2 formation.

These steps involve the dissolutions of AlB_2 and Al_3Ti phases and the reaction for synthesizing TiB_2. Thereby, the related formation process of TiB_2 is a dissolution-reaction process.

Al_3Ti phase in the S700-10 sample mainly exists in the chain-like reinforcements. The area surrounding Al_3Ti phase is a [Ti]-rich region. AlB_2 phase also exists in molten Al, which can dissolve in Al to generate B atoms. When B atoms contact with the Al_3Ti phase, Ti and B can react to form TiB_2. The concentrations of [Ti] and [B] are rather low due to the low temperature of molten Al; thereby the TiB_2 particulates synthesized in this period are not able to grow large, and more TiB_2 particulates with smaller size were

formed. As a result, the percentage of TiB_2 particulates with smaller size in the S700-30 sample was increased compared with the S700-10 sample, as shown in Figure 5.2b. As the reaction time was increased, the quantities of Al_3Ti and AlB_2 were both decreased, and more TiB_2 could be formed. A comparison about the chain-like reinforcements between the S700-10 sample and the S700-30 sample is given in Figure 5.3. It is clear that the size of long chain-like reinforcements became small due to the dissolution of Al_3Ti phase in the formation of TiB_2 particulates. In this research, because the temperature was rather low, a complete formation of TiB_2 was hard to achieve in a short holding time.

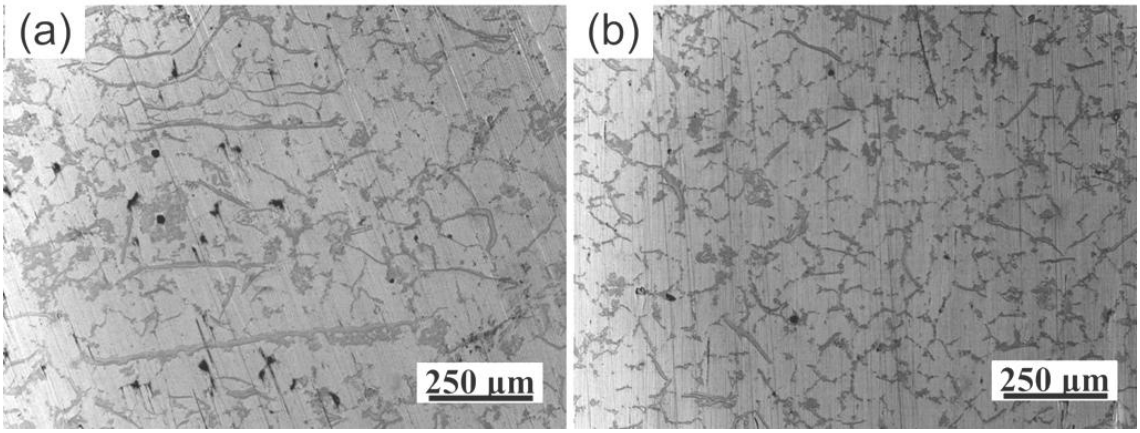

Figure 5.3 Microstructures of the S700-10 sample (a) and S700-30 sample (b).

One more thing should be mentioned is about the AlB_2 phase. In this research, the phases in the slags produced in the fabrications of the S700-10 and S700-30 samples were similar; on the other hand, the content of TiB_2 was increased in the S700-30 sample, it is reasonable to think some AlB_2 should exist in the S700-10 sample. Due to the rather small amount of AlB_2, it is hard to be detected by XRD. As reported by Wang et al.

(2011), blocky AlB_2 could be formed in the Al-B master alloy at 750 °C with a 10-min reaction time. Wang et al. (2012) continued proving that the similar AlB_2 particles still existed in the Al-B master alloy at 750 °C with a 30-min reaction time. So it is hard to distinguish AlB_2 phase in the S700-10 and S700-30 samples in this research.

This research clearly showed that a lower temperature could decrease the size of TiB_2 particulates obviously. However, the synthesis speed of TiB_2 in the mixed-salts reaction at a lower temperature became rather slow, leading to a lower yield of TiB_2. In order to obtain more TiB_2 phase, longer reaction time is needed. Chen et al. (2014) reported that a completed reaction for synthesizing TiB_2 could not be achieved with a 60-min holding time after salt addition at 750 °C, and large areas of AlB_2 and Al_3Ti were observed along the grain boundary of the composites.

Overall, at a higher reaction temperature (900 °C), the mixed-slats reaction for synthesizing TiB_2 phase mainly follows the precipitation-growth process at the reaction interface between salts and liquid Al. At a lower reaction temperature (700 °C), two types of TiB_2 particulates are formed: one is formed following the precipitation-growth process at the reaction interface, and the other one some is produced due to the dissolution reaction between AlB_2 and Al_3Ti. The latter one has a smaller size compared with the former one.

5.1.2 Effects of Ultrasound on the Synthesis of TiB_2 at 700 °C

In this research, a much higher yield of TiB_2 particulates was obtained via the ultrasound assisted mixed-salts reaction at 700 °C with a 10-min reaction compared with the experiment without ultrasound. The yields of TiB_2 phase synthesized in the two

samples are shown in Figure 5.4. The yield of TiB_2 phase in the UTS700-10 sample could reach 90.40 %, whereas value was just 28.10 % in the S700-10 sample.

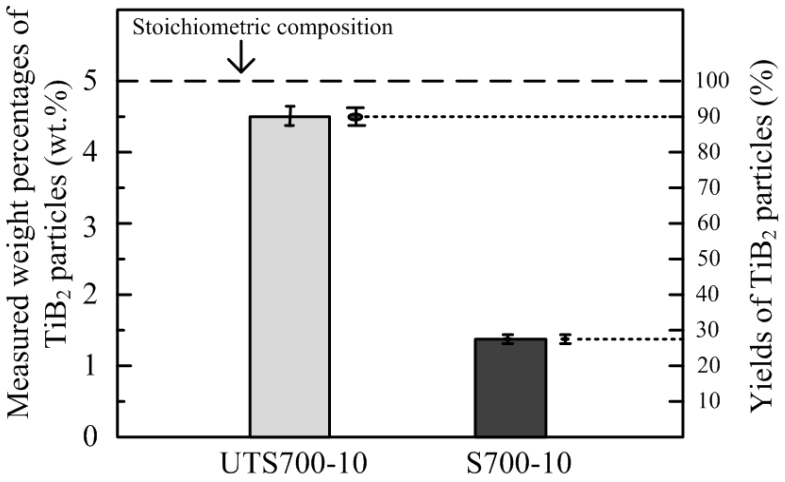

Figure 5.4 Yields of TiB_2 synthesized in the UTS700-10 and S700-10 samples.

After adding the mixed K_2TiF_6 and KBF_4 powders into the pure Al melt irradiated with high-intensity ultrasound, the solid powders were dissolved into the melt immediately. Shortly, the melt surface turned red, indicating that plenty of heat was generated during the mixed-salts reaction; whereas, the dissolution rate of which became slower in the Al melt without ultrasound, suggesting that ultrasound was able to accelerate the dissolution of salts into the melt effectively. The temperature changes of the Al melt in both experiments were measured in one minute intervals for 10 min with a thermocouple which was immersed into the melt with a depth of about 3 cm, as shown in Figure 5.5. The temperature of the melt could increase about 90 °C in one minute, and then the temperature started to decrease. As the reaction proceeded, the amount of reactants became less, and the heat was transferred to deeper melt, leading to the fall of

temperature. In the ultrasound assisted mixed-salts reaction, in the first 6 min, the temperature of melt irradiated with ultrasound was higher than that without using ultrasound, indicating that the mixed-salts reaction was promoted effectively in the ultrasonic fields.

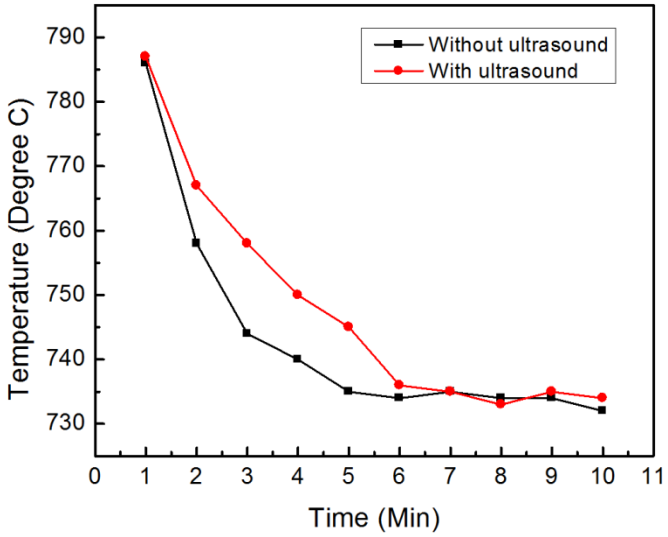

Figure 5.5 Temperature changes of the Al melt during the reaction with time.

In the present research, it is demonstrated that high-intensity ultrasound was able to promote the synthesis of TiB_2 phase effectively via the mixed-salts reaction at a lower temperature. It is well known that ultrasonic fields in a liquid can give rise to nonlinear effects, such as acoustic caviation and acoustic streaming. A developed cavitation generated by ultrasonic vibration in the melt can be evaluated by two ultrasonic parameters: one is the frequency and the other is the acoustic intensity. Generally, the frequency of high-intensity ultrasound might be influenced by the temperature of the melt. A high temperature can result in the decrease of the ultrasonic frequency. In this research,

the frequency change of ultrasound in the Al melt was measured in one minute intervals for 10 min with a frequency meter. The related results were shown in Figure 5.6. Before immersing the Nb probe into the melt, the ultrasonic frequency was 20.01 kHz. After 10 min, the value of frequency was around 19.84 kHz. It is clear that the ultrasonic frequency decreased a little bit, but its attenuation was rather limited. Thereby, the actual working frequency of introduced into the melt in this research was able to arouse ultrasound.

The acoustic intensity p_k in the melt can be expressed by the following expression:

$$p_k = \left(\frac{2P\rho_L C_L}{S}\right)^{\frac{1}{2}} \qquad \text{Eq. 5.3}$$

where P is the output power of ultrasonic generator, ρ_L the density of melt, C_L the speed of ultrasound in the melt, S the cross sectional area of the probe tip. In our research, $P = 1.5kW$, $\rho_L = 1.92gcm^{-3}$ (Chrenkova, Danek, & Silny, 2001), and $S = 5.06cm^2$. The speed of ultrasound in the mixed molten K_2TiF_6-KBF_4 salt has never been reported. According to the work by Cantor (1972), the value of C_L could be approximately regarded as $2.5\times10^3 ms^{-1}$, thereby $p_k = 1.69\times10^6 Pa$, which is much higher than the threshold value for generating acoustic cavitation. Based on this calculation, it is reasonable to believe that the cavitation was able to reach the developed stage in molten salts.

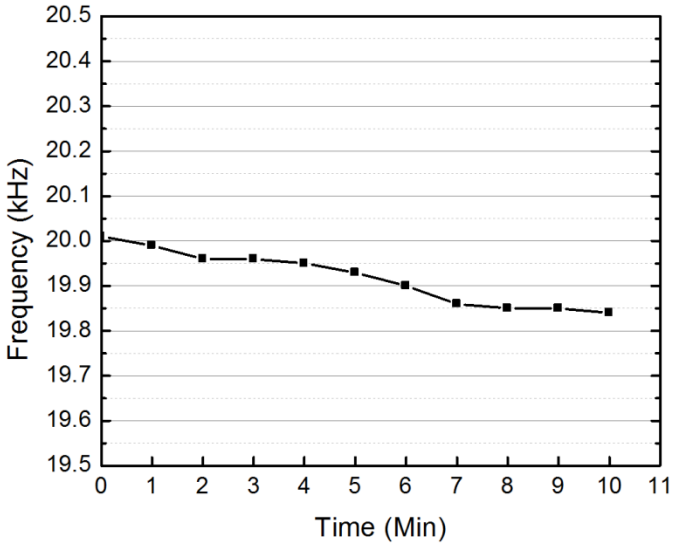

Figure 5.6 The working frequency of ultrasound in the mixed-salts reaction.

The synthesis of TiB_2 particles undergoes the processes of nucleation and growth, in which the saturabilities of Ti and B atoms and their diffusion rates from the molten mixed salts to Al melt both influence the formation of TiB_2 particles. Thereby, the effects of ultrasound on promoting the formation of TiB_2 particles can be investigated in terms of the above aspects. In order to explain the synthesis of TiB_2 in ultrasonic field, a schematic illustration about ultrasound assisted the mixed-salts reaction at lower reaction temperature is shown in Figure 5.7.

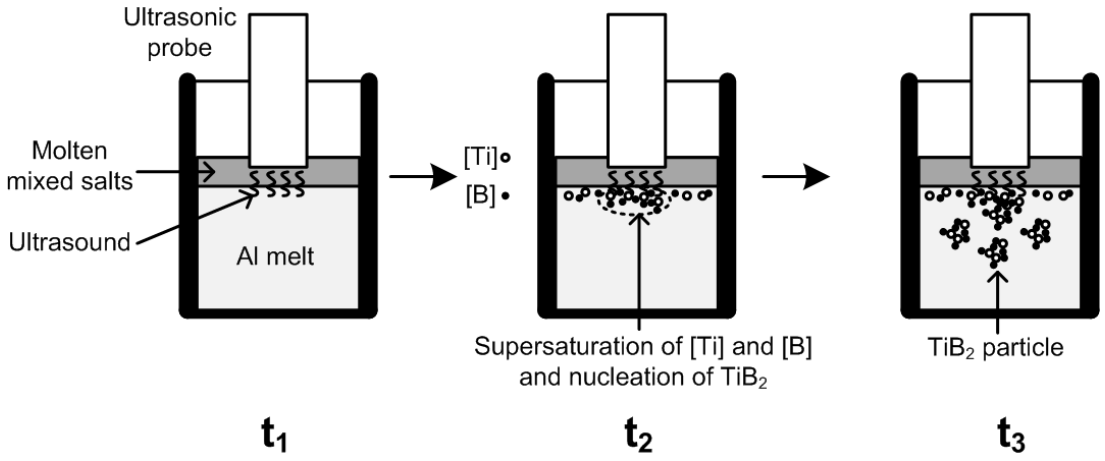

Figure 5.7 Schematic illustration showing the synthesis mechanism of small-sized TiB_2 particulates in ultrasonic field (t: the holding time, and $t_1 < t_2 < t_3$).

As mentioned above, a rapid dissolution of solid mixed salts in Al melt was obtained in this research, which was attributed to the effects of ultrasonic cavitation. For Al-K_2TiF_6-KBF_4 system, ultrasound can generate micro-jet impact and shock wave damage in front of the surfaces of solid salts. These two physical effects result in the localized erosion which can greatly promote the dissolution rate of solid salts. The time when ultrasound is introduced to the Al melt is denoted as t_1. Within the molten salts Ti and B atoms start to diffuse into the Al melt across the interface of salts and Al melt. The Ti and B atoms can react with Al to form Al_3Ti and AlB_2 by reduction reactions firstly. In ultrasonic fields, the bubble collapses produces extreme local temperature which can reach 5000 K; thereby the Al_3Ti and AlB_2 can be more easily dissolved into the Al melt to form [Ti] and [B].

As the time increases, the concentrations of [Ti] and [B] adjacent to the interface increase due to the further diffusions. It should be mentioned that due to the application of ultrasound, more energy is provided to the molten mixed salts. As reported in Chapter

2, the cycle of single acoustic cavitation is rather short, and the ultrasound is able to activate the chemical reaction effectively in a short time. As a result, the activities of Ti and B atoms are enhanced greatly, resulting in much faster and easier transfers from salts to molten Al. Consequently, a saturation of [Ti] and [B] can be reached rapidly by using ultrasound compared to the treatment without ultrasonic.

When the concentrations of [Ti] and [B] research saturation, TiB_2 nuclei precipitate from the saturation region in the Al melt, and the time of this stage is denoted as t_2. Shock waves generated in the ultrasonic fields can induce several physical and chemical effects, including the enhanced mass transfers due to strong turbulent mixing and acoustic streaming. Thereby, the Ti and B in the Al melt irradiated with ultrasound have better contact, leading to the formation of more effective TiB_2 nuclei. It has been reported that the sonication can effectively enhance the nucleation rate. (Gracin, Uusi-Penttilä, & Rasmuson, 2005). In addition, previous research (Luque de Castro & Priego-Capote, 2007) has shown that ultrasound can induce primary nucleation in nominally particle-free solutions at much lower supersaturation levels, and can shorten the induction time between the moment when supersaturation is established and the onset of nucleation and crystallization.

As the time increases from t_2 to t_3, more Ti and B deposit to the surfaces of the growing TiB_2 crystals. Consequently, the size of TiB_2 particulates becomes larger. In this research, the size of TiB_2 particulates was much smaller compared with the S900 samples. The possible reason might be explained as follows. On the one hand, more effective TiB_2 nuclei can be produced in ultrasonic field; thereby the size of single TiB_2 particle can be limited. On the other hand, the growth of TiB_2 crystals is also influenced by the solute

concentration around them. Solute-rich region can provide more Ti and B for the growth of TiB_2 in a certain amount of time. Due to the strong turbulent mixing and acoustic streaming, TiB_2 particulates are pushed far away from the solute-rich region, and the growth of TiB_2 particulates can be hindered effectively. Thereby, the size of most of in situ formed TiB_2 particulates was smaller than 300 nm in this research.

The mechanical disturbances created by both cavitaion and ultrasonic streaming alter the fluid dynamics and increase bulk-phase mass transfer. On the one hand, supersatutration of Ti and B in the Al melt could be obtained easily, and Ti and B had more chance to contact in ultrasonic fields, leading to the formation of more effective TiB_2 nuclei in the Al melt. On the other hand, rapid mass transfer of the solute could provide more Ti and B on the surface of the growing TiB_2 particles.

In addition, extremely high temperature and pressure created by bubble collapse in the ultrasonic fields can give rise to the following effects (Ruecroft, Hipkiss, Ly, Maxted, & Cains, 2005): 1) subsequent rapid local cooling rates, calculated at 10^7-10^{10} K/s, play a significant role in increasing supersaturation; 2) localized pressure increases reduce the crystallization temperature, and 3) the cavitation events allow the excitation energy barriers associated with nucleation to be surmounted. The above effects can accelerate the nucleation and growth rates of TiB_2 particulates obviously.

5.2 Discussion of the Direct-metal Reaction

5.2.1 Formation Mechanism of Blocky Al_3Ti Particulates

In this research, small blocky Al_3Ti particulates were synthesized successfully via the direct-melt reaction between solid Ti powders and liquid Al at low temperature of 730 °C. Based on the morphology of reaction layer on the unreacted Ti particles and the EDS results, it is obvious that the reaction layer was composed of by some Al_3Ti particles, which became looser and larger from inside to outside of the layer. Some separated Al_3Ti particulates were distributed around the reaction layer as well. Accordingly, a reaction-peeling model was proposed to explain the formation of small blocky Al_3Ti particulates at low temperatures.

A reactive diffusion can occur at the Ti/Al interface as soon as the solid Ti particle contacts the liquid Al. In reactive diffusion, the reaction rate for the formation of new phase can be evaluated by diffusion coefficients for the species. It is well known that the impurity diffusion coefficient in solids is usually described by the Arrhenius equation:

$$D = D_0 \exp(-E_A / RT) \qquad \text{Eq. 5.4}$$

where D_0 is a temperature-independent pre-exponential (m^2/s), E_A the activation energy for diffusion (J/mol), R the gas constant, and its value 8.31 J/mol•K; T the absolute temperature (K). Based on this empirical equation, the diffusion rates for Ti atoms to Al and Al atoms to Ti in the Ti (solid)-Al (liquid) system can be approximately evaluated, and then the main diffusion phase can be defined. In the temperature range of 700-850 °C, the Arrhenius equation for the diffusion coefficients for Al in solid Ti ($D_{Al/Ti}$) (Thuillard, Tran, & Nicolet, 1988) and for Ti in liquid Al($D_{Ti/Al}$) (Du, Chang, Huang, Gong, Jin, Xu, Yuan, Liu, He, & Xie, 2003) can be expressed as the following equations, respectively:

$$D_{Al/Ti} = 9.58\times10^{-9}\, m^2/s \bullet \exp\left[\frac{-114600J/mol}{8.31J/molK\cdot T}\right] \quad \text{Eq. 5.5}$$

$$D_{Ti/Al} = 4.29\times10^{-7}\, m^2/s \bullet \exp\left[\frac{-36300J/mol}{8.31J/molK\cdot T}\right] \quad \text{Eq. 5.6}$$

Since some heat was released in the reaction, the temperature of the Al melt containing solid Ti powders was in the range of 730-750 °C, and the values of $D_{Al/Ti}$ and $D_{Ti/Al}$ are in the range of 1.0×10^{-14} to 1.35×10^{-14} m^2/s and 5.5×10^{-9} to 6.0×10^{-9} m^2/s, respectively, as shown in Figure 5.8. This result illustrates that solid Ti is the main diffusing species in the Al(l)-Ti(s) system, for the values of $D_{Ti/Al}$ are much greater than those of $D_{Al/Ti}$ by around five orders of magnitude.

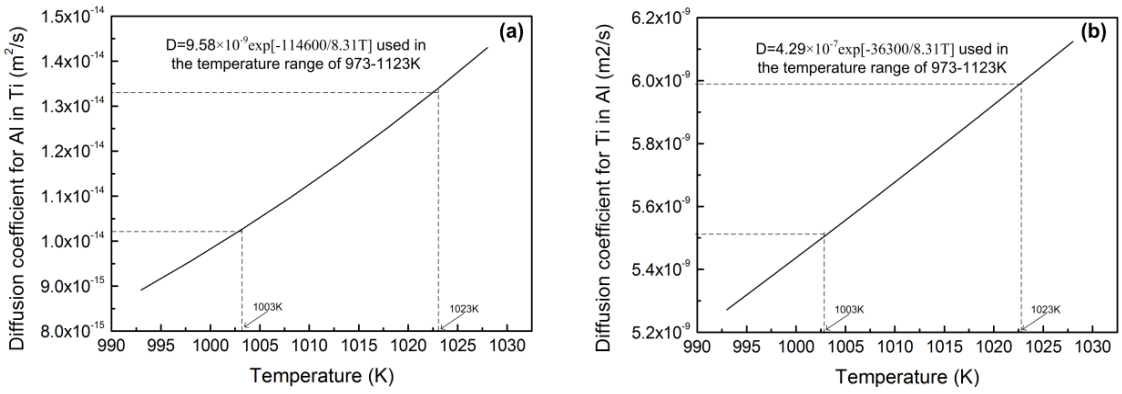

Figure 5.8(a) Diffusion coefficients for Al in Ti and (b) diffusion coefficients for Ti in Al in the temperature range of 973-1123 K.

In order to illuminate the formation mechanism of the small-sized blocky Al_3Ti particulates, a schematic illustration about the evolution of Ti powders in molten Al is shown in Figure. 5.9. A single Ti particle is regarded as a Ti sphere. In the initial stage of diffusion of Al(l)-Ti(s) system, solid Ti powders totally exposure to liquid Al, and plenty of Ti atoms can cross Ti/Al interface into liquid Al in a very short time. According to the

Al-Ti phase diagram (Sigworth, 1984) (as shown in Figure.2.7), It is clear that the solubility of Ti in liquid Al is rather low at 730 °C, which is less than 0.15 wt. %. As a result, the initial diffusion of Ti atoms across the Ti/Al interface into the liquid Al can produce a saturated solution adjacent to the interface. After that, the nucleation of Al_3Ti phase occurs, and these Al_3Ti nuclei attach to the surface of solid Ti particle. The time for the formation of the Al_3Ti nuclei is referred as t_1, as shown in Figure 5.9a.

As the reaction time increases from t_1 to t_2, further diffusion of Ti atoms results in the growth of Al_3Ti particles on the solid Ti surface. Due to the spherical morphology of Ti particle, Al_3Ti particles grow along the radical direction rather than the planar direction. For Al_3Ti phase, it usually has the priority growth at <110> direction. John et al.(1979a) indicated that for the growth of Al_3Ti particles, the growth rate anisotropy can be adequately accounted for by a marked difference in the rate of atomic attachment to the major crystallographic planes. The analysis of atomic attachment kinetics by Jackson (1969) suggested that, for a given crystallographic direction related to the planar density normal to that direction, a nucleation of new atomic layers is easier on the lower density planes. Al_3Ti phase has the lowest density on (110) direction, thereby the growth of Al_3Ti favors <110> direction. As a result, the Al_3Ti reaction layer on the surface of Ti particle is not a compact layer and some inter-Al_3Ti particle spacings exist in the reaction layer due to the above growth characteristics of in situ Al_3Ti particles, as shown in Figure 5.9b.

As the reaction time further prolongs to t_3, more Ti atoms are consumed to form Al_3Ti phase, and Al_3Ti particles grow larger. Thereby, for the reactive diffusion between solid Ti and liquid Al, it is a process of the decrease of solid Ti volume, but also a process of the increase of Al_3Ti volume. Figure 5.10 shows the evolution of thickness of

the reaction layer on the solid Ti particles at 730 °C with different reaction times (1, 3, 5 and 10 min). The thickness of S730-1, S730-3, S730-5 and S730-10 were 5, 10, 15 and 25μm, respectively. These reaction layers were composed of by a few of Al_3Ti particles with inter-spacings.

One important feature is that the volume of the Al_3Ti phase formed in the Al-Ti interface is greater than the consumption volume of Ti, which can be easily understood due to the lower density of Al_3Ti comparing with Ti. Also, Machowiak et al. (1959) reported the same finding in their research. This volume change easily gives rise to stresses in the reaction layer. During the growth of Al_3Ti phase, tensile stresses in the reaction layer develop parallel to the Ti surface. An easy rupture of Al_3Ti particles from reaction layer takes place when the tensile stresses become large enough. The existence of spacings between each Al_3Ti particles and the brittleness of Al_3Ti are attributed to the peeling process. Furthermore, the rupture of the Al_3Ti phase is also attributed the shear stress produced by the liquid Al flow. In addition, some works reported that the fracture strength of a metal can be reduced in a liquid metal, because the liquid metal affects the fracture behavior at the tip of the crack, reducing the critical stress intensity for fracture and altering the micromechanism of fractures at the crack tip, which is named as liquid metal induced embrittlement (Clegg, 2001; Lynch, 1984). Liquid Al may give rise to a similar effect on the fracture of the Al_3Ti phase. Based on the preceding analysis, the Al_3Ti phase can be easily peeled from the reaction layer during the direct-melt reaction, as shown in Figure 5.9c.

After the Al_3Ti particles peel from the reaction layer, the remaining Al_3Ti phase starts to grow following the above steps. The latter peeling particles push the earlier

peeling particles away to outside. Thereby, a loose reaction layer composed of loose Al_3Ti particles can be formed.

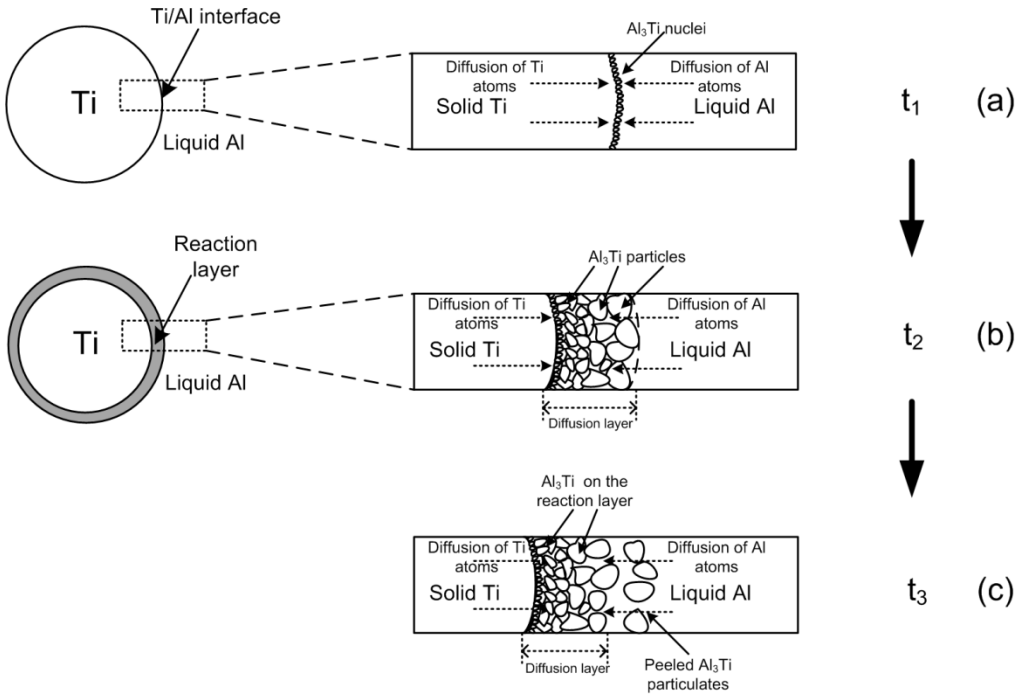

Figure 5.9 Schematic illustration showing the formation mechanism of small-sized blocky Al_3Ti particulates (t: the reaction time, $t_1<t_2<t_3$): (a) nucleation of Al_3Ti, (b) growth of Al_3Ti, and (c) rupture of Al_3Ti particulates.

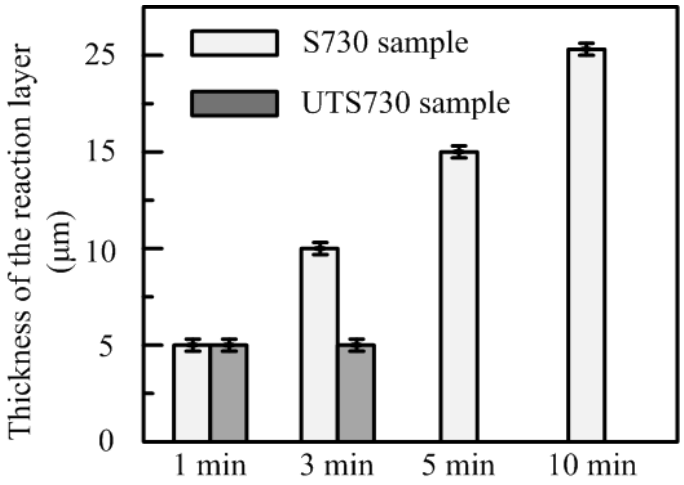

Figure 5.10 Thickness of the reaction layers on Ti particles in the S730 and UTS730 samples with different reaction times.

It is easy to understand that the temperature of molten Al has a significant effect on the direct-melt reaction for synthesizing Al_3Ti phase. A higher temperature can lead to a faster direct-melt reaction, because the diffusion coefficients increase as temperature increases. Most importantly, a higher temperature can shorten the delay time of the direct-melt reaction. Once the reaction occurs, the solid Ti powders are hard to be wrapped by Al_2O_3 films and the direct-melt reaction between solid Ti powders and liquid Al can proceed.

In this research, when solid Ti powders were added into molten Al at 700 °C, the temperature of molten Al around the addition would be decreased, because some heat was absorbed by the solid Ti powders. The reactive diffusion between solid Ti powders and liquid Al was delayed. The solid Ti powders were easily wrapped by Al_2O_3 films to form inclusions, and then the reactive diffusion between solid Ti and liquid Al was limited severely. In the end, the direct-melt reaction was not able to occur at 700 °C.

5.2.2 Effects of Ultrasound on the Direct-melt Reaction

According to the results of direct-melt reaction conducted at 730 and 700 °C, it is obvious that high-intensity ultrasound promoted significantly the synthesis of Al_3Ti particulates via the direct-melt reaction between solid Ti powders and liquid Al. Based on the preceding analysis, the formation mechanism of Al_3Ti particulates at low temperatures was explained through the reaction-peeling model. The effects of ultrasound on the reaction are analyzed in terms of this formation mechanism.

Results in Chapter 4 showed that the reaction time for a completed direct reaction at 730 °C in ultrasonic fields was about 3-5 min; whereas the reaction time exceeded 10 min at 730 °C without ultrasound. It is clear that the reaction time was shortened remarkably by using ultrasound. The advantage of ultrasound in the direct-melt reaction at a lower temperature was highlighted in this research. At 700 °C, the direct-melt reaction between solid Ti powders and liquid Al was hard to be conducted without ultrasound; whereas in situ Al_3Ti particulates could be formed successfully in ultrasonic fields.

When high-intensity ultrasound was introduced in molten Al at 730 °C (or 700 °C), the generation of a developed acoustic cavitation in the Al melt was also evaluated by Eq. 5.3. In this experiment, the density of molten Al, $\rho_{Al} = 2.35 g cm^{-3}$, $C_L = 4.65 \times 10^3 ms^{-1}$; thereby $P_k = 2.55 \times 10^6 Pa$, which is much larger than the threshold value for arising acoustic cavitation in molten Al, indicating that acoustic cavitation played crucial effects on the direct-melt reaction for synthesizing Al_3Ti particulates.

As introduced in Chapter 2, when high-intensity ultrasound is introduced into the liquid-solid (powders) system which can be regarded as a suspension system, some unique effects are generated in the suspension. One is the instantaneously high pressure in the Al melt, the value of which can reach around 500 atmospheres. Once the high pressure is add on the Ti particle, the Al_3Ti particles on its surface will be peeled away more easily. On the other hand, due to the existence of shock waves, the ultrasonic irradiation of liquid-solid (powder) suspensions produces a very important effect: high velocity interparticle collisions. As reported by Suslick (1990), the shock waves can cause small particles to collide into one another with great force and the impact velocities range from 100-500 m/s for particles ~10 μm. The interparticle collisions are able to introduce remarkable changes in surface morphology, composition and reactivity. In this research, a solid particle can collide with the other solid particle with high speed due to effect of ultrasound. Based on the momentum theorem, since the collision time is rather short, the force generated between the two particles will be extremely large. Thereby, the Al_3Ti reaction layer on the Ti surface can be destroyed effectively, leading to a thinner Al_3Ti reaction layer on the Ti surface. In addition, due to the viscosity of the Al melt, the high speed movement of Ti particles wrapped with Al_3Ti particles in the Al melt can produce shear force between the solid particles and liquid Al, which also contributed to the peeling of Al_3Ti particles. The accelerated peeling of Al_3Ti from the reaction layer in ultrasonic field can decrease the thickness of reaction layer, by which the contact of Ti atoms and Al atoms became much easier, and the reaction time was shortened remarkably.

By comparing the S730 samples with the UTS730 samples, it is clear that the thickness of the reaction layer in the UTS730 samples were much thinner than those in

the S730 samples, as shown in Figure 5. 10. The thickness of the reaction layers in UTS730-1 and UTS730-3 samples were just around 5 μm, which was similar to the size of Al_3Ti particulates, suggesting that the reaction layer was composed of by a single layer of Al_3Ti particles. The results clearly show that the outside Al_3Ti particles of the reaction layers were easily peeled away in the ultrasonic fields. In the meantime a thinner reaction layer can result in a faster reaction between solid Ti and liquid Al, as the diffusion distance becomes shorter.

In addition, the diffusion coefficient of solid Ti in liquid Al is a key parameter for the direct-metal reaction. The diffusion coefficient might be increased because of the instantaneously high temperature generated in the ultrasonic fields, leading to a faster diffusion reaction, which is also a positive factor for synthesizing Al_3Ti particulates in molten Al.

Also, as mentioned in Chapter 2, there are two main proposed mechanisms for the effects of acoustic cavitation on the liquid-solid interface: shock wave damage and micro-jet impact. Both of which can induce the damage to the solid surface.

In this research, large sized inclusions containing solid Ti powders were easily formed in molten Al at 700 °C. The asymmetry of the environment near these inclusions induces a deformation of the cavity during the collapse of bubbles. As reported by Suslick (1990), this deformation is self-reinforcing, and it sends a fast-moving stream of liquid through the cavity at the surface with velocities greater than 100 m/s.

The second mechanism of cavitation-induced surface damage invokes shock waves created by cavity collapse in molten Al. High frequency nonlinear shear stress

resulting from shock waves in the ultrasonic fields can lead to the erosion of solid inclusion containing Ti powders.

The impingement of micro-jets and shock waves on the inclusions results in the localized erosion which can tear the inclusions and the solid Ti powders can be released into molten Al. Thereby Al_3Ti particulates can be formed in the ultrasonic fields at 700 °C.

In addition, the acoustic streaming generated in ultrasound fields is also attributed to the disruption of the inclusions in molten Al, because it can induce the microstreming. The shear force resulting from the microstreaming might be an active mechanism of the disruption of inclusions.

5.3 Conclusions

Low-temperature synthesis of particulates in molten Al was concerned in this research, in which the mixed-salts reaction of K_2TiF_6-KBF_4-Al system for synthesizing TiB_2 particulates and the direct-melt reaction between solid Ti powders and liquid Al for producing Al_3Ti particulates were both studied. By applying high-intensity ultrasound to the two reactions, TiB_2 and Al_3Ti particulates can be synthesized at much lower temperatures. The following conclusions are drawn:

1. Reaction temperature has an important influence on the synthesis of TiB_2 in molten Al via the mixed-salts reaction. A high temperature (900 °C) is beneficial for the formation of TiB_2. A higher temperature can lead to a higher yield of TiB_2 particulates with a larger size. In contrast, smaller-sized TiB_2 particulates can be obtained at a lower temperature (700 °C), but the formation of TiB_2 can be limited significantly. In the

meantime, some intermediate products such as Al_3Ti and AlB_2 phases exist in the Al matrix.

2. At a higher reaction temperature (900 °C), the formation of TiB_2 particulates mainly follows a precipitation-growth process, in which the nucleation and growth of TiB_2 phase proceed at the reaction interface between the salts and Al. At a lower temperature (700 °C), the precipitation-growth process and dissolution reaction between AlB_2 and Al_3Ti both contribute to the formation of TiB_2. As the reaction time is prolonged, TiB_2 particulates with a smaller size can be formed.

3. High-intensity ultrasound has remarkable effects on the formation of TiB_2 particulates at a lower temperature. A high yield of TiB_2 particulates with smaller size is obtained via the ultrasound assisted mixed-salts reaction. Ultrasound can lead to accelerated mass transfers of Ti and B from the molten salts to the reaction interface, and a high nucleation rate of TiB_2 can be accelerated significantly in ultrasonic fields. These two effects contribute to the low-temperature synthesis of TiB_2.

4. For the direct-melt reaction between solid Ti powders and liquid Al at low temperatures, a reaction-peeling model is created to explain the formation of small blocky Al_3Ti particulates in molten Al.

5. Ultrasound is able to effectively accelerate the reaction-peeling process. The reaction time for a completed synthesis of Al_3Ti can be shortened significantly. Most importantly, the formation of inclusions containing solid Ti powders can be avoided in the ultrasonic fields, allowing for the realization of a lower-temperature synthesis of Al_3Ti at 700 °C.

5.4 Future Work

Due to the limitation of the research time, more important work is worth doing in the future based on this research.

For the mixed-salts reaction, only 10-min and 30-min reaction times were studied in the present research. Actually, in order to clarify the reaction clearly, more reaction times are needed, such as 5 min, 20 min and 60 min; especially for the ultrasound assisted mixed-salts reaction, some shorter reaction times, such as 1min, 3 min and 5 min might be useful to recognize the effects of ultrasound on the mixed-salts reaction.

For the ultrasound assisted direct-melt reaction, the temperature of molten Al was decreased as low as 700 °C. Since the melting point of pure Al is about 660 °C, the temperatures lower than 700 °C can be tried in the future work. The Al alloys always have much lower melting temperatures than pure Al. It is reasonable to think that the ultrasound assisted direct-melt reaction has more advantages in the fabrication of in situ Al_3Ti/Al alloys composites. Also, some alloying elements in the Al alloys might influence the direct-melt reaction for producing Al_3Ti phase. Thereby, more interesting results might be obtained using the Al alloys to replace the pure Al in the direct-melt reaction.

The final aim of fabricating in situ particulate reinforced Al (alloys) composites is to improve the mechanical properties of materials. The mechanical properties of Al composites should be examined in the future work.

REFERENCES

REFERENCES

Alippi, A., Galbato, A., & Cataldo, F. (1992). Ultrasound cavitation in sonochemistry: Decomposition of carbon tetrachloride in aqueous solutions of potassium iodide. *Ultrasonics, 30*(3), 148-151.

Anandkumar, R., Almeida, A., & Vilar, R. (2011). Wear behavior of Al–12Si/TiB_2 coatings produced by laser cladding. *Surface and Coatings Technology, 205*(13), 3824-3832.

Arnberg, L., Bäckerud, L., & Klang, H. (1982a). 1: Production and properties of master alloys of Al–Ti–B type and their ability to grain refine aluminium. *Metals Technology, 9*(1), 1-6.

Arnberg, L., Bäckerud, L., & Klang, H. (1982b). Evidence of metastable phase in Al–Ti–(B) system. *Metals Technology, 9*(1), 14-17.

Basu, B., Raju, G., & Suri, A. (2006). Processing and properties of monolithic TiB2 based materials. *International materials reviews, 51*(6), 352-374.

Birol, Y. (2009). Al–Ti–B grain refiners via powder metallurgy processing of Al/K_2TiF_6/KBF_4 powder blends. *Journal of alloys and compounds, 480*(2), 311-314.

Blake, J. R., & Gibson, D. (1987). Cavitation bubbles near boundaries. *Annual Review of Fluid Mechanics, 19*(1), 99-123.

Brennen, C. E. (2013). *Cavitation and bubble dynamics*: Cambridge University Press.

Cantor, S. (1972). Relationship between Sonic Velocity and Entropy in Molten Salts. *Journal of Applied Physics, 43*(2), 706-709.

Chen, Z., Chen, Y., An, G., Shu, Q., Li, D., & Liu, Y. (2000). Microstructure and properties of in situ Al/TiB2 composite fabricated by in-melt reaction method. *Metallurgical and Materials Transactions A, 31*(8), 1959-1964.

Chen, Z., Wang, T., Zheng, Y., Zhao, Y., Kang, H., & Gao, L. (2014). Development of TiB_2 reinforced aluminum foundry alloy based in situ composites – Part I: An improved halide salt route to fabricate Al–5wt% TiB_2 master composite. *Materials Science and Engineering: A, 605*(0), 301-309.

Chrenkova, M., Danek, V., & Silny, A. (2001). Density of the Molten System KCl-KBF $_4$-K_2TiF_6. *Chemical Papers-Slovak Academy of Sciences, 55*(1), 27-31.

Christy, T., Murugan, N., & Kumar, S. (2010). A comparative study on the microstructures and mechanical properties of Al 6061 alloy and the MMC Al 6061/TiB2/12p. *Journal of Minerals and Materials Characterization and Engineering, 9*, 57.

Clegg, R. (2001). A fluid flow based model to predict liquid metal induced embrittlement crack propagation rates. *Engineering Fracture Mechanics, 68*(16), 1777-1790.

Davies, P., Kellie, J., & Wood, J. (1992). UK patent 2257985A. *ASM, Paris, September*.

Doel, T., & Bowen, P. (1996). Tensile properties of particulate-reinforced metal matrix composites. *Composites Part A: Applied Science and Manufacturing, 27*(8), 655-665.

Doktycz, S. J., & Suslick, K. S. (1990). Interparticle collisions driven by ultrasound. *Science, 247*(4946), 1067-1069.

Dong, S., & Yang, T. (2008). Thermodynamic analysis of the formation of In-situ reinforced phases in cast Al-4.5 Cu alloy. *Journal of Wuhan University of Technology-Mater. Sci. Ed., 23*(3), 342-345.

Dragut, D. V., Moldovan, P., & Butu, M. (2012). Thermodynamics and Mechanism of Metalothermic Reduction of Molten Salts. *Revista de Chimie, 63*(9), 925-928.

Du, Y., Chang, Y., Huang, B., Gong, W., Jin, Z., Xu, H., . . . Xie, F.-Y. (2003). Diffusion coefficients of some solutes in fcc and liquid Al: critical evaluation and correlation. *Materials Science and Engineering: A, 363*(1), 140-151.

El-Mahallawy, N., Taha, M. A., Jarfors, A. E., & Fredriksson, H. (1999). On the reaction between aluminium, K_2TiF_6 and KBF_4. *Journal of alloys and compounds, 292*(1), 221-229.

Emamy, M., Mahta, M., & Rasizadeh, J. (2006). Formation of TiB_2 particles during dissolution of $TiAl_3$ in Al–TiB_2 metal matrix composite using an in situ technique. *Composites Science and Technology, 66*(7), 1063-1066.

Eskin, G. I. (1997). Ultrasonic treatment of light alloy melts.

Fan, T., Yang, G., & Zhang, D. (2005). Thermodynamic effect of alloying addition on in-situ reinforced TiB2/Al composites. *Metallurgical and Materials Transactions A, 36*(1), 225-233.

Feng, C., & Froyen, L. (2000). Microstructures of in situ Al/TiB_2 MMCs prepared by a casting route. *Journal of materials Science, 35*(4), 837-850.

Fjellstedt, J., & Jarfors, A. E. (2005). On the precipitation of TiB2 in aluminum melts from the reaction with KBF_4 and K_2TiF_6. *Materials Science and Engineering: A, 413*, 527-532.

Gracin, S., Uusi-Penttilä, M., & Rasmuson, Å. C. (2005). Influence of ultrasound on the nucleation of polymorphs of p-aminobenzoic acid. *Crystal growth & design, 5*(5), 1787-1794.

Guzowski, M., Sigworth, G., & Sentner, D. (1987). The role of boron in the grain. *Metallurgical Transactions A, 18*(5), 603-619.

Han, Y., Liu, X., & Bian, X. (2002). In situ TiB_2 particulate reinforced near eutectic Al–Si alloy composites. *Composites Part A: Applied Science and Manufacturing, 33*(3), 439-444.

Hayes, F., & Lukas, H. (1991). The Al-B-Ti system (Aluminum-Boron-Titanium). *Journal of phase equilibria, 12*(5), 609-611.

Hyun, S., Lee, D.-R., & Loh, B.-G. (2005). Investigation of convective heat transfer augmentation using acoustic streaming generated by ultrasonic vibrations. *International Journal of Heat and Mass Transfer, 48*(3–4), 703-718.

Jie, W., Kandalova, E., Zhang, R., & Nikitin, V. (2000). Al_3Ti/Al composites prepared by SHS. *Rare Metal Materails and Engineering*.

Jones, G. P., & Pearson, J. (1976). Factors affecting the grain-refinement of aluminum using titanium and boron additives. *Metallurgical Transactions B, 7*(2), 223-234.

Kori, S., Biradar, S., & Auradi, V. (2014). Synthesis of Al-Al_3Ti In Situ Metal Matrix Composites by Salt Route and Evaluation of their Mechanical Properties. *Advanced Materials Research, 984, 280-284.*

Kornfeld, M., & Suvorov, L. (1944). On the destructive action of cavitation. *Journal of Applied Physics, 15*(6), 495-506.

Kumar, S., Subramanya Sarma, V., & Murty, B. (2008). A statistical analysis on erosion wear behaviour of A356 alloy reinforced with in situ formed TiB_2 particles. *Materials Science and Engineering: A, 476*(1), 333-340.

Kwak, J. S., Mohney, S., Lin, J.-Y., & Kern, R. (2000). Low resistance Al/Ti/n-GaN ohmic contacts with improved surface morphology and thermal stability. *Semiconductor science and technology, 15*(7), 756.

Lakshmi, S., Lu, L., & Gupta, M. (1998a). In situ preparation of TiB_2 reinforced Al based composites. *Journal of Materials Processing Technology, 73*(1), 160-166.

Lakshmi, S., Lu, L., & Gupta, M. (1998b). In situ preparation of TiB_2 reinforced Al based composites. *Journal of Materials Processing Technology, 73*(1), 160-166.

Lauterborn, W., & Bolle, H. (1975). Experimental investigations of cavitation-bubble collapse in the neighbourhood of a solid boundary. *Journal of Fluid Mechanics, 72*(02), 391-399.

Leighton, T. (1994). *The acoustic bubble*: Academic press.

Li, G. R., Wang, H. M., Zhao, Y. T., Chen, D. B., Chen, G., & Cheng, X. N. (2010). Microstructure of in situ Al_3Ti/6351Al composites fabricated with electromagnetic stirring and fluxes. *Transactions of Nonferrous Metals Society of China, 20*(4), 577-583.

Li, J.X., & Wu, A.P. (2005). *Principle of Materials Processing* , Peking University Press, Beijing.

Li, Z., Li, M., Xiao, Y., & Wang, C. (2014). Ultrarapid formation of homogeneous Cu6Sn5 and Cu3Sn intermetallic compound joints at room temperature using ultrasonic waves. *Ultrasonics sonochemistry, 21*(3), 924-929.

Liu, Z., Han, Q., & Li, J. (2013). Fabrication of in situ Al_3Ti/Al composites by using ultrasound assisted direct reaction between solid Ti powders and liquid Al. *Powder Technology, 247*, 55-59.

Liu, Z., Han, Q., Li, J., & Huang, W. (2012). Effect of ultrasonic vibration on microstructural evolution of the reinforcements and degassing of in situ TiB_{2p}/Al–12Si–4Cu composites. *Journal of Materials Processing Technology, 212*(2), 365-371.

Liu, Z., Rakita, M., Han, Q., & Li, J. (2011). Microstructural evolution of reinforcements in the remelting in situ TiC/Al–12Si composites treated by ultrasonic vibration. *Materials Research Bulletin, 46*(10), 1674-1678.

Liu, Z. W., Han, Q., & Li, J. G. (2012). Formation of Small Blocky Al3Ti Particles via Direct Reaction Between Solid Ti Powders and Liquid Al. *Metallurgical and Materials Transactions a-Physical Metallurgy and Materials Science, 43A*(12), 4460-4463.

Liu, Z. W., Han, Q. Y., & Li, J. G. (2011). Ultrasound assisted in situ technique for the synthesis of particulate reinforced aluminum matrix composites. *Composites Part B-Engineering, 42*(7), 2080-2084.

Liu, Z. W., Rakita, M., Wang, X. M., Xu, W., & Han, Q. Y. (2014). In situ formed Al_3Ti particles in Al alloy matrix and their effects on the microstructure and mechanical properties of 7075 alloy. *Journal of materials research, 29*(12), 1354-1361.

Liu, Z. W., Wang, X. M., Han, Q. Y., & Li, J. G. (2014). Effects of the addition of Ti powders on the microstructure and mechanical properties of A356 alloy. *Powder Technology, 253*, 751-756.

Lohse, D. (2003). Bubble puzzles. *Physics Today, 56*(2), 36-42.

Lupis, C., & Elliott, J. (1966). Generalized interaction coefficients: Part I: Definitions. *Acta Metallurgica, 14*(4), 529-538

Lupis, C., & Elliott, J. (1967). Prediction of enthalpy and entropy interaction coefficients by the "central atoms" theory. *Acta Metallurgica, 15*(2), 265-276.

Lupis, C. H. (1983). Chemical thermodynamics of materials. *Elsevier Science Publishing Co., Inc., 1983*, 581.

Luque de Castro, M., & Priego-Capote, F. (2007). Ultrasound-assisted crystallization (sonocrystallization). *Ultrasonics sonochemistry, 14*(6), 717-724.

Lynch, S. (1984). A fractographic study of gaseous hydrogen embrittlement and liquid-metal embrittlement in a tempered-martensitic steel. *Acta Metallurgica, 32*(1), 79-90.

Ma, Z., Zhao, W., Yan, J., & Li, D. (2011). Interfacial reaction of intermetallic compounds of ultrasonic-assisted brazed joints between dissimilar alloys of Ti6Al4V and Al4Cu1Mg. *Ultrasonics sonochemistry, 18*(5), 1062-1067.

Mackowiak, J., & Shreir, L. (1959). The nature and growth of interaction layers formed during the reaction between solid titanium and liquid aluminium. *Journal of the Less Common Metals, 1*(6), 456-466.

Mandal, A., Maiti, R., Chakraborty, M., & Murty, B. (2004). Effect of TiB_2 particles on aging response of Al–4Cu alloy. *Materials Science and Engineering: A, 386*(1), 296-300.

Mason, T. J., & Lorimer, J. P. (2002). Applied sonochemistry. *The uses of power ultrasound in chemistry and processing*, 1-48.

Mayes, C., McCartney, D., & Tatlock, G. (1993). Influence of microstructure on grain refining performance of Al–Ti–B master alloys. *Materials science and technology, 9*(2), 97-103.

McNamara, W. B., Didenko, Y. T., & Suslick, K. S. (1999). Sonoluminescence temperatures during multi-bubble cavitation. *Nature, 401*(6755), 772-775.

Merouani, S., Hamdaoui, O., Rezgui, Y., & Guemini, M. (2014). Theoretical estimation of the temperature and pressure within collapsing acoustical bubbles. *Ultrasonics sonochemistry, 21*(1), 53-59.

Michael Rajan, H. B., Ramabalan, S., Dinaharan, I., & Vijay, S. J. (2013). Synthesis and characterization of in situ formed titanium diboride particulate reinforced AA7075 aluminum alloy cast composites. *Materials & Design, 44*(0), 438-445.

Mohanty, P., & Gruzleski, J. (1995). Mechanism of grain refinement in aluminium. *Acta Metallurgica et Materialia, 43*(5), 2001-2012.

Moldovan, P., Butu, M., Popescu, G., Buzatu, M., Usurelu, E., Soare, V., & Mitrica, D. (2010). Thermodynamics of Interactions in Al-K_2TiF_6-KBF_4 System. *Revista de Chimie, 61*(9), 828-832.

Neppiras, E. (1984). Acoustic cavitation series: part one: Acoustic cavitation: an introduction. *Ultrasonics, 22*(1), 25-28.

Neppiras, E., & Noltingk, B. (1951). Cavitation produced by ultrasonics: theoretical conditions for the onset of cavitation. *Proceedings of the Physical Society. Section B, 64*(12), 1032.

Neppiras, E. A. (1980). Acoustic cavitation. *Physics Reports, 61*(3), 159-251.

Noltingk, B. E., & Neppiras, E. A. (1950). Cavitation produced by ultrasonics. *Proceedings of the Physical Society. Section B, 63*(9), 674.

Nyborg, W. L. (1958). Acoustic streaming near a boundary. *The Journal of the Acoustical Society of America, 30*(4), 329-339.

Plesset, M. (1949). The dynamics of cavitation bubbles. *J. Appl. Mech., 16*, 277.

Plesset, M. S., & Chapman, R. B. (1971). Collapse of an initially spherical vapour cavity in the neighbourhood of a solid boundary. *Journal of Fluid Mechanics, 47*(02), 283-290.

Plesset, M. S., & Prosperetti, A. (1977). Bubble dynamics and cavitation. *Annual Review of Fluid Mechanics, 9*(1), 145-185.

Poritsky, H. (1951). The collapse or growth of a spherical bubble or cavity in a viscous fluid. *Journal of Applied Mechanics-Transcations of the Asme, 18,* 332-333.

Prasad, K., Sonawane, S., Zhou, M., & Ashokkumar, M. (2013). Ultrasound assisted synthesis and characterization of poly (methyl methacrylate)/$CaCO_3$/ nanocomposites. *Chemical Engineering Journal, 219*, 254-261.

Rayleigh, L. (1917). VIII. On the pressure developed in a liquid during the collapse of a spherical cavity. *The London, Edinburgh, and Dublin Philosophical Magazine and Journal of Science, 34*(200), 94-98.

Richards, W. T., & Loomis, A. L. (1927). The chemical effects of high frequency sound waves I. A preliminary survey. *Journal of the American Chemical Society, 49*(12), 3086-3100.

Ruecroft, G., Hipkiss, D., Ly, T., Maxted, N., & Cains, P. W. (2005). Sonocrystallization: the use of ultrasound for improved industrial crystallization. *Organic Process Research & Development, 9*(6), 923-932.

Sakharov, D. V., Hekkenberg, R. T., & Rijken, D. C. (2000). Acceleration of Fibrinolysis by High-frequency Ultrasound: The Contribution of Acoustic Streaming and Temperature Rise. *Thrombosis Research, 100*(4), 333-340.

Sigworth, G. K. (1984). The grain refining of aluminum and phase relationships in the Al-Ti-B system. *Metallurgical Transactions A, 15*(2), 277-282.

Spoor, P., Maynard, J., Pan, M., Green, D., Hellmann, J., & Tanaka, T. (1997). Elastic constants and crystal anisotropy of titanium diboride. *Applied physics letters, 70*(15), 1959-1961.

St John, D., & Hogan, L. (1979). Metallography and growth crystallography of Al_3Ti in Al-Ti alloys up to 5 wt% Ti. *Journal of Crystal Growth, 46*(3), 387-398.

Starritt, H., Duck, F., & Humphrey, V. (1991). Forces acting in the direction of propagation in pulsed ultrasound fields. *Physics in medicine and biology, 36*(11), 1465.

Suslick, K. S. (1988). Ultrasound: its chemical, physical, and biological effects: *VCH Publishers.*

Suslick, K. S. (1989). The chemical effects of ultrasound. *Scientific American, 260*(2), 80-86.

Suslick, K. S. (1990). Sonochemistry. *Science, 247*(4949), 1439-1445.

Suslick, K. S., Eddingsaas, N. C., Flannigan, D. J., Hopkins, S. D., & Xu, H. (2011). Extreme conditions during multibubble cavitation: Sonoluminescence as a spectroscopic probe. *Ultrasonics sonochemistry, 18*(4), 842-846.

Suslick, K. S., Hammerton, D. A., & Cline, R. E. (1986). The Sonochemical Hot-Spot. *Journal of the American Chemical Society, 108*(18), 5641-5642.

Suslick, K. S., & Price, G. J. (1999). Applications of ultrasound to materials chemistry. *Annual Review of Materials Science, 29*(1), 295-326.

Tee, K., Lu, L., & Lai, M. (2001). In situ stir cast Al–TiB_2 composite: processing and mechanical properties. *Materials science and technology, 17*(2), 201-206.

Tee, K. L., Lu, L., & Lai, M. (1999). In situ processing of Al–TiB_2 composite by the stir-casting technique. *Journal of Materials Processing Technology, 89*, 513-519.

Thuillard, M., Tran, L., & Nicolet, M.-A. (1988). Al_3Ti formation by diffusion of aluminum through titanium. *Thin Solid Films, 166*, 21-28.

Tijun, C., Jian, L., & Yuan, H. (2009). Casting fabrication of in situ Al_3Ti-Al composites and their wear behaviors. *Research & Development*.

Tjong, S. C., & Ma, Z. (2000). Microstructural and mechanical characteristics of in situ metal matrix composites. *Materials Science and Engineering: R: Reports, 29*(3), 49-113.

Tomita, Y., & Shima, A. (1986). Mechanisms of impulsive pressure generation and damage pit formation by bubble collapse. *Journal of Fluid Mechanics, 169*, 535-564.

Wang, T., Chen, Z., Fu, H., Xu, J., Fu, Y., & Li, T. (2011). Grain refining potency of Al–B master alloy on pure aluminum. *Scripta Materialia, 64*(12), 1121-1124.

Wang, T., Fu, H., Chen, Z., Xu, J., Zhu, J., Cao, F., & Li, T. (2012). A novel fading-resistant Al–3Ti–3B grain refiner for Al–Si alloys. *Journal of alloys and compounds, 511*(1), 45-49.

Wang, X., Jha, A., & Brydson, R. (2004). In situ fabrication of Al3Ti particle reinforced aluminium alloy metal–matrix composites. *Materials Science and Engineering: A, 364*(1-2), 339-345.

Williams, A. (1974). DNA degradation by acoustic microstreaming. *The Journal of the Acoustical Society of America, 55*(S1), S17-S17.

Williams, A., & Slade, J. (1971). Ultrasonic dispersal of aggregates of Sarcina lutea. *Ultrasonics, 9*(2), 76-80.

Wilson, G. M. (1964). Vapor-liquid equilibrium. XI. A new expression for the excess free energy of mixing. *Journal of the American Chemical Society, 86*(2), 127-130.

Wright, R., Rabin, B., & McFerran, W. (1992). Combustion synthesis of cubic Al_3Ti alloys. *Journal of materials research, 7*(10), 2733-2738.

Wu, J. M., Zheng, S. L., & Li, Z. Z. (2000). Thermal stability and its effects on the mechanical properties of rapidly solidified Al-Ti alloys. *Materials Science and Engineering: A, 289*(1–2), 246-254.

Xu, H., Zeiger, B. W., & Suslick, K. S. (2013). Sonochemical synthesis of nanomaterials. *Chemical Society Reviews, 42*(7), 2555-2567.

Xue, J., Wang, J., Han, Y. F., Chen, C., & Sun, B. D. (2012). Behavior of CeO_2 additive in in-situ TiB_2 particles reinforced 2014 Al alloy composite. *Transactions of Nonferrous Metals Society of China, 22*(5), 1012-1017.

Yu, H., Chen, H., Sun, L., & Min, G. (2006). Preparation of Al-Al_3Ti in situ composites by direct reaction method. *Rare Metals, 25*(1), 32-36.

Yue, N. L., Lu, L., & Lai, M. O. (1999). Application of thermodynamic calculation in the in-situ process of Al/TiB_2. *Composite structures, 47*(1–4), 691-694.

Zeiger, B. W., & Suslick, K. S. (2011). Sonofragmentation of molecular crystals. *Journal of the American Chemical Society, 133*(37), 14530-14533.

Zhang, M. X., Kelly, P., Easton, M., & Taylor, J. (2005). Crystallographic study of grain refinement in aluminum alloys using the edge-to-edge matching model. *Acta Materialia, 53*(5), 1427-1438.

Zhang, Q., Xiao, B., Wang, W., & Ma, Z. (2012). Reactive mechanism and mechanical properties of in situ composites fabricated from an Al–TiO_2 system by friction stir processing. *Acta Materialia, 60*(20), 7090-7103.

VITA

VITA

Zhiwei Liu
Graduate School, Purdue University

Education
B.S., 2005, Wuhan University of Science and Technology, Wuhan, China
M.S., 2008, Xi'an Jiaotong University, Xi'an, China
Ph.D., 2012, Shanghai Jiao Tong University, Shanghai, China
Ph.D., 2014, Purdue University, West Lafayette, Indiana

Research Interests
Fabrication of metal matrix composites.
Fabrication of advanced materials.

PUBLICATIONS

PUBLICATIONS

JOURNALS:

Liu, Z.W., Rakita, M., Xu, W., Wang, X.M., & Han, Q.Y. (2015). Ultrasound assisted Salts-metal reaction for synthesizing TiB_2 particles at low temperature, *Chemical Engineering Journal* 263, 317-324.

Liu, Z.W., Rakita, M., Xu, W., Wang, X.M., & Han, Q.Y. (2014). Ultrasound assisted combustion synthesis of TiC in Al-Ti-C system, *Ultrasonics Sonochemistry* (In revision).

Liu, Z.W., Rakita, M., Wang, X.M., Xu, W., & Han, Q.Y. (2014). In situ formed Al_3Ti particles in Al alloy matrix and their effects on the microstructure and mechanical properties of 7075 alloy. *Journal of materials research, 29*(12), 1354-1361.

Liu, Z.W., Wang, X.M., Han, Q.Y., & Li, J. G. (2014). Effects of the addition of Ti powders on the microstructure and mechanical properties of A356 alloy. *Powder Technology, 253*, 751-756.

Liu, Z.W., Wang, X.M., Han, Q.Y, & Li, J.G. (2014). Synthesis of submicrometer-sized TiC particles in aluminum melt at low melting temperature. *Journal of materials research*, 29(7), 896-901.

Liu, Z.W., Wang, X.M., Han, Q.Y, & Li, J.G. (2014). Effect of ultrasonic vibration on direct reaction between solid Ti powders and liquid Al. *Metallurgical and Materials Transactions A*, 45(2), 543-546.

Liu, Z.W., Han, Q.Y, & Li, J.G. (2013). Fabrication of in situ Al_3Ti/Al composites by using ultrasound assisted direct reaction between solid Ti powders and liquid Al. *Powder Technology, 247*, 55-59.

CONFERENCES:

Liu, Z.W., Han, Q.Y. (2015). The evoltion of solid Ti powders in liquid Al and the effects of ultrasound on it. *TMS*. (Accepted)